UNVERSIDAD DE VALENCIA-CSIC

DEPARTAMENTO DE FÍSICA ATÓMICA,
MOLECULAR Y NUCLEAR

INSTITUTO DE FÍSICA CORPUSCULAR

Neutron capture measurement of ^{54}Fe and ^{57}Fe at CERN n_TOF

Giuseppe Giubrone

PhD Thesis
May 2014

Supervised by:
César Domingo Pardo
José Luis Taín Enríquez

César Domingo Pardo y **José Luis Taín Enríquez** Colaboradores Científicos del Consejo superior de Investigaciones Científicas (CSIC),

Certifican: Que la presente memoria "**Neutron capture measurement of ^{54}Fe and ^{57}Fe at CERN n_TOF** " ha sido realizada bajo su dirección en el Instituto de Física Corpuscular (Centro mixto Unversidad de Valencia-CSIC) por **Giuseppe Giubrone** y constituye su Tesis Doctoral dentro del programa de doctorado del Departamento de Física Atómica, Molecular y Nuclear.

Y para que así conste, en cumplimiento con la legislación vigente, presenta ante el Departamento de Física Atómica, Molecular y Nuclear la referida memoria, firmando el presente certificado en Burjassot (Valencia) a 27 de Mayo de 2014.

F.do César Domingo Pardo

F.do José Luis Taín Enríquez

Abstract

The measurement of the (n,γ) cross section of ^{54}Fe and ^{57}Fe isotopes was performed at the CERN n_TOF facility with the aim of better understanding the *s*-process stellar nucleosynthesis in the Fe-Ni region. At the same time Fe is a structural material in accelerator driven systems (ADS) and accurate neutron cross sections are required for reliable design studies, to account for the neutron balance and for assessing the related uncertainties. The accurate measurement of the (n,γ) cross section of ^{54}Fe and ^{57}Fe isotopes in the resolved resonance region (RRR) has been carried out with high resolution using the time of flight technique. These measurements were performed using the total energy detector technique. An optimized detection setup has been used, which permitted the determination of their cross sections with a minimal influence of neutron sensitivity. First part of this work was devoted to the MC simulation of the response function to calculate the corresponding weighting functions. These weighting functions were applied to the measured data in order to obtain the capture yield, and derive the capture cross section. An R-matrix analysis of the resolved resonance region has been performed for both nuclides, deriving the total radiative capture cross section and the corresponding resonance parameters. The analysis was carried out using the R-matrix code SAMMY. The results obtained in this work are compared with previous experiments performed elsewhere and with evaluated data. The results presented in this work are important to disentangle the *r* and *s* contribution observed in the old stars and for advanced reactor concepts.

Contents

List of Figures

List of Tables

Chapter 1

Introduction

1.1 Nucleosynthesis in the universe

Nucleosynthesis describes the processes involved in combining atomic nuclei in order to create other atomic nuclei.

Stars provide the perfect setting for the various reactions necessary for the nucleosynthesis to occur. The two key ingredients required for nucleosynthesis are energy and time. The evolution of stars through the different stages of nuclear burning provide both these ingredients, and so stars are converting the Universe from its original pristine state of hydrogen and helium atoms into a metal-rich area. The basis of the modern astrophysics were made by Fred Hoyle at the end of the 1940's.

In 1957 the paper published by Burbidge et al., settled the nucleosynthesis argument by outlining how the evolution of stars has been the main source for the creation of most of the elements present in the periodic table [1, 2]. In astrophysics the elements on the periodic table are generally divided in two groups based on atomic number, Z. The "light" elements with $Z \leq 30$ and the "heavy" elements with $30 \leq Z \leq 83$. Iron represents a change in regime as to how the elements can be created.

The light elements heavier than boron and lighter than iron are typically formed in charged-particle reactions during nuclear burning in stars. The charge of these particles is sufficiently low to overcome the Coulomb barrier and the nuclei can capture charge particles such as protons and alpha particles. Beyond iron, the Coulomb barrier is too high for charged particle reaction to occur [3, 4].

The neutrons are the key to heavy element formation because the temperatures inside the stars are not high enough for the heavy elements to be formed via proton capture reaction. This is possible because there is no Coulomb repulsion to overcome in interaction between neutrons and heavy elements.

The neutron is also unstable, with a half-life of about 15 minutes. For the process to be efficient we need not only a source of neutrons, but also that the source is immersed in matter sufficiently dense so that the neutrons can interact before decaying. These conditions are naturally found inside stars. The stars appear as places where, at the side of thermonuclear reactions, efficient neutron capture processes take place, while not contributing to the energetics of the star, can make a substantial contribution to the nucleosynthesis of heavy elements. Since neutrons are produced on thermonuclear time scale, their flux remains low ($\sim 10^8 \mathrm{n/cm}^3$) and we can assume that the process is "slow", in the sense that the time between two successive neutron captures in each case is greater than the decay times of unstable elements β-products. That is, the unstable nuclei have time to decay before capturing another neutron. This is the so called s-process and occurs at temperature of 1-10 $\times 10^8$ K. For this reason the s-process can be treated quantitatively and at the same time most of the isotopes on the s-process path are stable and can well be studied in the laboratory [5, 6].

If we consider the stellar neutron flux as $\Phi = n_n v_T$, where $v_T = \sqrt{2kT/m}$ is the thermal velocity and n_n is the neutron density, a neutron capture occurs in a slow time scale and the neutron capture rate became $\lambda_n = \Phi\sigma$, where σ is the neutron capture cross section.

Than in the production of s-process nuclei, we expect the establishment of an approximate equilibrium situation, in which the production rate and destruction rate are equal. Under neutron irradiation the change in abundance N(A) of a particular isotope A can be written as:

$$\frac{dN(A)}{d\tau} = \sigma(A-1)N(A-1) - \sigma(A)N(A). \tag{1.1}$$

In the last equation the term τ is the time integrated neutron flux. To describe the observed abundance an exponential distribution of neutron exposures is assumed [7], in the classical s-process:

$$\rho(\tau) = \frac{GN_{\odot}^{56}}{\tau_0} e^{-\tau/\tau_0} \tag{1.2}$$

The last equation is characterized by two parameters, the factor G of the ^{56}Fe abundances and the mean neutron exposure τ_0.

The bulk of s-process material in the mass range $90 < \mathrm{A} < 204$ is produced by what is called the “main” s-process component. Below A$<$ 90 this component fails to describe the steep increase of the σN curve towards the iron seed. Therefore, a “weak” component is added which is characterized by a smaller mean neutron exposure [7]. Finally, a strong component is to be postulated in order to account for the abundance maximum at lead [8, 9]. The isotopic s-process abundances in the stars can be determined by the corresponding neutron capture cross section. Taking into account the neutron exposure given by eq. 1.2, the product of the stellar cross section and s-process abundances (σN$_s$) can be expressed as function of mass number [7]:

$$\sigma(A)N(A) = \frac{GN_{\odot}^{56}}{\tau_0} \prod_{i=56}^{A} \left(1 + \frac{1}{\sigma_i \tau_0}\right)^{-1}. \tag{1.3}$$

The last equation shows only a dependence on the neutron capture cross section along the neutron capture chain.

Alternatively to the s-process there is the r-process that occurs under extremely large neutron flux. More generally, many isotopes may arise from a combination of both the s- and r-processes.

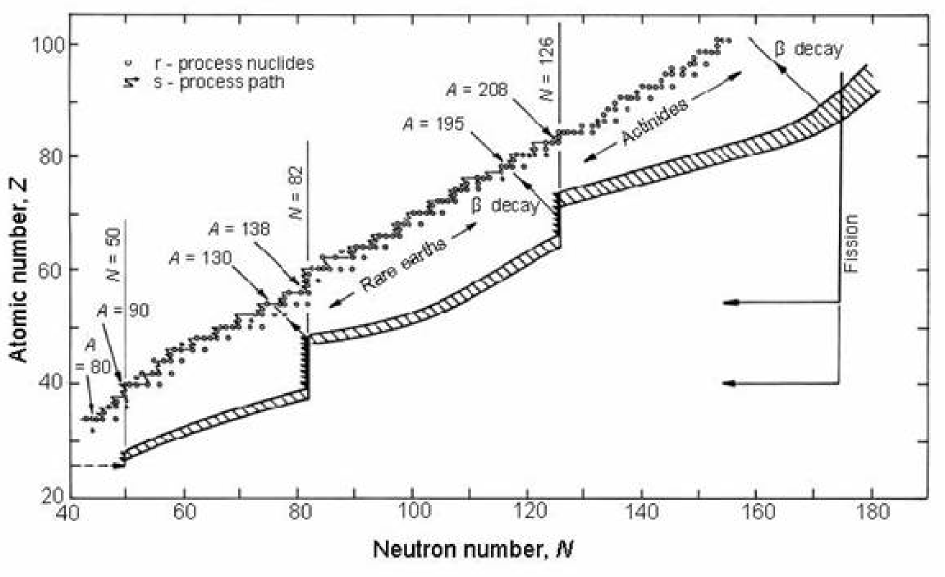

Figure 1.1: *r and s process paths* [3].

The observed r-abundances can be calculated as the difference between the total observed solar abundance $N_{\odot}$ and the s-process contribution.

$$N_r = N_{\odot} - N_s. \tag{1.4}$$

The isotopic s abundances are well established by the fact that they are determined by their respective (n,γ) cross sections, which can be determined in laboratory experiments. The resulting differences between solar and s-process abundances are plotted in Fig. 1.2 together with the ensemble of r-only isotopes.

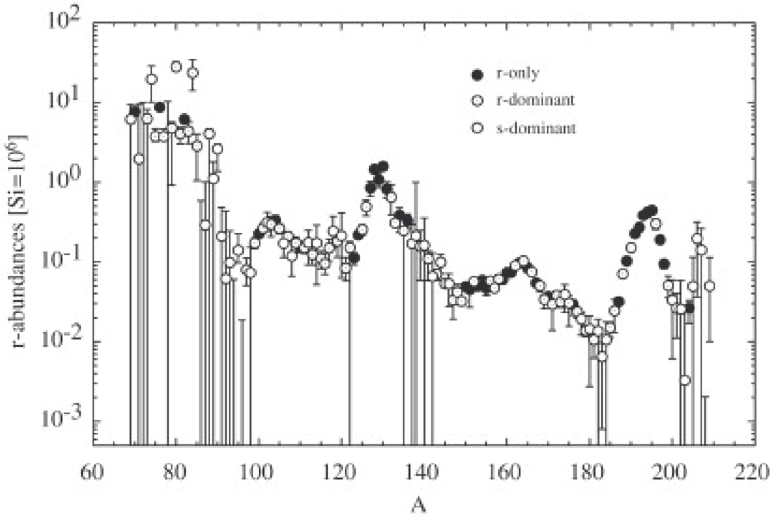

Figure 1.2: *r-process residuals obtained as the subtraction of the s-process contribution from the observed solar abundances* [7].

The obtained r-process residuals show remarkably good agreement with the r-only measured abundances.

In the refinement of stellar models, the neutron data input is needed in the form of cross-sections averaged over the kinetic energy distribution of the stellar neutrons. Average neutron capture cross-sections can be calculated from the energy dependent ones. In stellar environments, the relative velocities v between the neutrons and the target isotopes follow a Maxwell-Boltzmann distribution at a temperature T. The reaction rate in certain assumption can be written as $n \langle \sigma_\gamma \rangle k_T v_T$ and are therefore proportional to the Maxwellian-averaged neutron capture cross-section, (MACS) [10] given by:

$$\langle \sigma \rangle_{kT} = \frac{\langle \sigma_\gamma v \rangle}{\langle v \rangle} = \frac{2}{\sqrt{\pi (kT)^2}} \int_0^\infty \sigma_\gamma(E) E e^{-\frac{E}{kT}} dE \tag{1.5}$$

Here σ_γ is the neutron capture cross-section at the total kinetic energy in the center of mass system. Neutron cross-section are known for many isotopes but the quality of existing data is not always sufficient, in particular for isotopes with small cross-sections or for radioactive isotopes. Innovative neutron facilities characterized by high instantaneous neutron flux and low backgrounds are the place where accurate measurements of neutron capture cross-sections can be performed.

1.2 The radiative neutron capture reaction

The aim of this section is to describe in general the radiative neutron capture process [3, 11, 12].

The radiative neutron capture process consists essentially on the absorption of a neutron by a nucleus, with the formation of a compound nucleus, and subsequently emission of one or more gamma rays. This process can be represented as:

$$Z^A + n \longrightarrow (Z^{A+1})^* \longrightarrow (Z^{A+1}) + \gamma. \tag{1.6}$$

Where $(\mathrm{Z}^{A+1})^*$ is the compound nucleus generated during the process.

The formation of the compound nucleus and the emission of the gamma rays is represented in Fig. 1.3.

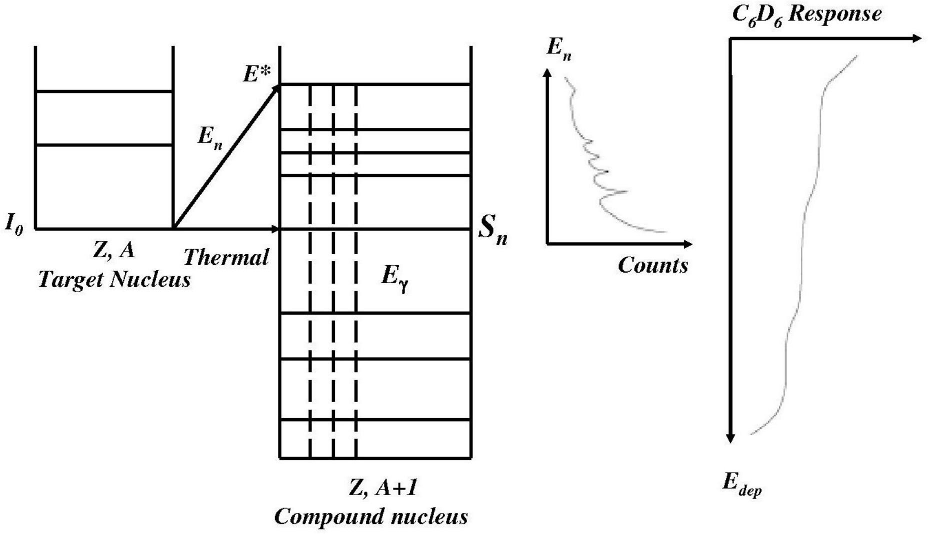

Figure 1.3: *Scheme of the radiative capture process and the observables measured in the experiment, the gamma ray and the neutron energy spectrum.*

After the neutron capture, the nucleus is excited to a level with a energy given by:

$$E^* = S_n^c + \frac{A}{A+1} E_n, \tag{1.7}$$

in this case E_n is the energy of the incident neutron and S_n^c is the neutron separation energy of the nucleus (Z^{A+1}).

The generated compound nucleus decays after an extremely short time ($\sim 10^{-14}$ seconds) by emission of one or several gamma rays E_γ.

Neglecting the recoil energy of the nucleus the sum of the energies of the gammas is equal to the excitation energy:

$$E^* = \sum_i E_i^\gamma. \tag{1.8}$$

The cross section is used to express the interaction between particles, with consequent generation of a compound nucleus, and in the case of a single isolated resonance is given by Breit-Wigner dispersion formula:

$$\sigma_{c^*}(E_n) = g \frac{\pi}{k_n^2} \frac{\Gamma_n \Gamma}{(E_n - E_0)^2 + (\Gamma/2)^2}. \tag{1.9}$$

In the last equation the factor Γ_n is the neutron scattering width, otherwise Γ is the total width which is the sum of the individual reaction widths:

$$\Gamma = \Gamma_\gamma + \Gamma_n + \Gamma_f + \ldots\ldots\ldots \tag{1.10}$$

In the equation 1.9 the factor g is expressed as:

$$g = (2J+1)/((2s+1)(2I+1)), \tag{1.11}$$

where s is the spin of the neutron, I is the spin of the target and J is the spin of the compound nucleus.

The radiative capture width is of the order of 0.5 to 0.1 eV in the medium mass nuclei and smaller for heavy nucleus, generally from 0.1 to 0.03 eV.

Cross-sections for neutron induced reactions below about 1 MeV are characterized by resonances. These resonances correspond to excited levels of the compound nucleus, which are quasi-bound states with a relatively long lifetime. The lifetime τ_γ is about 10^{-14} seconds, and is correlated to the total width of the resonance by the Heisenberg's uncertainty principle:

$$\Gamma_\gamma \tau_\gamma \approx \hbar. \tag{1.12}$$

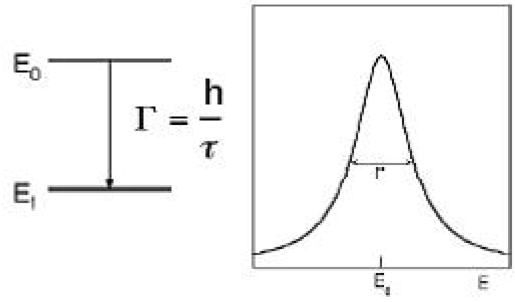

Figure 1.4: *Equivalence in the time energy domain.*

The total width of the level Γ is the sum of partial widths Γ_r corresponding to the decay of the compound nucleus. The probability of the compound nucleus to decay is given by:

$$P_r = \frac{\Gamma_r}{\Gamma}, \tag{1.13}$$

with r = n, γ.

Then, the corresponding cross-section is expressed as:

$$\sigma_r = \sigma_{c*}(E_n)(P_r). \tag{1.14}$$

In the case of a (n,γ) capture the cross-section become:

$$\sigma_\gamma(E_n) = g\frac{\pi}{k_n^2}\frac{\Gamma_n\Gamma_\gamma}{(E_n - E_0)^2 + (\Gamma/2)^2}. \tag{1.15}$$

The total radiative area of a resonance is obtained by integration of the equation 1.14 between $E_0 - \Gamma/2$ and $E_0 + \Gamma/2$:

$$A_r = \frac{2\pi^2}{k_0^2}K_r, \tag{1.16}$$

where K_r is the radiative Kernel expressed as:

$$K_r = g\frac{\Gamma_n\Gamma_\gamma}{\Gamma}. \tag{1.17}$$

1.3 Waste transmutation and ADS Systems

The field of nuclear technology, in particular for energy production in nuclear power plants is another field where neutron cross-section data have a fundamental impact. In this case radioactive waste can be considered as the main disadvantage of the energy production in nuclear power plants.

The large amount of ^{238}U in the fuel is the basis of the production of the highly radio-toxic actinides by successive neutron captures and beta decays, leading to the formation of transuranic elements, like Pu and Cm.

By of partitioning and transmutation (P&T) of the actinides and some of the long-lived fission products, the radio-toxicity of the high-level waste (HLW) can be reduced compared with the current once-through fuel cycle. This requires very effective reactor and fuel cycle strategies, including fast reactors (FRs) and accelerator-driven, sub-critical systems (ADS) [13, 14, 15].

The ADS has recently been receiving increased attention due to its potential to improve the flexibility and safety characteristics of transmutation systems. Although the neutron cross sections at high neutron energy (keV to MeV) are much smaller than at low neutron (thermal) energy, the fission-to-capture ratio is higher in the high energy regime, and this can be exploited in ADSs in order to fission the transuranium isotopes, which were built by neutron capture reactions in the conventional reactor fuel.

The primary benefit of transmutation is a reduction in the minor actinide and long-lived fission product content of the HLW. The first and most effective step to reduce the total mass of the HLW is the transition from a Light Water Reactor (LWR) once-through strategy with direct disposal of the fuel elements to a plutonium burning strategy with HLW vitrification. For the transmutation of actinides, the key reaction is the fission reaction which transforms long-lived, highly radio-toxic actinides into mostly short-lived, less toxic fission products. The transmutation of an actinide is completed, when the transformation chain, which involves “generations” of neutron reactions and radioactive decays, terminates with a fission.

For the long-lived fission products, the goal is to transform them into shorter-lived or stable species by means of neutron capture reactions. The traditional fission product transmutation method is the irradiation of targets in a strong flux of neutrons produced by a fission reactor or a spallation neutron source. This is basically the principle to develop an ADS. The concept of ADS, frequently called hybrid systems, combines a particle accelerator with a sub-critical core as illustrated in Fig. 1.5. The accelerator is either a linac or a cyclotron. The protons are injected onto a spallation target (made with heavy metal) to produce neutrons for driving the subcritical core. After spallation reactions in the target a few tens of neutrons per incident proton are emitted and they are introduced into the sub-critical core to induce further nuclear reactions. The function of the spallation target in the ADS is to convert the incident high energy charged particle beam to low energy neutrons. Iron is omnipresent as constituent of structural components in ADS. All stable isotopes of iron are considered in the reference ADS geometry in the composition of the fuel (cladding material) as well as in the reflector. Therefore the precise knowledge of the radiative neutron capture cross sections of the iron isotopes turns out to be relevant for the design of an ADS for the transmutation of radioactive residues and energy production.

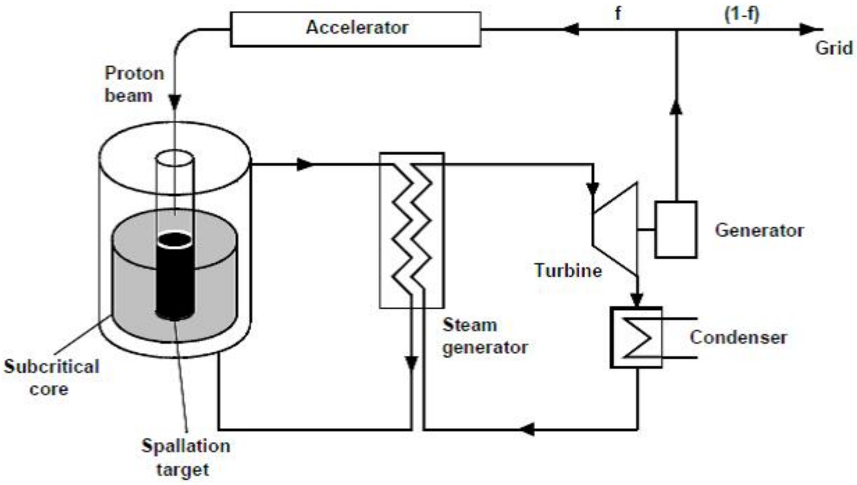

Figure 1.5: *Scheme of an ADS system* [14].

Chapter 2

Experimental setup and measuring technique

The (n,γ) cross section of ^{54}Fe and ^{57}Fe isotopes, in the resolved resonance region has been measured with high resolution using the time of flight technique at the CERN n_TOF facility. These measurements were performed using high time-resolution scintillation C_6D_6 detectors, which register at most one gamma ray per capture event, in a similar way as applied by Macklin and Gibbons [16] for the first time in 1967. Using radiation detectors one can generate an average response function proportional to energy by applying to each pulse from the detector a certain weight, which is function of the pulse height only. This is the basis of the Pulse Height Weighting Technique (PHWT) [17, 18]. These experiments are carried out at the n_TOF facility using a pair of C_6D_6 liquid scintillator detectors which have a low neutron sensitivity. The PHWT has been chosen for these measurements. This is an advantage for the measurement of samples with a high neutron scattering to capture cross section ratio since it allows to reduce the background due to scattered neutrons. However, in this case the simplicity of the experimental set-up is counterbalanced by the more involved analysis procedure, which requires a manipulation of the previously determined detector response function. A description of the n_TOF facility , experimental setup used in the capture experiment, the PHWT technique and the procedure to obtain the polynomial WF will be made in this chapter.

2.1 The CERN neutron time of flight facility n_TOF

CERN n_TOF [19, 20] is a time of flight installation which is based on the spallation mechanism. Neutrons are produced by spallation reactions induced by a sharply pulsed 20 GeV/c proton beam impinging onto a high purity lead target of 80×80×60 cm^3. With this mechanism about 600 neutrons are generated in average for each incident proton. Protons are provided by the CERN Proton Synchrotron (PS). The CERN PS is able to produce high intensities of up to 7×10^{12}ppp (protons per pulse), in the form of short pulses with a repetition time of 1.2 s or multiples of this quantity. In this case the PS proton beam works in dedicated mode. It can also operate in parasitic mode delivering 4×10^{12}ppp. The neutrons produced by spallation are canalized into an experimental area located at 185 m downstream through a vacuum pipe. The lead spallation target is immersed in water contained in an aluminum tank. An additional layer of borated water serves as moderator of the initially fast neutrons with a 1/E flux dependence up to about 1 MeV. The only interface between the moderator and the vacuum pipe is an aluminum alloy window of 1.6 mm thickness. Furthermore, a 2 m long dipole magnet is located 120 m downstream in order to remove from the neutron beam secondary charged particles. A 3 m thick iron shielding is placed after the magnet to minimize the background due to negative muons capture in the experimental area. A two collimators system located at 135.35 m and 175.35 m from the lead target results in a Gaussian beam profile at the sample position. The measuring station starts 182.5 m downstream and the capture sample is positioned usually at 185 m from the window of the spallation target (see Fig. 2.1). Thanks to this very long flight path a very high neutron energy resolution is obtained. $\Delta E/E = 1 \times 10^{-4}$ can be achieved at neutron energies of ~100 keV. A detailed description of the experimental setup in these experiments will be given in the next section.

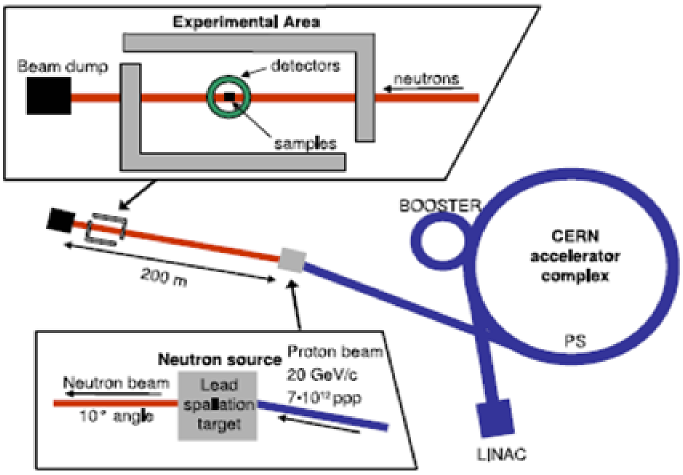

Figure 2.1: *Schematic view of the n_ TOF facility* [20].

2.2 Experimental setup

A picture of the experimental setup used for the measurements is shown in Fig. 2.2.

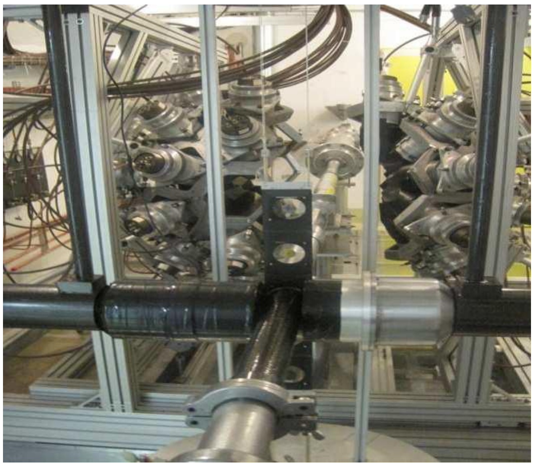

Figure 2.2: *Experimental setup for the capture cross section measurement.*

The two detectors were placed at 90° with respect to the beam line.

The geometric and the isotopic composition of the samples measured at n_TOF for the capture cross section are reported in table 2.1.

Sample	Diameter	Thickness	Mass	Enrichment
^{198}Au	20.03 mm	1 mm	6.1248 g	100%
^{198}Au	19 mm	0.1 mm	0.59599 g	100%
^{54}Fe	20.11 mm	0.86 mm	2.271 g	99.77%
^{57}Fe	19.95 mm	0.64 mm	1.6235 g	96.06%

Table 2.1: *Geometric and isotopic composition of the samples.*

In the next sections each component of the experimental setup is described in detail.

2.2.1 C_6D_6 detectors

Neutron capture events were registered via the prompt gamma ray cascade by a set of two C_6D_6 liquid scintillator detectors with a low neutron sensitivity. In the measurements described in this thesis, two kinds of detectors were used:

- BICRON version: This is a commercial detector, consisting of an aluminum cell based on the design of Nuclear Enterprise and manufactured by BICRON. The photomultiplier tube has been built with a non borated glass window to lower its neutron sensitivity. The C_6D_6 has a volume of 618 cm^3 and is coupled with the photomultiplier by a quartz window, and is provided with a thin aluminum housing and removable teflon tubing coiled around the cell for the expansion of the scintillator [21]. A set of four BICRON detectors are available at n_TOF.

Figure 2.3: *The modified BICRON C_6D_6 detectors.*

- FZK version: This is a detector designed and manufactured at Forschungszentrum Karlsruhe [21] and consists of a very thin carbon fiber cell for the scintillator (1 litre) which was glued directly onto the photomultiplier tube. In this way, all the parts which are not absolutely essential were removed, including the window of the cell and the complete photomultiplier housing, because they are the main source of captured neutrons in the range up to ∼20 keV. Compared to the improved BICRON detector, the resulting neutron sensitivity could be reduced by another factor of four [21].

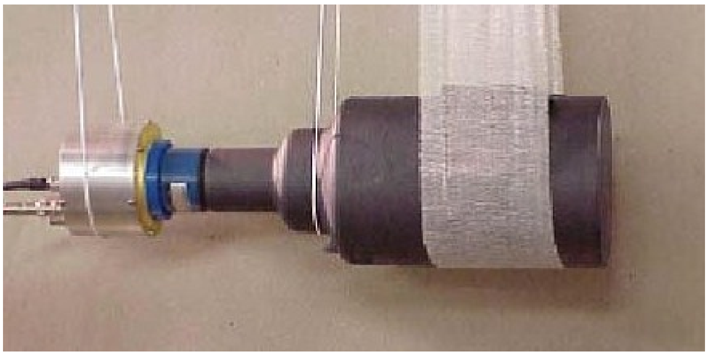

Figure 2.4: *The optimized FZK detector.*

2.2.2 Silicon Monitor(SiMon) and PTB chamber

The accurate determination of neutron cross-section requires a precise knowledge of the neutron flux and of its energy dependence. Different detectors and techniques for measuring and monitoring the neutron flux are present in the experimental area based on a standard reaction with smooth cross section. Generally in the range from the thermal region up to 250 keV and 1 MeV the reaction ^{10}B (n,α) ^{7}Li and ^{6}Li (n, α) ^{3}H, are considered standard, as well as the reaction ^{235}U(n,f) is standard at thermal neutron energy and from 0.15 to 20 MeV. In the first case the detector used is a silicon monitor (SiMon) [22], for the latter case a PTB chamber [23].

- SiMon detector: Four Silicon detectors, covering a large solid angle around a pure ^{6}Li sample of 200 mg/cm^2 thickness and 6 cm diameter on a substrate of 3 μm mylar are placed inside a carbon-fiber vacuum chamber. In this way thanks to the well known ^{6}Li (n, α) cross section it is possible to monitor the neutron flux from thermal to $\sim$ 1 MeV energies. SiMon detectors were used to continuously monitor the neutron beam during capture measurements.

Figure 2.5: *Silicon Monitor.*

- PTB chamber: This fission chamber is provided by the Physikalisch-Technische Bundesanstalt Institute (PTB). Two identical parallel plate ionization chambers (Fig. 2.6) with fissile deposits, one with ^{235}U and another with ^{238}U, have been used with the main objective of determining the neutron flux over a wide energy range. The detectors consist of five platinum plates with fissile deposits on both sides separated by 5 mm, of the electrodes made of tantalum where the thickness of the electrodes is 0.125 mm. The circular plates are 86 mm in diameter, and the fissile deposits have a diameter of 76 mm. The overall thickness of the fission chamber is 50 mm and they work under atmospheric pressure, with a gas mixture made of 90 % of Ar and 10 % of CF_4. The 0.15 mm-thin windows are made of tantalum.

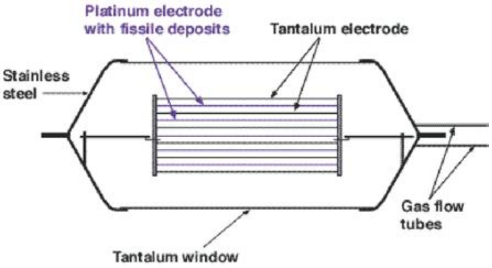

Figure 2.6: *Schematic view of the PTB chamber* [19].

2.2.3 Micro Megas Detector

In order to measure the spatial profile and the homogeneity of the neutron beam arriving at the experimental area, a large surface detector, based on the practically mass-less "MicroMegas" chambers was developed [24]. MicroMegas is a gaseous detector based on simple geometry with planar electrodes. Generally it consists of a conversion gap where radiation produces ionization electrons, and of a thin amplification gap. A thin 5 mm grid separates the two regions. The free electrons drift into the amplification gap where printed electrodes of any shape collect the electrons from the avalanche. In order to operate the Micro Megas detector as a neutron beam profile detector for the n_TOF facility at CERN, an appropriate neutron/charged particle converter has been employed which can be either the filling gas of the detector or a deposited target on its entrance window. Since the neutron energy range of the n_TOF facility extends from a thermal to over 200 MeV, there is not a unique choice of an efficient converter. Interdependent parameters such as the high neutron reaction cross section, the low charged particles energy loss inside the converter, their subsequent energy-angular distribution and the range inside the filling gas should be considered and optimized. In order to achieve a very good profile measurement of the n_TOF beam, it was decided to place the MicroMegas detector inside a vacuum chamber made of Aluminum. The chamber was connected to the standard n_TOF tube that extends up to a diameter of 200 mm.

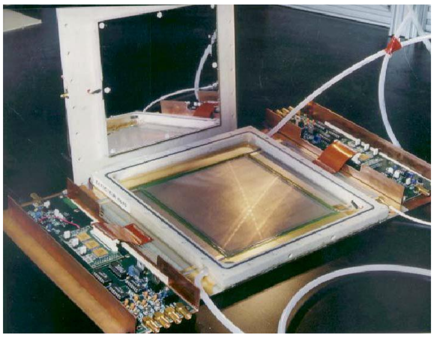

Figure 2.7: *The Micro Megas Detector.*

2.3 Energy and resolution calibration

An energy calibration is needed to relate the amplitude of the registered signal with the energy deposited in the detectors. The detectors were calibrated using three different radioactive sources, ^{137}Cs, ^{88}Y and Am/Be with γ-ray energies of 662 keV, 0.898 keV, 1.62 MeV and 4.4 MeV, respectively.

The deposited energy depends linearly with the pulse height:

$$E_{dep} = a_0 + a_1 \times Amplitude \tag{2.1}$$

For the instrumental resolution we found a different dependence of the energy, depending of the type of detector. For the commercial BICRON there is a simple dependence on the energy,

$$\sigma^2 = b_0 E. \tag{2.2}$$

For the FZK detector the dependence is given by:

$$\sigma^2 = b_0 E + b_1 E^2. \tag{2.3}$$

To obtain the calibration coefficients a set of MC simulations for the experimental setup and for the three different source were made. Subsequently the simulated spectra were recalibrated and convoluted to fit the experimental one. The best calibration coefficients were found using a simultaneous least square fit [25]. The parameters b_0 and b_1 for each detectors and for both experiments are reported in table 2.2. The parameter b_0 is expressed in keV and the parameter b_1 is adimensional.

Detector	b_0(keV)	b_1
BICRON(^{54}Fe)	1.74132	0
BICRON(^{57}Fe)	1.91886	0
FZK(^{54}Fe)	6.01496	9.7422×10^{-3}
FZK(^{57}Fe)	5.48279	1.88702×10^{-3}

Table 2.2: *Parameters obtained for the resolution calibration.*

The resolution obtained for the liquid scintillator detectors is independent from the gain and is shown in Fig. 2.8.

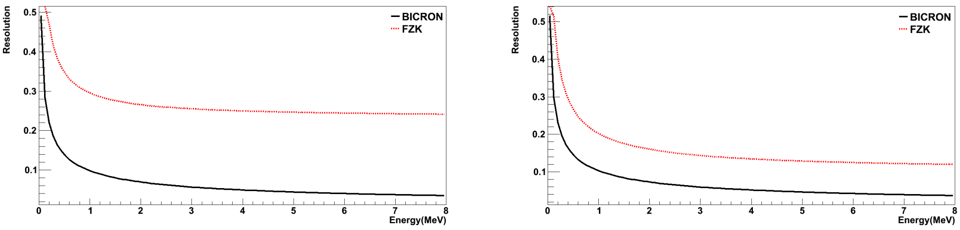

Figure 2.8: *Resolution (FWHM/E) for the FZK (dashed line) and BICRON (solid line) detector for the ^{54}Fe measurement (right) and for ^{57}Fe measurement (left).*

An example of the experimental and simulated (and fitted) spectra is shown in Fig. 2.9.

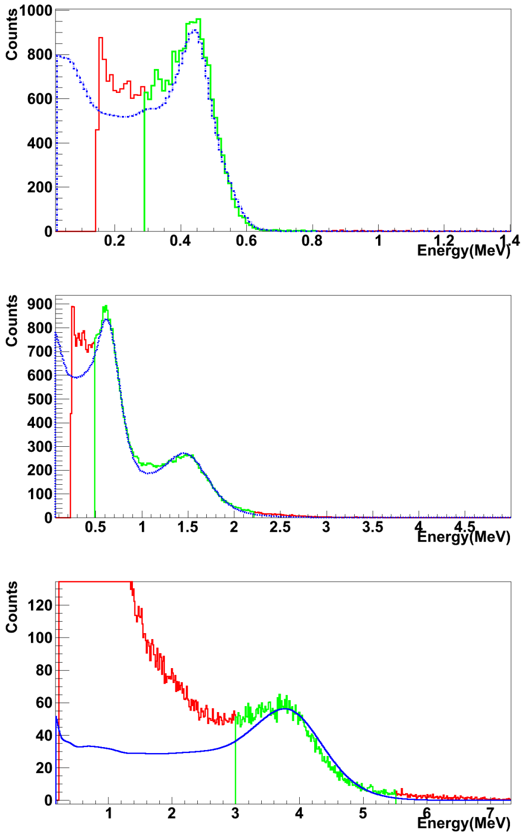

Figure 2.9: *From top to bottom: Calibration made with* ^{137}Cs*,* ^{88}Y *and Am/Be sources.*

2.4 Pulse Height Weighting Technique

The PHWT [17, 18] is based on an original idea from Maier-Leibnitz and was applied the first time by Macklin and Gibbons in 1967 [16]. This technique requires the use of a low efficiency γ-ray detector, such that only one γ-ray out of the capture cascade is registered,

$$\varepsilon_\gamma \ll 1, \tag{2.4}$$

and with detection efficiency ε_γ that is proportional to the photon energy E_γ:

$$\varepsilon_\gamma = \alpha E\gamma. \tag{2.5}$$

Under these conditions the efficiency for detecting a cascade ε_c will be proportional to the known cascade energy and independent of the actual cascade path,

$$\varepsilon_c \simeq \sum_j \varepsilon_{\gamma j} = \alpha E_C. \tag{2.6}$$

The proportionality of the efficiency with the γ-ray energy is achieved through the manipulation of the detector energy response distribution R(E) (or its energy binned equivalent R_i) by the introduction of a "pulse height" (i.e. deposited energy) dependent weighting factor W(E), which has to be applied to each registered count. The smooth, generally polynomial, dependence of the weighting factor on the energy is determined by a least-squares fit to a number of γ-ray responses in the energy range of interest:

$$min \sum_j (\sum_i W_i R_i^j - \alpha E_{\gamma j})^2. \tag{2.7}$$

The exact shape of the WF depends on the details of the experimental setup like the sample and the type of detector, and therefore, it can be only obtained by means of MC simulations. From eq. 2.7 we can calculate the goodness of the polynomial WF at each gamma ray energy E_j^γ by performing the weighted sum of its response function and check how much the ratio with the gamma energy differs from the unity (assuming α=1) [26]:

$$\frac{\sum_i W_i R_{i,j}}{E_j^\gamma} = 1. \tag{2.8}$$

To determine the WF uncertainty we have used the procedure described in the previous work [26], based on the MC simulation of a realistic nuclear cascade with a determined energy E_C. If W_i is the calculated WF and R_i^C is the response distribution of the simulated cascade C, for a big number of cascades N, it must be fulfilled that

$$\frac{\sum_i W_i R_i^C}{N E_C} = 1. \tag{2.9}$$

The deviation of this ratio from unity indicates the uncertainty introduced in the capture experiment due to the WF. In the following sections the procedure to obtain the response function and the calculation of the polynomial WF with the related uncertainty will be described.

2.5 Monte Carlo simulation of the response function and WF calculation

Photons in the energy range of the capture energy were simulated with isotropic emission from the sample and the primary and secondary particle were registered in the C_6D_6 detectors volume. The MC package used to perform this simulation was GEANT4 version 4.9.3 [27]. In this code a detailed geometric description of the setup, as described in section 2.2, was implemented. The experimental setup implemented in GEANT 4 is shown the Fig. 2.10.

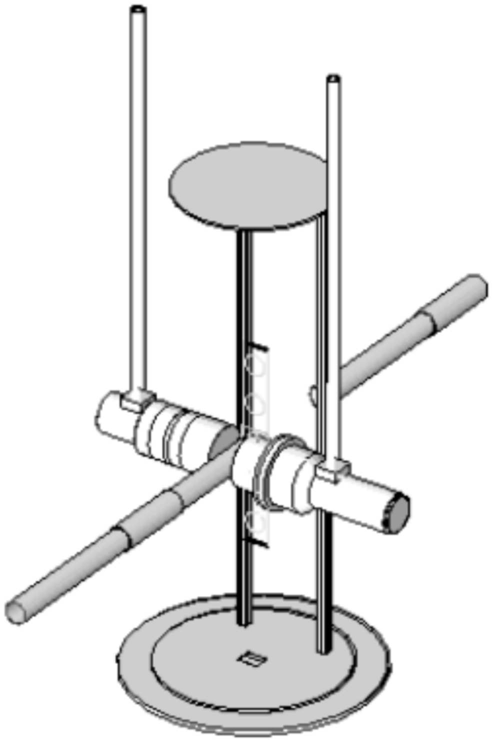

Figure 2.10: *Experimental setup as implemented in GEANT4.*

The geometric input for the simulation includes the sample, the main parts of the sample changer with the aluminum top and bottom flanges, the sample's carbon frame and all the supports in carbon fiber. For the simulation the standard electromagnetic package was used. The deposited energy distribution in the sensitive detectors volume was recorded for j=1,....N γ-ray energies E_j in the range from 50 keV to the neutron separation energy Sn. For each energy, 5×10^6 photons were sequentially and isotropically generated, randomly from the sample. In the simulation we took into account the radial distribution following the beam profile and a depth probability distribution was also included, considering the magnitude of the isotope's cross section. The deposited energy spectra were histogrammed with a bin of 10 keV, and the instrumental resolution was included in the simulated response using a Gaussian function of appropriate width [25]. In Fig. 2.11 and 2.12 the simulated response for the different gold and Iron samples are represented. Note the different response depending on the sample thickness.

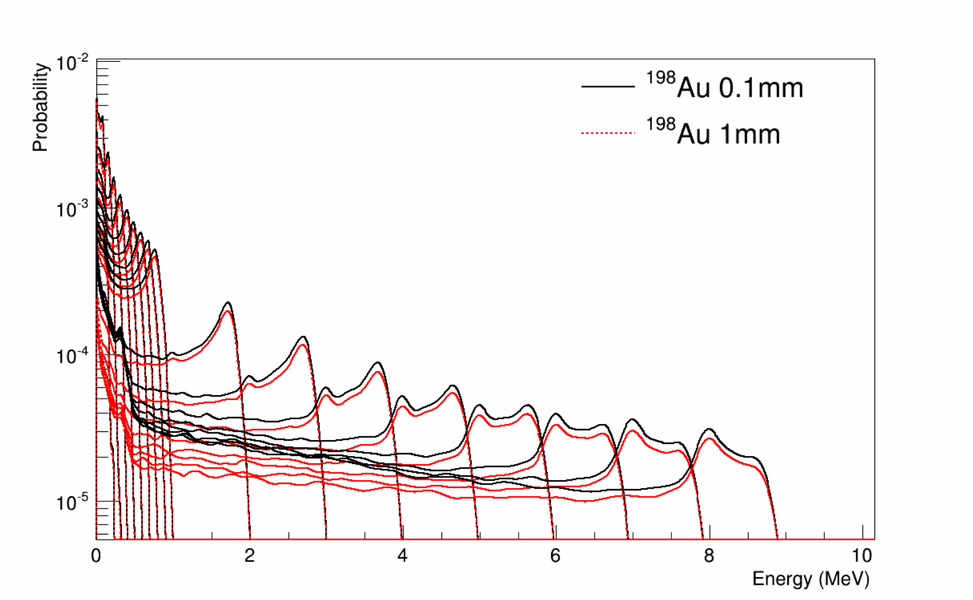

Figure 2.11: *Response function for the BICRON detector for the thin and thick gold samples.*

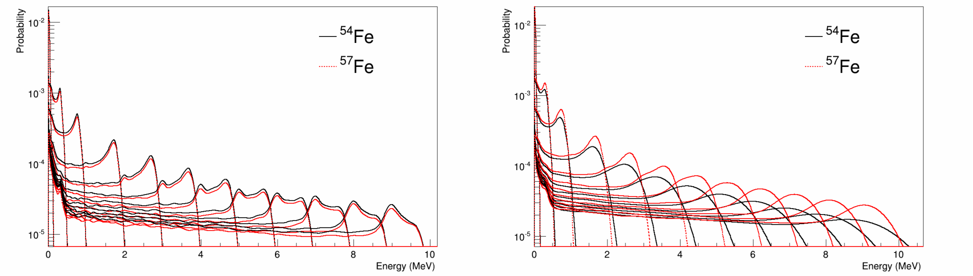

Figure 2.12: *Response function for BICRON(left) and FZK(right) for the different iron samples.*

The weighting functions are calculated using eq. 2.7 and assuming a fourth degree polynomial for the WF. The weighting functions calculated for the gold samples are shown in Fig 2.13.

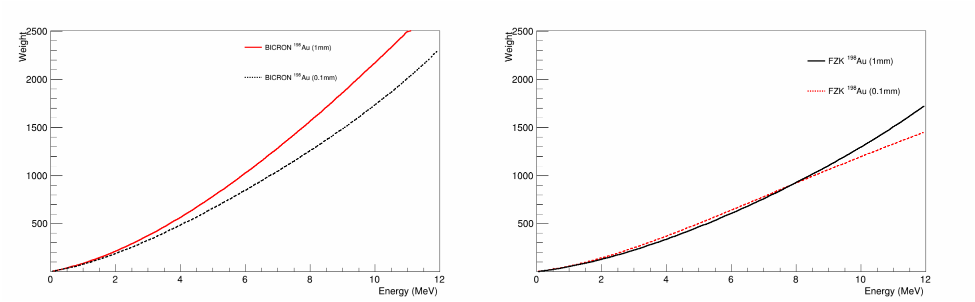

Figure 2.13: *Polynomial WF obtained for the gold samples. BICRON (left), and FZK (right).*

The goodness of the obtained WF is shown in Fig. 2.14 and 2.15 were the ratio of eq. 2.8 is displayed.

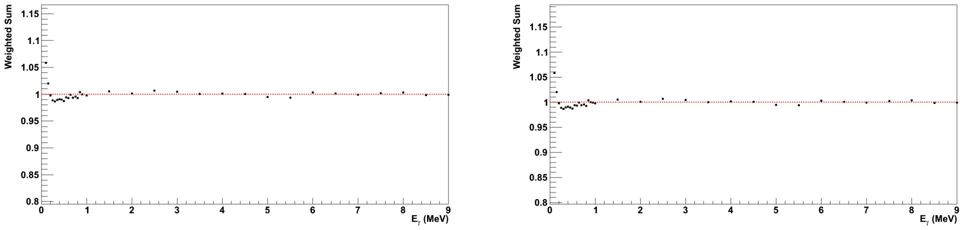

Figure 2.14: *Proportionality check for the thin gold sample, for BICRON(left) and FZK(right).*

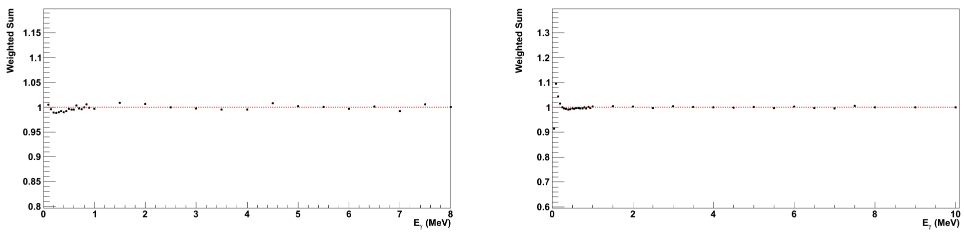

Figure 2.15: *Proportionality check for the thick gold sample, for BICRON(left) and FZK(right).*

The last figure shows a good performance of the WF along the whole energy range of interest. A big deviation is present at the energy of 50 keV and probably this is due to absorbed gamma rays. The RMS deviation for the FZK is 1.35% and 1.3% for the BICRON, in the case of the big sample. For the small sample the RMS deviation is 0.9% for the FZK detector and 0.94% for the BICRON detector. The plot for the polynomial WF obtained for the iron samples is represented in the Fig. 2.16, where the dashed line represents the response of the BICRON detector and the solid line is the FZK detector.

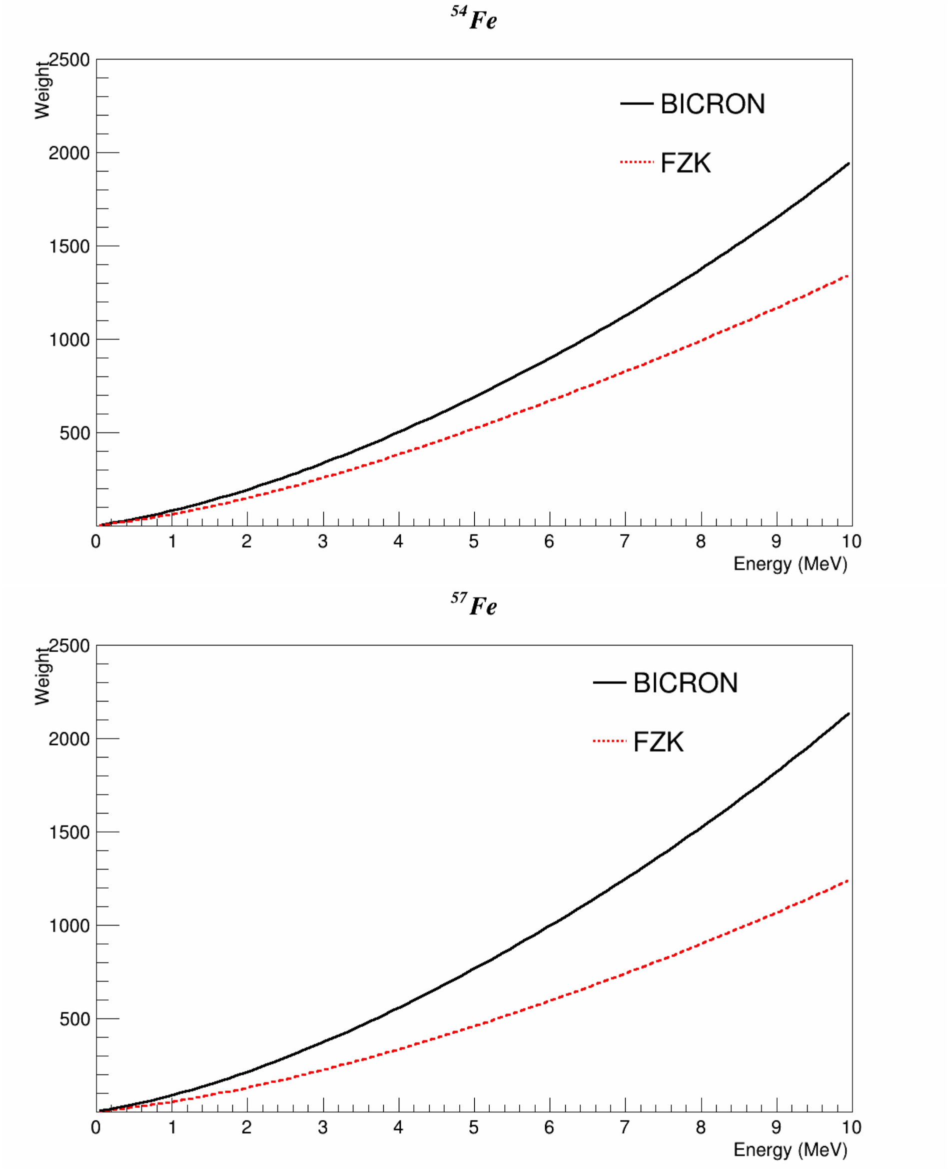

Figure 2.16: *Polynomial WF obtained for* ^{54}*Fe (top) and for* ^{57}*Fe (bottom).*

Fig. 2.17 and 2.18 show the goodness of the WF obtained for both iron samples.

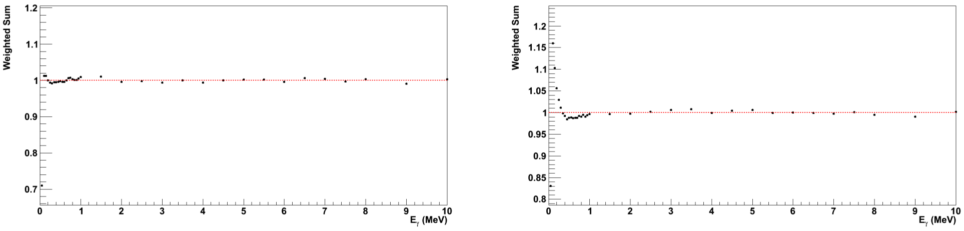

Figure 2.17: *Proportionality check for the* ^{54}*Fe, BICRON (left) and FZK (right).*

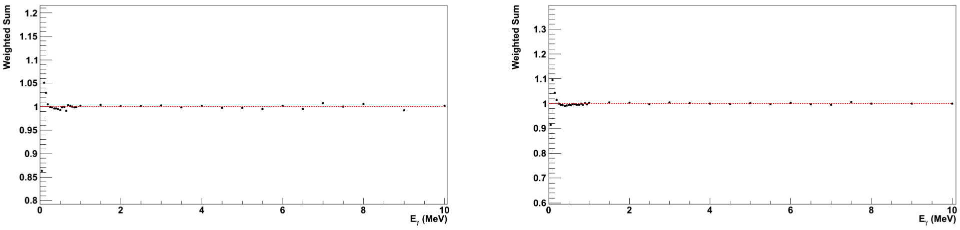

Figure 2.18: *Proportionality check for the* ^{57}*Fe, BICRON (left) and FZK (right).*

The RMS deviation for the BICRON detector is 0.75% and 0.18% for the FZK detector, in the ^{54}Fe measurement. The RMS deviation for the BICRON detector is 0.2% and 0.074% for the FZK detector, in the ^{57}Fe measurement.

2.5.1 MC Simulation of capture events and WF uncertainty

In order to determine the uncertainty of the calculated WFs we use the method described in the previous work [26], based on the MC simulation of realistic nuclear cascades with a total energy E_C, where at most one of the prompt gamma rays is detected. This method is also used in order to determine yield correction factors connected with the detection threshold of the C_6D_6 detectors and other systematic effects, which are described later. Let W_i be the calculated WF and R_i, c the response distribution of each simulated cascade c. Then,for a large number of cascades N and an exact WF it should be fulfilled that the weighted sum is equal to the number of cascades times the capture energy,

$$\sum_{c=1}^{N}\sum_{i=1}^{n} W_i R_{i,c} = NE_C. \tag{2.10}$$

Deviations of the weighed sum (left term in eq. 2.10) from NE_C indicate the uncertainty due to the calculated W_i. The computer program [17] was used in order to generate realistic cascade events. For each capture nucleus a known low excitation energy level scheme is defined, consisting of a set of complete levels with spin-parity and branching-ratios. At high energies a statistical model of the nucleus is used to generate a level scheme. Levels of appropriate spin and parity are generated from a level density formula by introducing fluctuation of the Wigner type. The strength functions for E_1, M_1, and E_2 radiation are generated by a giant dipole resonance (GDR), and have a form of a standard Lorentzian [28].

$$f_{XL}^{SLO}(\varepsilon_\gamma) = \frac{26\times10^{-8}}{2L+1}\sigma_o \Gamma E_\gamma^{(3-2L)} \frac{\Gamma_o}{(E_\gamma^2 - E_o^2)^2 + E_\gamma^2 \Gamma_o^\gamma)} [mb^{-1} MeV^{-2}]. \tag{2.11}$$

The transmission coefficient $T_{XL}(\varepsilon_\gamma)$ of the gamma ray emission is described in reference [29] and given by the relationship:

$$T_{XL}(\varepsilon_\gamma) = 2\pi\varepsilon_\gamma^{(2L+1)} f_{XL}(\varepsilon_\gamma) \tag{2.12}$$

In the code are included three model for the level density. The parametrizations included in the code for the level density are:

- Back shifted Fermi Gas (Dilg et al.) [30].
- Constant temperature (Von Egidy et al.) [31].
- Combined BSFG + CT (Gilbert-Cameron) [30].

With this code a list of capture events is generated, which is subsequently used as input to the GEANT4 code. Each generated event consists of a list of gamma ray energies, and eventually X-ray and electron energies. A GEANT4 simulation was performed with the proper cascade events and geometrical description for each sample used in the capture experiments. The instrumental resolution of the C_6D_6 detectors was included in the simulated spectrum as mentioned before, and the simulated response are histogrammed and compared with the experimental ones. This simulation was performed for the two gold samples exactly in the resonance energy at 4.9 eV. For the iron sample we simulated one resonance for each spin group and parity. To obtain the experimental energy deposited spectra in the detectors we put a time of flight window around the energy of 4.9 eV. After a detailed simulation and comparison we found that the best agreement is obtained using the Constant Temperature level density parametrization of Von Egidy et al. [31]. The comparison between the simulated spectra and the experimental energy spectra are shown in the Fig. 2.19.

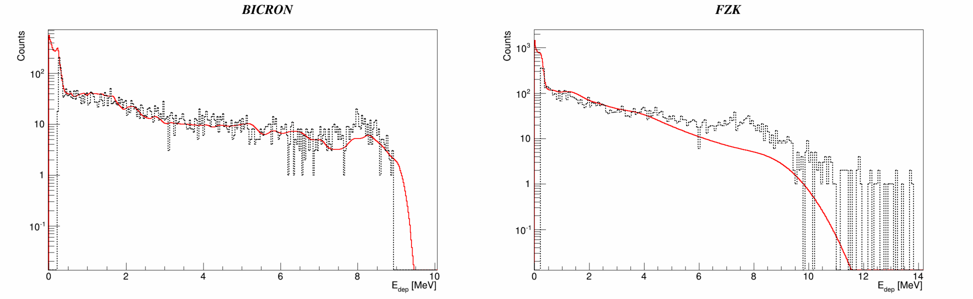

Figure 2.19: *Comparison between the simulated and the experimental spectra for the BICRON(left) and FZK(right) detectors.*

In Fig. 2.19 we can verify the good performance obtained using the cascade generator code to obtain the cascade response (dashed line) for the resonance at 4.9 eV in the gold and the good agreement with the experimental spectra.

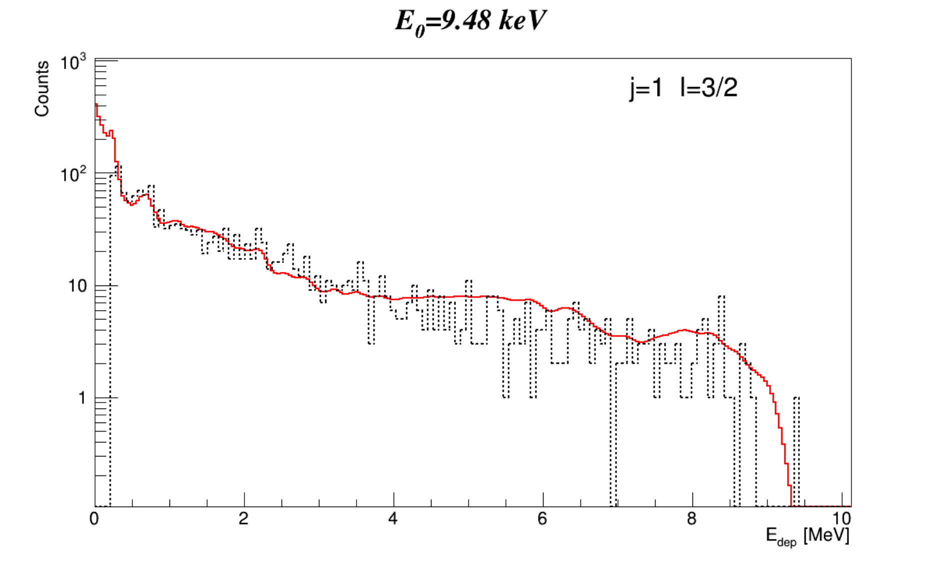

Figure 2.20: *Simulated response spectra at 9.48 keV for* ^{54}*Fe.*

In Fig. 2.20 a comparison between the simulated spectra (solid line) and the experimental one (dashed line) for the resonance at 9.48 keV in ^{54}Fe is represented. In this case good agreement is obtained also using the same level density parametrization adopted for the gold sample.

2.5.2 WF uncertainty

A total of N = 1 $\times 10^6$ capture cascades are generated for each sample investigated in the experiment(see table 2.1). The γ-rays generated from the cascade are emitted simultaneously in the GEANT4 simulation and the response distribution is recorded and convoluted including the instrumental resolution. Using the WF obtained for the sample under study and the simulated response obtained from a realistic cascade generated by the "cascade generator", the uncertainty can be calculated using the eq. 2.9.

The results obtained for the gold and iron samples are listed in the table 2.3 and 2.4 respectively.

Detector	Sample thick ×diam. (mm)	$\sum_i W_i R_i^C$	$\frac{\sum_i W_i R_i^C}{NE_C}$
BICRON	^{197}Au 1 × 20.03	4167000	1.00479
BICRON	^{197}Au 0.1 × 19.97	4157400	1.00247
FZK	^{197}Au 1 × 20.03	4122210	0.995
FZK	^{197}Au 0.1 × 19.97	4162190	1.00363

Table 2.3: *Estimated uncertainty on the WF for the gold samples.*

Detector	Sample thick ×diam. (mm)	$\sum_i W_i R_i^C$	$\frac{\sum_i W_i R_i^C}{NE_C}$
BICRON	^{54}Fe 20.11 × 0.86	7576690	0.9982
BICRON	^{57}Fe 19.95 × 0.64	4039700	1.00823
FZK	^{54}Fe 20.11 × 0.86	7575100	0.9974
FZK	^{57}Fe 19.95 × 0.64	3972160	0.992

Table 2.4: *Estimated uncertainty on the WF for the iron samples.*

Small variation of the deposited energy calibration have a considerable effect on the value of $\sum_i W_i R_i^C$, however this deviation is cancelled out when computing the ratio with the Au reference sample. Finally a 0.46% is adopted as the uncertainty associated with the polynomial WF of the sample listed in table 2.1.

Chapter 3

Data reduction

3.1 Capture Yield

Capture yield is defined as the fraction of neutrons intersecting the sample and undergoing a capture reaction [32].

The number of counts registered in a capture experiment, N, depend of the time of flight (TOF) and on the pulse height (A) and can be expressed as:

$$N = N(t_{TOF}, A). \tag{3.1}$$

Using this definition we can express the number of counts as:

$$N(E_n, E_{dep}) = Y \times N_n(E_n) \times \varepsilon(E_{dep}), \tag{3.2}$$

where Y is the capture yield, N_n is the number of incoming neutrons and ε is the detector efficiency. E_n is the neutron energy derived from the measured time of flight (TOF) and E_{dep} is the energy deposited in the C_6D_6 volume, obtained from the pulse eight (A). Therefore N_n, represents the time integrated neutron flux $\phi_n$crossing the sample of surface S,

$$N_n = \int_s \int \phi_n dSdt. \tag{3.3}$$

As mentioned in chapter 2, the dependence on the efficiency must be avoided since it means a cascade detection probability dependent on the deexcitation path. This can be achieved by applying the PHWT .

Now eq. 3.2 can be expressed as:

$$N^W(E_n) = \sum_{E_{dep}} W(E_{dep}) \times N(E_n, E_{dep}) = Y \times N_n(E_n) \times E_C(E_n). \quad (3.4)$$

The term $W(E_{dep})$ is the calculated weighting function, and as described in the previous chapter it is different for each sample used in the capture experiment, and the term E_C represents the energy of the cascade $E_C = S_n + E_n$, where S_n is the neutron separation energy of the sample under investigation.

Finally, considering the last expression the experimental capture yield is given by:

$$Y(E_n) = \frac{N^W(E_n)}{N_n(E_n) \times (S_n + E_n)}. \quad (3.5)$$

The absolute value of the neutron flux is difficult to obtain. Therefore, the capture yield is always measured with the respect to a reference sample.

This is the general procedure to determine the cross section using the PHWT and it is based on the saturated resonance method. This method will be described in the section 3.7. Furthermore, there are some important factors to take into account during the extraction of the yield:

$$Y'(E_n) = Y(E_n) \times f^{t,s,CE} \times f^{sat} \times f^{ns}. \quad (3.6)$$

The therm f^{sat} is the correction factor obtained by the saturated resonance method, f^{ns} is the neutron sensitivity correction factor and the $f^{t,s,CE}$ is the correction mostly due to the loss of counts below the electronic threshold. The latter contains also summing and conversion electron corrections.

3.2 The data acquisition system DAQ

The n_TOF data acquisition system (DAQ) has been designed on the basis of high performance Flash Analog to Digital Converter (FADC) [33] which are able to record the digitized detector pulses for each neutron bunch. The relevant parameters of the electronic signals such as time of flight or signal amplitude and area are calculated by means of an offline pulse shape analysis algorithm for every detector type [34]. The n_TOF DAQ consists of 44 FADC channels with 8-bit resolution, sampling rates up to 2 GHz and 8 or 16 Mbyte memory. Each detector in the experimental setup is coupled to one FADC channel. The pulsed structure of the CERN PS allows the DAQ to be triggered by the impact of the proton beam on the spallation target. The trigger opens a 16 ms time window where neutrons from thermal (∼meV) up to several GeV can be measured. The set of signals corresponding to one detector and one proton pulse is formatted in a data buffer, grouped into a data stream and saved on a local temporary disk pool in the corresponding raw data stream files. An Event Display program allows the raw data files to be read from the local disk pool and the digitized signals of all detectors present in the setup to be visualized for online control and monitoring of detector performance. After a raw data file is closed, it is transferred to CASTOR (Cern Advanced STORage system) [35]. A block diagram of the n_TOF DAQ is illustrated in the Fig. 3.1

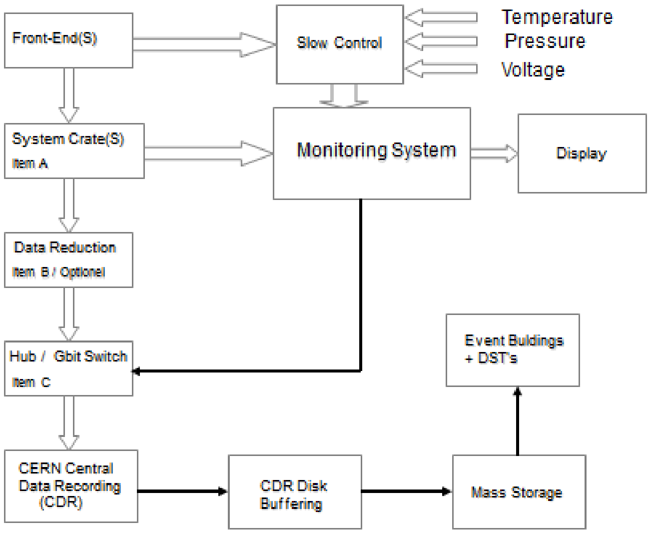

Figure 3.1: *Block diagram of n_ TOF DAQ [19].*

3.3 The raw data processing

After a raw data file is migrated to tape, it is mirrored to a disk pool and it is read-out by the Data Processing Software (DPS) and processed.

The relevant parameters of the electronic signals such as time of flight or signal amplitude and area are calculated by means of an offline Pulse Shape Analysis (PSA) algorithm for every detector type.

The raw data processing consists of the pulse shape analysis of the different FADC data sets corresponding to the detectors coupled to the DAQ, and runs in batch mode at CERN's batch services LXBATCH [36]. Digital Pulse Shape Analysis (DPSA) algorithms are available for the different detectors used at n_TOF with specific features in order to extract the parameters of physical relevance from the data buffers. Specific algorithms written in C++ are available for each individual detector type. The relevant signal parameters such as time, energy and quality factors are extracted from the pulse shapes, formatted and saved as Data Summary Tapes (DSTs).

The DSTs are stored on disk, and the data format is based on the BOS bank system [37] .

The quality of the analysis for the particular case of the C_6D_6 liquid scintillators is illustrated in Fig. 3.2 by the comparison of the FADC output(continuous line) and the reconstructed signal (dashed line) which is obtained by an iterative baseline correction and a least-squares fit of the digital signals to a reference C_6D_6 pulse shape.

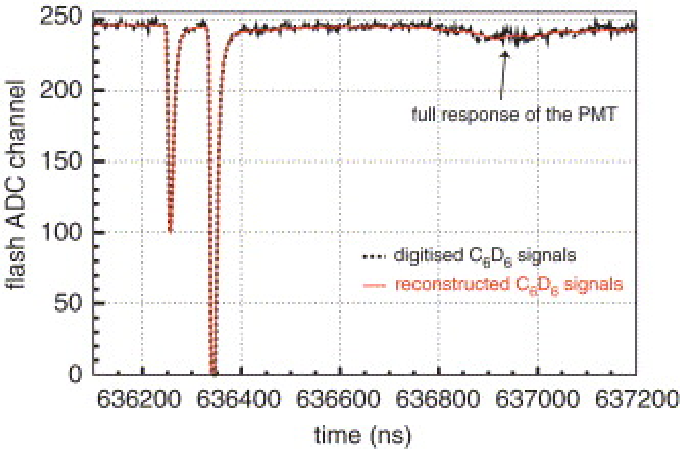

Figure 3.2: *Reconstructed signals for* C_6D_6 *using the pulse shape analysis.*

To access the DST files a software tool is available in order to process this information, select valid events by applying specific cuts and to have the possibility to save all this information in histograms to be used in the next step of the analysis, for example to obtain the capture yield or some specific spectrum.

In Fig. 3.3 a flow diagram to obtain the final data is showed.

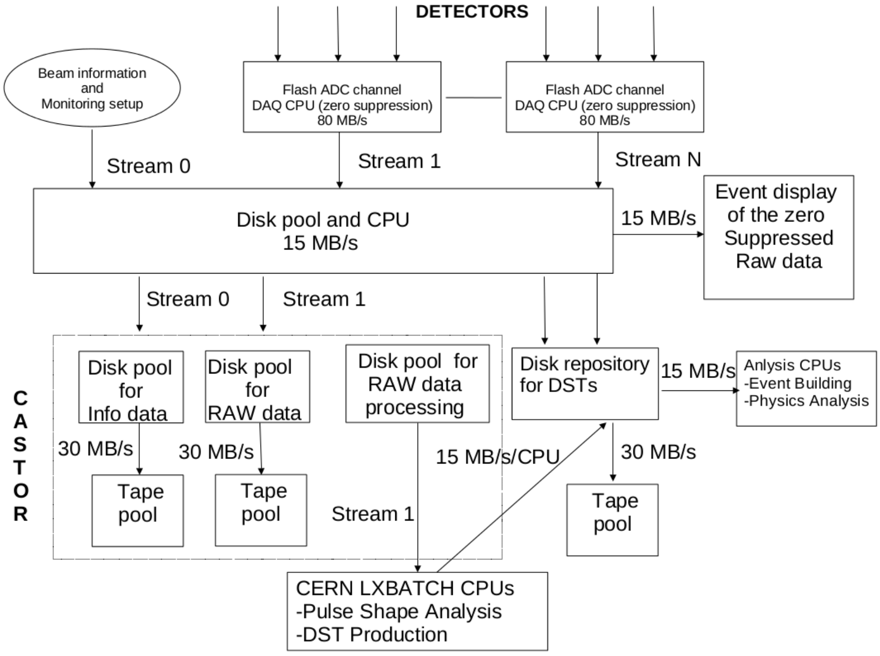

Figure 3.3: *Schematic data flow from detectors to tape and to data processing[19].*

3.4 Consistency tests of counts rates

The first step to select the runs to use in the analysis is to check the counting rate between the two C_6D_6 detectors.To compare better the count rate is convenient to apply some “cuts” in the data. The counting rates of C_6D_6 detectors correspond to neutron energies from 1 eV to 100 keV. This condition is applied to exclude the possibility of big baseline fluctuations in the high neutron energy range.

In Fig. 3.4 the count rate of the two C_6D_6 and the four Silicon detectors during several runs for the ^{54}Fe measurement is shown.

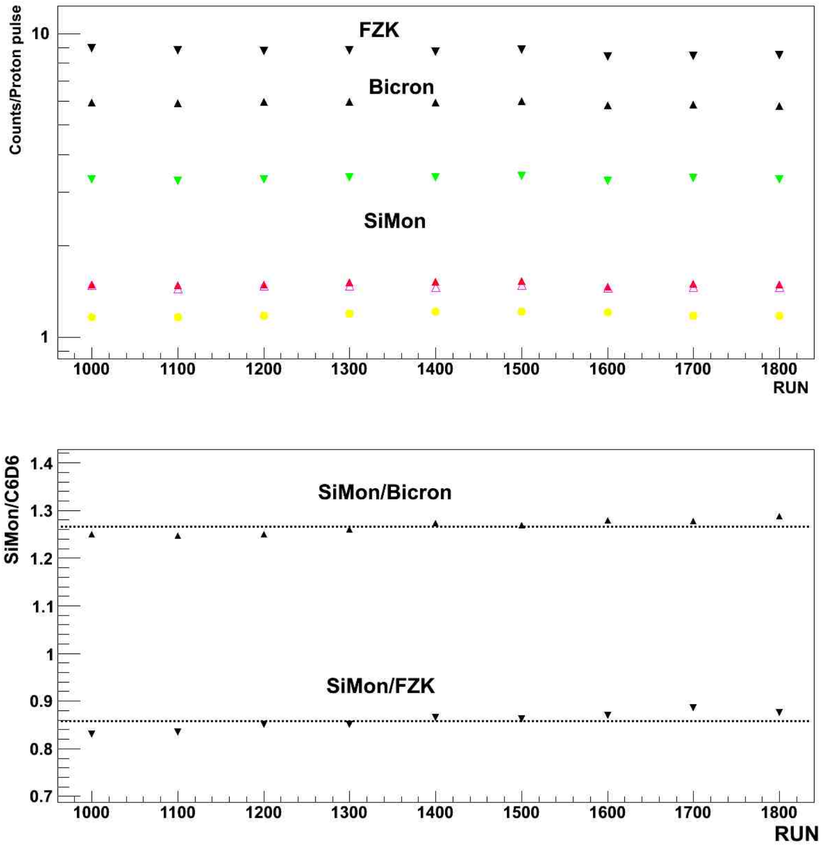

Figure 3.4: *Count rate of all detectors involved in the capture experiments (Top). Ratio of the count rate between the Silicon monitor and the* C_6D_6 *detectors (bottom).*

The higher count rate for the FZK detector is due to its bigger volume with respect to the BICRON detector. The relevant information is that both detectors show a proportional counting along the measuring time. This proportionality is better shown in the bottom part of the figure by plotting the relative ratio.

The count rate is divided for the number of protons in the pulse and the electronic threshold is 250 keV for both scintillator detectors.

The previous check allows to identify possible systematic deviations. In addition to the low energy threshold, a high energy cut is also applied to exclude high energy signal sources of background.

3.5 Time of flight energy relation

The technique is based on a pulsed neutron source, where the energy of the neutron inducing a detected reaction is determined by:

$$E_n = \frac{1}{2} m_n v^2 = \left(\frac{72.2977 L}{t} \right)^2 , \tag{3.7}$$

This equation shows the relation between time and the neutron energy.

In eq. 3.7 E_n is the neutron energy expressed in eV, L is the effective flight path in meters and t is the time of flight in μs.

The effective flight path includes the geometrical distance between the neutron source and the sample and also the average moderation path followed by the neutron inside the lead block and the borated water moderator.

The effective flight path depends on E_n because the moderation process varies with the neutron energy and L can be written as the sum of two terms:

$$L = L(E_n) = L_0 + \triangle L(E_n). \tag{3.8}$$

The term L_0 present in the last equation includes any constant term of the moderator distance and represents the geometrical distance between the sample and the outer face of the moderator.

It was demonstrated [38] that the addition of the term $\triangle$L to the constant distance L_0 is equivalent to add a constant time offset t_0, to the measured time of flight t.

In this way the equation 3.8 can be written as:

$$E_n = \frac{1}{2} m_n v^2 = \left(\frac{72.2977 L_0}{t + t_0} \right)^2 . \tag{3.9}$$

Note that this expression neglects relativistic effects and is, therefore,valid only below about 1 MeV.

In order to obtain the calibration parameters L_0 and t_0 a set of standard resonances have been measured [38].

3.6 Neutron Flux

The n_TOF neutron fluence has been analyzed from the data of the SiMon (^{6}Li), MGAS (^{10}B and ^{235}U) and PTB (^{235}U) [39] detectors which were described in chapter 2.

The neutron intensity, expressed as $neutrons/pulse/ln(E_n)$ is calculated from the measured counting rates as:

$$\phi(E_n) = \frac{C(E_n)}{\varepsilon_{det}(E_n) \cdot Y_{n,x}(E_n) \cdot ln\left(\frac{E_n + \triangle E_n}{E_n}\right)} \tag{3.10}$$

where C is the measured counting rate in count/pulse, ε_{det} is the detection efficiency as function of the neutron energy, $Y_{n,x}$ is the expected reaction yield, and $ln(E_n + \triangle E_n / E_n)$ is the width of the energy interval in isolethargic units.

This evaluated value is the weighted average of different detectors in different energy ranges.

Energy range	Detector Used
20 meV-1 eV	SiMon (^{6}Li), MGAS (^{10}B and ^{235}U), PTB (^{235}U)
1 eV- 3 keV	SiMon (^{6}Li), MGAS (^{10}B)
3 keV- 27 keV	SiMon (^{6}Li), MGAS (^{10}B and ^{235}U), PTB (^{235}U)
27 keV- 10MeV	PTB (^{235}U)

Table 3.1: *Detectors used for the calculation of the evaluated fluence in different neutron energy ranges.*

In Fig. 3.5 the adopted neutron flux is represented.

The dip present at 300 eV is due to the absorption of neutrons in the manganese impurity of the aluminum alloy window crossed by the beam at the exit of the spallation target.

The fluence above 10 keV is clearly dominated by transmission dips from Aluminum layers along the beam line, mainly those surrounding the spallation target and that at the beginning of the neutron beam line.

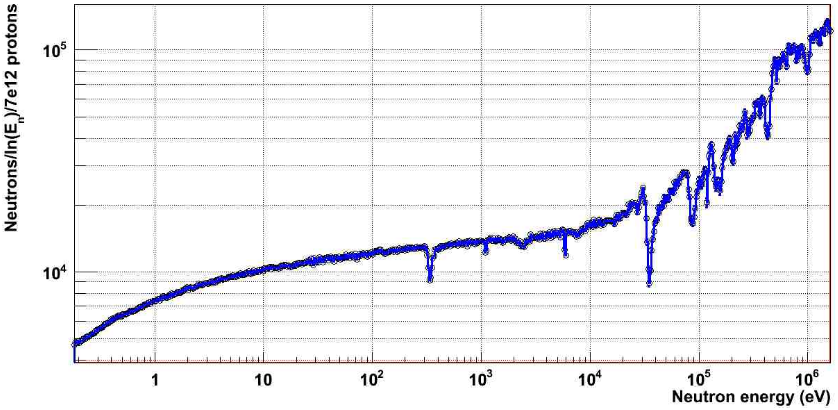

Figure 3.5: *Neutron flux at n_ TOF.*

3.7 Saturated resonance method

As mentioned in section 3.2 the determination of the capture yield depends on the detection efficiency ε and the neutron intensity I_n.

In the saturated resonance method [40, 41], the theoretical and the observed capture yields are compared for a particular resonance where the peak cross-section and the sample thickness must be large enough for the resonance to be saturated at the top $(1-e^{-n\sigma_{tot}}) \to 1$, and the capture to scattering cross-section ratio are large enough so that the saturation value $(Y_{n,\gamma}^{sat} \sim \sigma_\gamma/(\sigma_\gamma+\sigma_n))$ can be determined accurately in the plateau region.

From equation 3.5, the experimental yield for the reference resonance can be obtained by:

$$Y_{ref}^{exp}(E_n) = \frac{N_{ref}^{w}(E_n)}{N_n(E_n) \times (S_n^{ref} + E_n)}. \tag{3.11}$$

The yield for this resonance can be accurately calculated if its cross section is well known and the sample is indeed thin.

For this purpose we used the well-known resonance of ^{197}Au at 4.9 eV for the yield calibration.

In this case the transmission is very small and the multiple scattering is the main source of neutron losses. To calculate the yield related to this resonance we have used the code SAMMY [42] which takes into account those effects.

Fig. 3.6 is shows an example of the resonance at 4.9 eV for the ^{197}Au (n,γ) reaction.

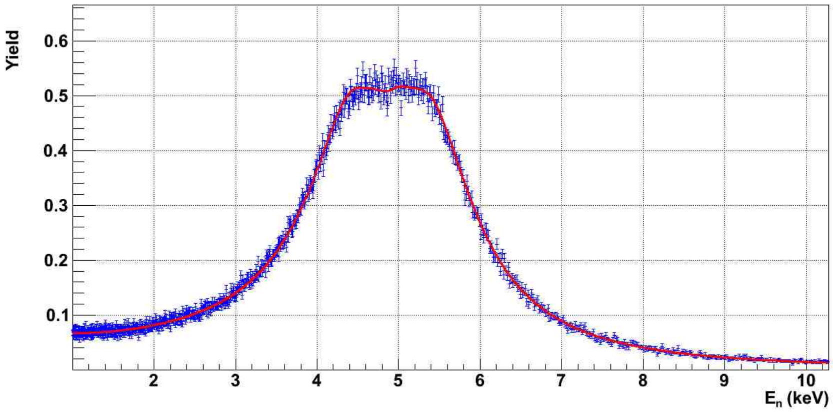

Figure 3.6: *4.9 eV ^{197}Au resonance fitted with SAMMY and used for yield calibration.*

The data points correspond to the experimental yield, and the solid line to a function with the form $AY^{th}_{ref} + B$, where the parameters A and B were fitted to obtain:

$$Y^{exp}_{ref}(E_n) = AY^{th}_{ref}(E_n) + B \rightarrow f^{sat} = 1/A. \tag{3.12}$$

The yield normalization factor, f^{sat}, is given by the inverse of the fitting parameters A.

The term B is a constant which accounts for the background.

When the reference samples have different diameters than the samples employed in the capture experiment, the neutron beam profile is needed in order to correct the different flux seen by the sample under study. The n_TOF beam profile was determined using the MicroMegas detector as described in the chapter 2 [43].

3.8 Sources of systematic uncertainty

In the measurement of (n,γ) cross sections using the PHWT, there are four effects which need to be taken into account. These effect are:

- Pile-up: This situation occurs when two signals overlap and can not be distinguished as two independent pulses [44].

- Threshold effect: This effect occurs because during a capture experiment the detectors register counts only above an electronic threshold. In this way, signals with a small amplitude are not registered, but they have to be taken into account in the final capture yield. An estimation of how much the experimental yield is affected by the counts lost at low energy is given by:

  $$\sum_{i=0}^{\infty} W_i R_i^C / \sum_{i=t}^{\infty} W_i R_i^C \tag{3.13}$$

  where R_i^C are the simulated response for N simulated cascade, and the first term take into account a zero electronic threshold.

- $\gamma-$summing: This effect happens when more than one gamma ray is detected by the same detector, usually is very small and depends on the isotope under study.

- Internal conversion electron (CE) process: This effect occurs when a gamma transition is absorbed by an electron emission and the X-ray generated can be stopped by the detector material and deposit a small quantity of energy [45].

3.8.1 Global Correction factor

This correction factor takes into accounts all the effects mentioned above in a simultaneous way.

The contribution of the CE process in the yield is very small and negligible in our cases. The global correction factor is given by:

$$f^{t,s,CE} = \frac{\sum_{i=0}^{\infty} W_i R_i^C}{\sum_{i=t\,keV}^{\infty} W_i R_i^{C,Sim}}. \tag{3.14}$$

where R_i^C corresponds to the response function for a certain number of N cascades, where the $\gamma-$rays are emitted sequentially and no CE process is included.

$R_i^{C,Sim}$ corresponds to the response function for cascades, where $\gamma-$rays are emitted simultaneously and CE is included.

The resulting correction factor for the gold samples measured in this experiment and the relative threshold level for each detectors are summarized in table 3.2.

Detector	Sample	$f^{t,s,CE}$	Electronic Threshold
BICRON	^{197}Au (20 ×1 mm)	1.07788	250 keV
BICRON	^{197}Au (19.93 × 0.1 mm)	1.08392	300 keV
FZK	^{197}Au (20 ×1 mm)	1.07371	250 keV
FZK	^{197}Au (19.93 × 0.1 mm)	1.07788	300 keV

Table 3.2: *Correction factor obtained for the Gold reference samples.*

3.9 Neutron sensitivity

A detailed investigation about the neutron sensitivity of the detectors employed in our measurement was carried out, in ref. [21]. These results have been obtained by Monte Carlo simulation and cross checked experimentally.

A new set of Monte Carlo simulation using the GEANT4 package and a new neutron library [46] were performed, in the present work, and are in agreement with the previous results.

In Fig. 3.7 is shown the neutron sensitivity as function of the neutron energy for different kinds of scintillator detector. We can define the probability that a registered signal is due to a neutron captured in the detector material rather than a gamma ray coming from a capture process as:

$$P^{ns} = \left(\frac{\varepsilon_n}{\varepsilon_c}\right)\left(\frac{\Gamma_n}{\Gamma_\gamma}\right), \tag{3.15}$$

where ε_c is the probability to detect a gamma ray from the cascade and ε_n is the neutron detection efficiency.

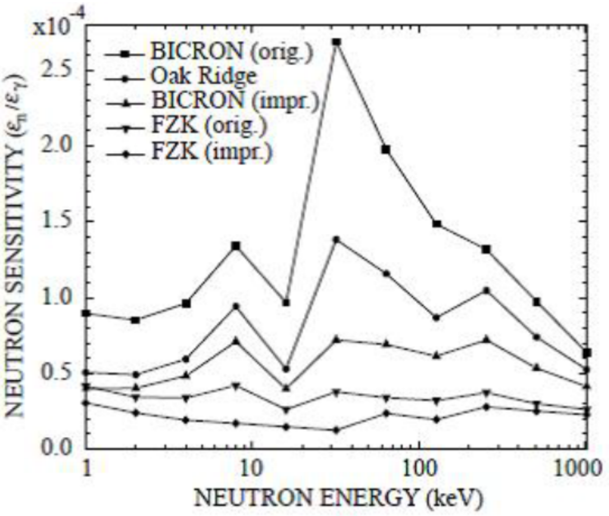

Figure 3.7: *Comparison of the simulated neutron sensitivities between the improved FZK and BICRON detectors, versus other scintillator detectors* [21].

It is important to remark that the quantity $\varepsilon_n/\varepsilon_c$ is not the same represented in fig 3.7, where ε_γ is the maximum gamma efficiency obtained from MC simulation at energy of 600 keV [21].

Γ_n and Γ_γ are the chances for a neutron to be captured and scattered respectively.

Under this assumption the final yield should be corrected by:

$$f^{n,s} = \frac{1}{1+P^{ns}}. \tag{3.16}$$

The cascade efficiency ε_c is approximately the sum of the efficiency of each gamma ray coming from the cascade:

$$\varepsilon_c \approx \sum_i \varepsilon_{\gamma,i}. \tag{3.17}$$

Under this consideration the equation 3.16 can be expressed as:

$$P^{ns} = \left(\frac{\varepsilon_\gamma}{\varepsilon_c}\right)\left(\frac{\varepsilon_n}{\varepsilon_\gamma}\right)\left(\frac{\Gamma_n}{\Gamma_\gamma}\right) = f^{gc}\left(\frac{\varepsilon_n}{\varepsilon_\gamma}\right)\left(\frac{\Gamma_n}{\Gamma_\gamma}\right), \tag{3.18}$$

where f^{gc} is the ratio between the probability to register a gamma ray of 600 keV and the probability to detect the prompt cascade coming from the corresponding energy resonance.

To evaluate this term, capture cascades were generated by MC simulation for each energy resonance where neutron sensitivity effects could be present.

Table 3.3 summarizes the most critical cases analyzed and the corresponding f^{gc} obtained from the corresponding MC simulation.

Nuclide	Energy	J	l	Γ_n/Γ_γ	f^{gc}
^{54}Fe	7.8 keV	1/2	0	598	0.5
^{54}Fe	130 keV	1/2	0	1196	0.5
^{57}Fe	6.26 keV	1	0	332	0.358
^{57}Fe	28.94	1	0	976	0.358

Table 3.3: *Parameters from references [46, 47].*

The accuracy of this correction is due to the uncertainty on $\varepsilon_n/\varepsilon_\gamma$, which is of about 12% [21], plus the uncertainty on the factor Γ_n/Γ_g.

The final correction factor for the energies resonances of ^{54}Fe and ^{57}Fe reported in table 3.3 was calculated through an iterative procedure by deriving the value of Γ_γ from the experimental yield and calculating the corresponding P^{ns} correction using the resonance parameters from reference [46, 47].

The value for the neutron sensitivity correction obtained for each resonance tabulated in table 3.3 are shown in table 3.4.

Detector	Energy	P^{ns}
FZK (improved)	7.8 keV	0.00538
BICRON (improved)	7.8 keV	0.0208
FZK (improved)	130 keV	0.012
BICRON (improved)	130 keV	0.036
FZK (improved)	6.26 keV	0.0023
BICRON (improved)	6.26 keV	0.007
FZK (improved)	28.94 keV	0.00592
BICRON (improved)	28.94 keV	0.0136

Table 3.4: *Neutron sensitivity effect calculated for some energy resonance.*

For the calibration resonances of gold samples the corresponding correction is negligible.

In summary, the largest correction is of ∼3.6% for the 130 keV resonance when measured with the BICRON detector.

3.10 R-matrix analysis

The measured cross-section is parametrized by means of nuclear reaction theory. In our case, in the range of the resolved resonance energy the R-matrix theory is employed [49].

There are several approximations of R-matrix formalism, but the multi-level Reich-Moore [20, 50] formalism is considered the best.

When the experimental yield is obtained there are several experimental effects that are difficult to correct. For this reason, it is convenient to include many effects into the calculation of the theoretical yield. Thus, "self-shielding" and "multiple-scattering" effect, must be included in the calculated theoretical yield [32].

Under this assumption the capture yield can be written as the sum of some components from multiple collision events:

$$Y(E) = Y_0(E) + Y_1(E) + ... \tag{3.19}$$

The first term present in equation 3.19 is the self-shielding which describes the reduction in the observed capture cross section, due to interactions of incident neutrons with other nuclei in front of the current position.

The term Y_0 can be expressed by:

$$Y_0 = \{1 - e^{n\sigma}\}\left(\frac{\sigma_\gamma}{\sigma}\right) \tag{3.20}$$

where σ is the total cross section and $e^{n\sigma}$ is the fraction of neutrons that traverses the sample of areal density n without interacting.

For a very thin sample, the therm $n\sigma \ll 1$ in the capture yield could be approximated to the first term $Y_0(E)$.

In general we have to take into account the multiple collision term. This effect leads to an increase in the observed capture cross section at a given energy due to capture of higher energy neutrons that have been scattered out of the original beam path. In this case a detailed MC simulation is needed to calculate and estimate such effects.

In the last case the second term of the equation 3.19 can be expressed as:

$$Y_1(E) = \{1 - e^{n\sigma}\}\left(\frac{\sigma_\gamma}{\sigma}\right)\left\langle\{1 - e^{n\sigma}\}\left(\frac{\sigma_{\gamma 1}}{\sigma_1}\right)\right\rangle. \tag{3.21}$$

Another important effect to consider is the thermal broadening related to the thermal motion of target nuclei. The mathematical approach to calculate this effect is to assume that the target nuclei have the same velocity distributions as the atoms of an ideal gas which follow the Maxwell-Boltzman distribution. Following some approximation this broadening effect can be included as a Gaussian broadening of the reaction rate with a width called Doppler width given by:

$$\triangle = \sqrt{\frac{4mEkT}{M}}, \tag{3.22}$$

where M is the mass of the target, k the Boltzman's constant and T is the effective temperature.

Angular distributions (elastic, inelastic, or other reaction), cross sections for incident neutrons can be also calculated from Reich-Moore resonance parameters.

3.11 R-matrix code SAMMY

For the analysis of the capture data the SAMMY code, version 8, was chosen [42].

Analysis of neutron cross-section data in the resolved resonance region (RRR) has distinct aspects, each of which must be included in any analysis code:

- An appropriate formalism is needed for generating theoretical cross sections.
- An appropriate mathematical description must be provided for every experimental condition.
- A fitting procedure must be available to determine the parameters values which provide the best fit of theoretical to experimental one.

This code permits to include Doppler and resolution broadening, multiple-scattering corrections for capture or reaction yields, normalizations and backgrounds.

The code is implemented with several approximations of R-matrix formalism but, as mentioned before, we have chosen the Reich-More formalism.

The fitting procedure is Bayes' method. Data and parameter covariance matrices are properly treated within the code. Parameters of different isotopes can be included in the input files in order to take into account the presence of impurities in the sample under study.

The resolution function RPI reproducing the n_TOF neutron beam resolution is implemented in the code [20, 50].

3.12 Analysis for the 4.9 eV ^{197}Au energy resonance

In this section the procedure followed to obtain the yield normalization factor from the ^{197}Au reference sample is described.

The experimental setup was illustrated in chapter 2, and I remark that the measurement was performed using one BICRON detector and one FZK detector.

The experimental yield was analyzed with the SAMMY code using the following function:

$$Y = AY^{Th} + B. \tag{3.23}$$

In the last equation YTh is the yield calculated by SAMMY using resonances parameters and the RM-formalism.

In this case the standard Γ_γ and Γ_n width from ENDF/B-VII [51] data base were used and fixed in the parameter file.

The term B is included to fit the background, and it was found that it is best fitted by a constant term. The term A is the yield normalization factor, and contains all information related to calibration or yield normalization.

Figure 3.6 shows a SAMMY fit for the 4.9 eV resonance energy.

In this particular case the effect of neutron sensitivity were neglected because of the very small scattering to capture ratio (Γ_n/Γ_γ) of this resonance.

The analysis of the gold sample is very important, because the yield normalization factor obtained for this sample is used as reference for the other isotopes. Once the yield normalization factor for the gold sample is obtained and appropriately corrected by the threshold effect, it can be used as reference for the analysis of the other isotopes and fixed in the SAMMY input file.

Finally the value for the final corrected yield normalization factor is calculated and is given by:

$$Y^{corr} = \frac{f^{t,s,CE}_{sample}}{f^{t,sCE}_{Gold}} \times Y. \tag{3.24}$$

The table 3.5 reports the yield normalization factor calculated for the gold samples investigated in our measurements.

Sample	Setup	NF
Gold (20.03×1) mm	FZK + BICRON	0.586
Gold (20.03×1) mm	BICRON	0.499
Gold (20.03×1) mm	FZK	0.672
Gold (19×0.1) mm	FZK + BICRON	0.614
Gold (19×0.1) mm	BICRON	0.566
Gold (19×0.1) mm	FZK	0.656

Table 3.5: *Normalization factor (NF) obtained for different setups.*

The normalization factor was calculated for different setups. As mentioned before the analysis was made considering the total statistics from the two detectors together, but as we will see in the next chapter we need the normalization factor for both detectors to investigate the neutron sensitivity effect.

The same procedure presented here to analyze this capture data was adopted for the measurement of the neutron capture cross section of ^{54}Fe and ^{57}Fe isotopes. For the last two isotopes the normalization factor was calculated for each spin and parity groups.

Chapter 4

^{54}Fe neutron capture cross section

^{54}Fe and ^{57} Fe are stable isotopes which play an important role in the *s* and *r* processes of nucloeosythesis. The weak *s*-process component exhibits a large uncertainty due to the poorly known cross sections in the Fe-Ni region. This chapter summarizes the analysis and results obtained for the (n,γ) cross section of ^{54}Fe, an *s*-only isotope which is shielded from the *r*-process by ^{54}Cr.

4.1 Experiment

The n_TOF setup used to perform the capture cross section measurement of ^{54}Fe, was described in the chapter 2. In order to reduce the in beam gamma rays induced background and primary γ-rays angular distribution effects, both detectors were moved at 1.8 cm backwards from the sample, and placed at 90° with respect to the beam direction. The relevant information about the capture experiments and the ^{54}Fe sample are summarized in table 4.1.

A	54
Z	26
S_n	13.378 MeV
I^π (target)	0^+
J^π (GS compound nucleus)	$3/2^-$
Abundance	5.845%
Sample mass	2.271 g
Thickness	0.86 mm
Diameter	20.11 mm
Enrichment	99.77 %
Normalization sample	^{197}Au (1×20.03)mm
Number of protons	7.861232×10^{17}

Table 4.1: *Relevant quantities involved in the measurement and analysis of the* ^{54}*Fe* (n,γ)*cross section.*

4.2 Data reduction, WF calculation and correction of systematic effects

The approach to sort and reduce the data was the same as the one described in chapter 3. The uncertainties of the obtained WF are summarized in table 2.4 and the proportionality condition given by equation 2.8 is shown in Fig. 2.17 and 2.18. In the case of the ^{54}Fe isotope a set of 36 monoenergetic gamma rays were Monte Carlo simulated with energies from 50 keV to 14 MeV. By minimizing equation 2.7 we obtain the WF parameters given in table 4.2.

Detector	*Sample*	a_0	a_1 (MeV^{-1})	a_2 (MeV^{-2})	a_3 (MeV^{-3})	a_4 (MeV^{-4})
Bicron	^{54}Fe	0.913	60.0750	20.378	-1.266	0.0581
FZK	^{54}Fe	0.823	44.791	16.700	-1.190	0.042

Table 4.2: *Coefficients of the polynomial WF for* ^{54}*Fe.*

Any capture experiment employing total energy detectors is affected by three different experimental sources of uncertainty related with the electronic threshold of the detectors, the summing probability of two or more gamma rays and the internal conversion electron process.

As described in section 3.8 to obtain the total correction factor, expressed by equation 3.14, a detailed simulation was made using the cascade generator and the best agreement with the experimental pulse-eight spectrum was obtained using the Constant Temperature level density parametrization by Von Egidy et al [31].

The strength functions for E_1, M_1, and E_2 radiation are generated by a giant dipole resonance (GDR) [30], and have the form of a standard Lorentzian, whose parameters are reported in table 4.3.

	E_0(MeV)	Γ_0(MeV)	σ_0(mb)
E1	18.77	7.035	89.25
M1	10.78	4	2
E2	16.57	5.45	1.36

Table 4.3: *Electromagnetic strength parameters used to simulate γ-ray cascades from the decay of $^{55}Fe^*$.*

An example of the MC simulation is represented in Fig. 4.1, where a comparison with the experimental deposited energy is shown.

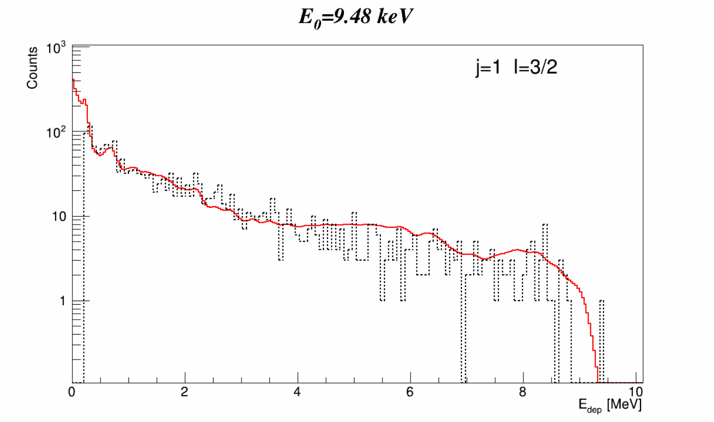

Figure 4.1: *Comparison between the deposited energy histogram predicted by Constant Temperature level density parametrization of Von Egidy et al. and the spectrum measured at n_TOF for the 9.48 keV resonance.*

The threshold correction factor was calculated for an electronic threshold of 250 keV and for all spin and parity values of resonances in $^{54}\mathrm{Fe} + n$. The values obtained are reported in table 4.4.

Detector	J	l	f^{s,t,CE}
BICRON	1/2	0	1.020
BICRON	1/2	1	1.020
BICRON	3/2	1	1.016
BICRON	3/2	2	1.016
FZK	1/2	0	1.018
FZK	1/2	1	1.018
FZK	3/2	1	1.014
FZK	3/2	2	1.014

Table 4.4: *Threshold correction factor for BICRON and FZK detector.*

As reported in table 4.4 the threshold correction factor obtained for the different spin groups of ^{54}Fe show a similar value for the group with J=1/2 and l=0 and 1, and the same situation is present for the group with J=3/2 and l= 1 and 2.

As described in chapter 2, the reference sample used for this measurement was of ^{197}Au, which isotopic an geometrical characteristics were reported in table 2.1. For this sample the threshold correction factor was calculated and is reported in the table 3.2. The final value to apply to the measured yield is given by:

$$Y^{corr} = \frac{f^{t,s,CE}_{^{54}Fe}}{f^{t,sCE}_{Gold}}, \qquad (4.1)$$

In table 4.5, the calculated yield correction factors, using a threshold of 250 keV, are reported.

Detector	l	Y^{corr}
BICRON	0	0.947
BICRON	1	0.943
BICRON	2	0.947
FZK	0	0.948
FZK	1	0.946
FZK	2	0.948

Table 4.5: *Yield correction factor for* ^{54}*Fe.*

The resulting deposited energy spectra for different spin and parity resonances are shown in Fig. 4.2, and the threshold correction factor is computed from these spectra.

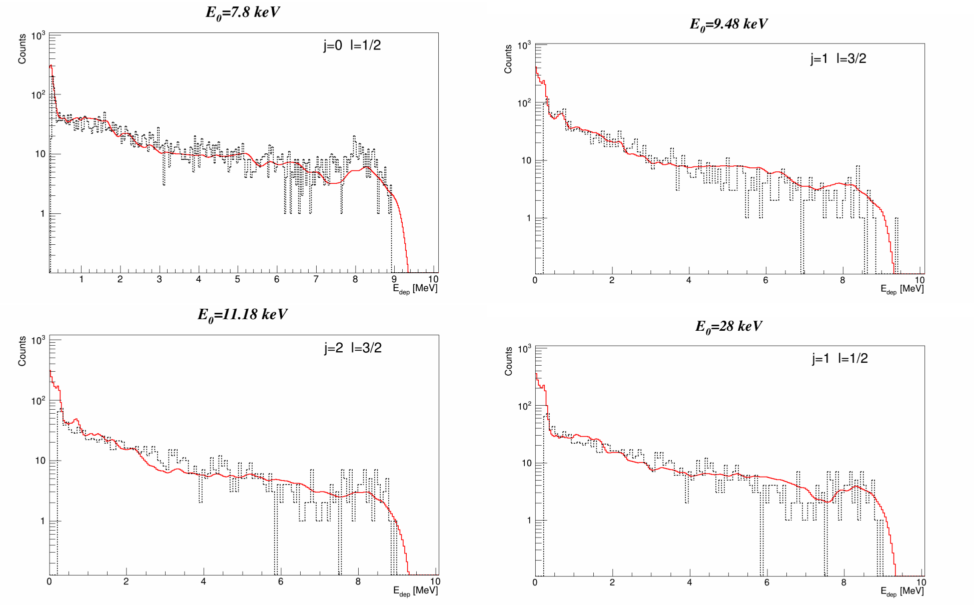

Figure 4.2: *Deposited energy histograms obtained with the statistical model of the nucleus for several resonances of* ^{54}*Fe.*

4.3 Analysis

The experimental yield, as described in the section 3.1, is given by:

$$Y'(E_n) = Y(E_n) \times f^{t,s,CE} \times f^{sat} \times f^{ns}. \tag{4.2}$$

In this equation the therm Y(E$_n$) is the uncorrected experimental yield calculated as:

$$Y(E_n) = \frac{N^w}{N_n E_c} \tag{4.3}$$

where N^w is the weighted counting rate obtained using the calculated WF, E$_c$ is the capture energy and N$_n$ is the number of neutrons. Otherwise the therm f^{sat} is the correction factor obtained by the saturated resonance method from the fit of the 4.9 eV of the gold sample, f^{ns} is the neutron sensitivity correction factor and the $f^{t,s,CE}$ is the correction due to the systematic effects. To perform a resonance analysis of the obtained capture yield, from transmission data, one usually knows E_0, Γ_n, Γ, g for $l = 0$ and $E_0, g\Gamma_n$ for $l \geq 0$. From this information it is possible to determine from the capture data E_0, Γ_γ if g and Γ_n are known and $E_0, g\Gamma_\gamma$ if only $g\Gamma_n$ is known. However, there are some p- and d-wave resonances not observed in transmission measurements. In such cases from the capture data is possible to derive only the resonance area (g$\Gamma_\gamma\Gamma_n/\Gamma$). The experimental yield obtained for the ^{54}Fe capture measurement is represented and compared with the ENDF [51] data library spectra in Fig. 4.3.

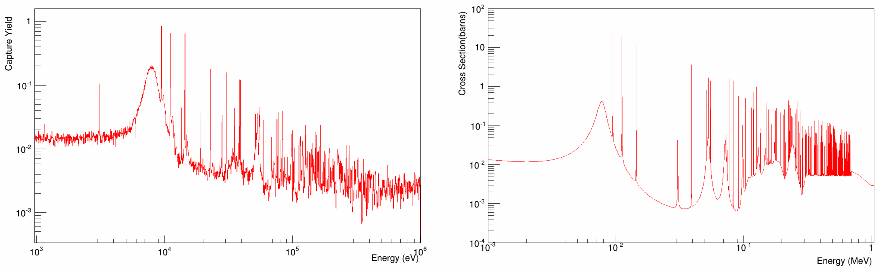

Figure 4.3: *Experimental yield obtained for* ^{54}*Fe isotope (left), and the ENDF capture cross section (right).*

The R-matrix analysis code SAMMY [42] has been employed to fit individually the capture yield of each observed resonance in ^{54}Fe. Double scattering, self shielding and finite size corrections to single scattering were taken into account with this code. The analyzed data can be compared with two previous experiments performed by Brusegan et al. [52, 53] and by Allen et al. [54, 55], which will be briefly described in section 4.4. In our case the background is better treated by fitting it to a constant term rather than subtracting it. For this purpose each capture resonance was analyzed with a wide enough neutron energy window covering its both sides. The fitting function used in SAMMY had the form:

$$Y'{=}Y^f(E_0,\Gamma_\gamma,\Gamma_n)+B, \tag{4.4}$$

where Y' is the corrected experimental yield given by equation 3.2 and B is a constant term to describe the background. The therm Y^f represents the yield fitted by SAMMY, where E_0,Γ_γ,Γ_n are the parameters describing each resonance in the analysis.

For those resonances where one or several transmission measurements give an accurate value of Γ_n, we fixed this parameter to that experimental value and only the energy of the resonance and the gamma width are derived by SAMMY using the Bayes' theorem. In some cases where the resonance is too broad (s-wave resonances) or the statistics are not high enough, the energy of the resonance was also kept fix, and sometimes the value of Γ_n is derived by SAMMY to obtain a best fit for the resonance under study. A total of 168 resonances were identified in the ^{54}Fe (n,γ) in the energy range from 1 eV to 1 MeV. In this energy interval we found 7 new resonances, which were not reported in the previous experiments.

Some examples of the fit obtained with SAMMY are represented in Fig. 4.4 and in Fig. 4.5.

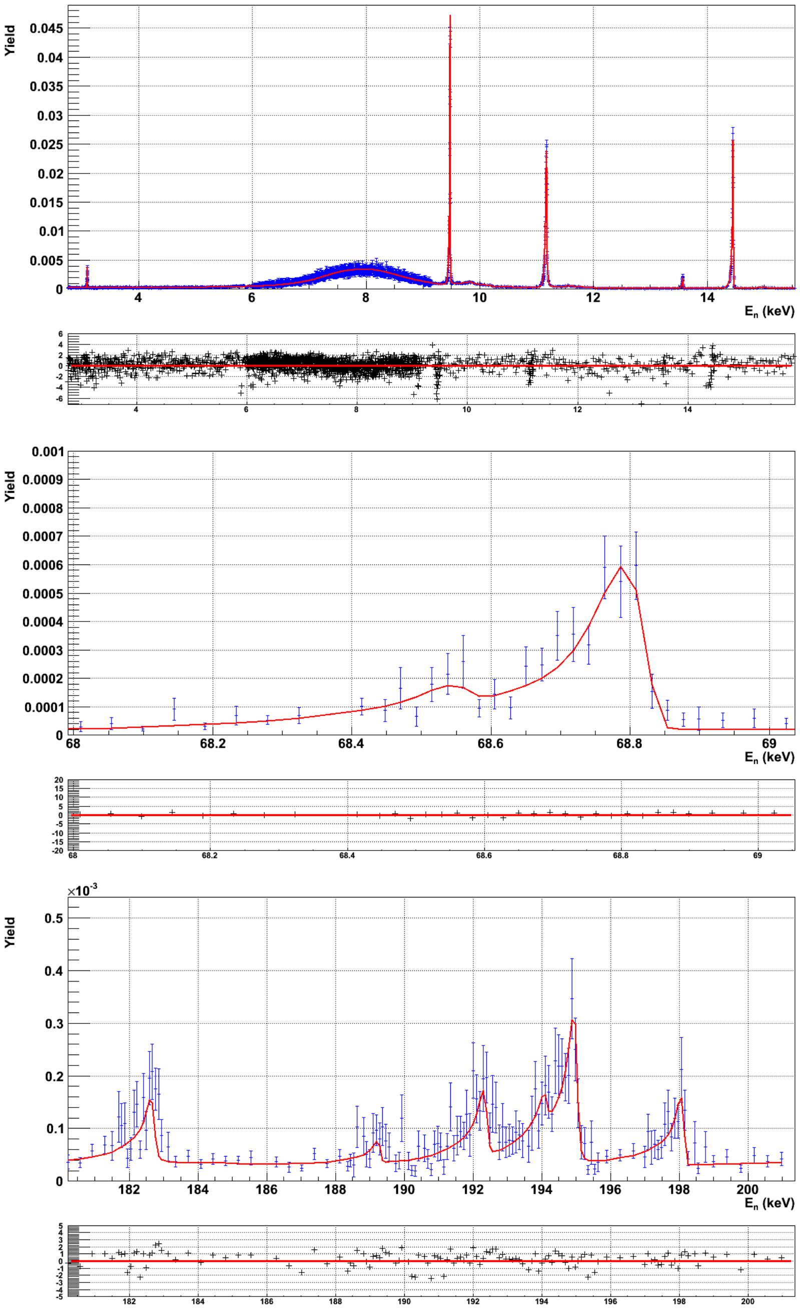

Figure 4.4: *(Top)Energy range from 1 to 15 keV where one can see the first resonance in* ^{54}*Fe + n. (Center) A doublet at an energy of ∼68 keV. (Bottom) At high energy the statistics are more limited, but several resonances can be clearly seen and analyzed.*

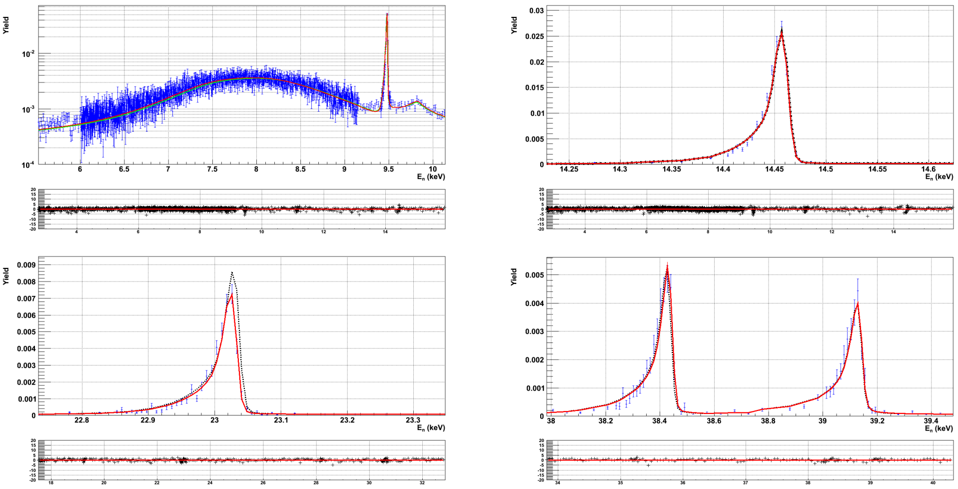

Figure 4.5: *Comparison of some resonances measured at n_TOF versus the capture yield obtained with the resonance parameters reported by [52]. The dashed line stands for the GELINA cross section, whereas the solid curve corresponds to the yield,* $Y^f + B$*, fitted with SAMMY to the n_TOF experimental yield data points, Y'.*

The value obtained for E_0 and Γ_γ and the value used for Γ_n with the relative kernel are summarized in table 4.6.

4.4 Results

This section summarizes the results obtained from the SAMMY analysis. They are compared with the other two experiments performed by Brusegan et al. at GELINA (IRMM) and Allen et al. at Oak Ridge National Laboratory (ORNL). In table 4.6 the radiative kernels obtained in this analysis are reported.

The radiative kernels from the previous experiments and those computed in the Sukhoruchkin compilation are listed in table 4.7. In order to have a clear comparative overview on the obtained capture data, a plot with a comparison between the n_TOF data and the previous experiments is shown in Fig. 4.6.

Before describing our results it may be convenient to make a brief description of the two old experiments.

- Brusegan et al.: This experiment has been performed in 1982 at the GELINA facility using two C_6D_6 liquid scintillator detectors. Results are reported in the range from 0 to 200 keV. The capture data was normalized to the transmission results for the 1.15 keV resonance of ^{56}Fe. The ^{54}Fe sample used had an enrichment of 97.69%, and the analysis was carried out using the area code TACASI [56] and the shape analysis code FANAC [57]. A detailed description of this experiment is available in Ref. [52].

- Allen et al.: This experiment was performed in 1976 at ORNL national laboratory using two non-hydrogenous C_6F_6 scintillator detectors. Two iron samples were measured at a distance of 40 m. A thick and a thin ^{54}Fe samples were used in order to evaluate the self shielding and the multiple scattering and to obtain best results for the low energy range [54, 55].

- ENDF/B -VII.1: (American) Evaluated Nuclear Data Files [51].

- Sukhoruchkin [46]: Compilation of the previous experimental data, which is a combination of the two old experiments and the ENDF data.

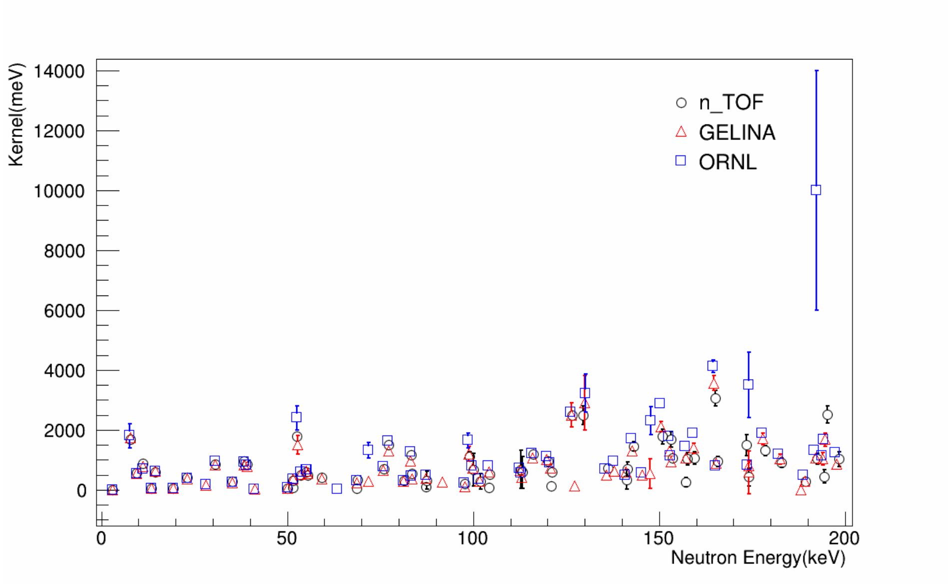

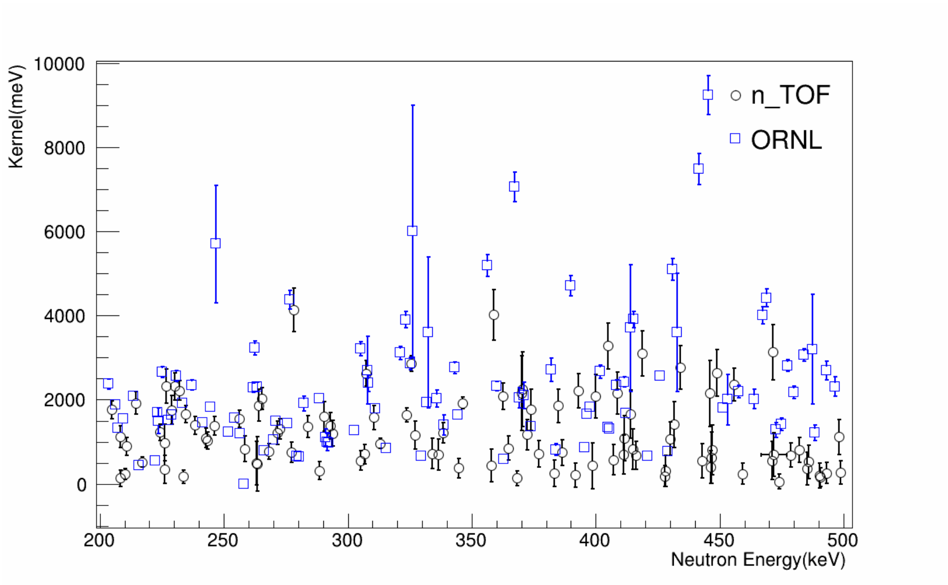

Figure 4.6: *Experimental kernel from n_ TOF, GELINA and ORNL.*

In the n_TOF data, a total of 168 resonances are visible in the energy range up to 500 keV. 102 out of them show a statistical deviation less than 50% with an average RMS of 22%. The statistics of the remaining 66 resonances are low thus yielding an average RMS of 92%. However, these 66 resonances are clearly visible in the data.

In table 4.7 the results obtained in this experiment are reported. Uncertainties quoted in table 4.7 are only statistical.

E_0 *(eV)*	*j*	*l*	Γ_n*(meV)*	Γ_γ*(meV)*	***Kernel(meV)***
3096 (0.2)	1	1/2*	3.48(0.37)	46	3.07(0.34)
7756	0	1/2	1037900	1780 (12)	1685 (12)
9486 (0.1)	1	3/2	578 (123)	592 (74)	554 (145)
11183 (0.2)	2	3/2	6553 (244)	500 (7)	881 (37)
13582	2	3/2*	35	35	33
14468 (0.2)	2	3/2	700	553 (16)	586 (18)
19280	2	5/2*	49	25	47
23042 (0.5)	2	3/2	1659	242 (12)	401 (21)
28229 (1.2)	1	1/2	3760	176 (11)	159 (11)
30678 (0.7)	2	3/2	4999	490 (14)	846 (25)
35273 (0.9)	1	1/2	1601	353 (128)	274 (105)
38463 (1.2)	1	3/2	5001	559 (23)	953 (41)
39162 (1.4)	1	3/2	8500	469 (20)	842 (39)
50101	0	1/2	79	190 (159)	53 (47)
51512 (2)	1	1/2	142	199 (188)	79 (78)
51633 (3.6)	1	1/2	6000	349 (38)	313 (36)
52657	0	1/2	1973400	1878 (155)	1779 (155)
53620	1	3/2	8502	268 (23)	493 (44)
55125 (3.9)	2	3/2	15966	320 (22)	595 (42)
55487 (3.1)	2	3/2	16005	257 (17)	480 (34)
59260 (3.3)	1	3/2	8110	226 (17)	416 (33)
68607 (3.9)	1	1/2	425	46 (21)	40 (19)
68860 (3.4)	1	1/2*	1375	471 (53)	332 (39)
75922 (4.3)	1	3/2	1400	508 (72)	706 (106)
77343 (2.9)	1	3/2	2000	1322 (106)	1509 (128)
81434 (7.6)	1	1/2	10820	335 (44)	308 (43)
83328 (5.1)	1	3/2	12653	638 (48)	1152 (92)

83637 (5)	1	3/2	1610	353 (60)	549 (98)
87289 (7.2)	1	3/2	1333	47 (29)	87 (56)
87505 (1.9)	2	3/2*	1230	192 (175)	315 (303)
97811 (6.8)	1	1/2	310	709 (440)	204 (134)
99064 (53.4)	0	1/2	510394	1184 (156)	1120 (156)
100040 (1.2)	1	3/2	1250	503 (470)	680 (547)
101913 (1.2)	1	1/2	800	464 (399)	278 (253)
104208 (10.1)	1	1/2*	5578 (5831)	80 (51)	75 (97)
104401 (7.9)	1	1/2	6924	572 (77)	501 (71)
112866 (1.3)	1	3/2	890	600 (528)	679 (630)
113205 (3)	1	3/2	1250	405 (357)	580 (539)
116136 (9.7)	1	1/2	26003	1312 (112)	1184 (106)
120106 (12.3)	1	1/2	26002	1052 (147)	959 (141)
120901 (8.6)	2	3/2**	2000	71 (44)	129 (85)
121080 (12.1)	2	3/2	20000	312 (48)	583 (95)
126718 (12)	1	1/2	120890	2671 (135)	2477 (132)
129620 (123)	0	1/2	3461500	2620 (312)	2482 (311)
136162 (20.7)	1	1/2	80035	765 (80)	718 (79)
141203 (5.2)	1	1/2	870	607 (552)	339 (325)
141403 (8.7)	1	1/2	1871	1202 (374)	694 (228)
143191 (10.8)	2	3/2	12002	821 (84)	1458 (157)
150804 (11.3)	1	1/2	8001	2449 (330)	1778 (252)
153125 (14.5)	1	3/2	19806	927 (135)	1678 (258)
153680 (14.9)	1	3/2	30008	571 (73)	1062 (143)
157161 (14.2)	1	3/2	10778	134 (80)	250 (158)
157611 (19.8)	1	1/2	25128	1135 (217)	1029 (208)
159481 (36.5)	1	1/2	100150	1131 (207)	1060 (205)
165100 (19.8)	1	3/2	111550	1640 (129)	3065 (255)
165721 (23.9)	1	1/2	75070	1007 (170)	942 (167)
173480 (189.3)	0	1/2	4585900	1575 (357)	1493 (357)
174042 (81.8)	1	1/2	174990	453 (303)	428 (302)
178403 (13.4)	1	1/2	13976	1533 (187)	1310 (168)
182867 (27.1)	2	5/2*	50057	323 (53)	911 (158)
189451 (10.7)	1	1/2*	2107	345 (137)	281 (118)
192548 (22.3)	2	3/2*	32439	549 (91)	1023 (179)
194302 (10.8)	1	3/2*	2000	268 (124)	448 (219)

195184 (19.3)	1	3/2	49994	1363 (142)	2515 (276)
198304 (10.9)	1	3/2*	2920	665 (153)	1027 (250)
204704 (23.3)	1	3/2	40001	951 (109)	1762 (213)
208151 (13.6)	1	1/2	6698	148 (194)	137 (190)
208315 (18.5)	1	1/2	20002	1262 (277)	1126 (260)
209997 (22.4)	2	3/2	24738	122 (67)	231 (134)
210857 (15.9)	2	3/2	24723	480 (109)	893 (213)
214461 (44.9)	1	1/2	166350	2050 (270)	1919 (267)
216904 (17.6)	1	3/2	15000	279 (65)	519 (128)
224210 (18.3)	1	3/2	20002	669 (98)	1228 (190)
226169 (49.8)	1	1/2	436200	1038 (436)	981 (435)
226230 (7.3)	1	1/2	41800	358 (334)	337 (332)
226606 (14.6)	2	3/2	11401	1376 (230)	2327 (410)
228893 (12.3)	2	3/2	3677	1237 (230)	1755 (344)
230200 (12.4)	2	3/2	5196	1595 (208)	2314 (318)
232096 (39)	1	3/2	132980	1182 (119)	2221 (236)
233801 (18.9)	2	3/2	16117	91 (81)	171 (160)
234453 (17.5)	1	3/2	25903	904 (107)	1657 (207)
238350 (13.7)	1	1/2	9200	1743 (257)	1389 (216)
242748 (19.1)	1	1/2	17601	1230 (243)	1090 (227)
246117 (60.6)	1	3/2	246900	734 (112)	1387 (224)
253496 (21.6)	1	1/2	27249	558 (103)	1037 (202)
256103 (31.4)	2	3/2	75432	821 (102)	1540 (202)
258360 (146.4)	0	1/2	351160	879 (300)	832 (299)
263200 (12.6)	2	1/2	1812	304 (303)	494 (519)
263403 (39.5)	2	1/2	56002	252 (324)	476 (644)
263610 (26.6)	1	3/2	32602	951 (335)	1752 (652)
264114 (22.7)	1	1/2	25702	2133 (404)	1867 (374)
265206 (17.8)	2	1/2	17501	1142 (137)	2033 (257)
268099 (14.5)	1	1/2	5000	962 (219)	765 (184)
271695 (15.3)	1	1/2	7560	1535 (339)	1210 (282)
272589 (15.4)	2	1/2	8300	751 (133)	1305 (244)
277228 (122.3)	1	3/2	300190	790 (239)	747 (239)
278351 (36)	2	1/2	120310	2222 (262)	4136 (515)
283952 (21.5)	1	3/2	20517	741 (135)	1357 (260)
288407 (45.3)	1	1/2	65461	334 (209)	315 (208)

290526 (44.5)	1	3/2	81017	852 (176)	1599 (348)
292863 (22.1)	0	1/2	110000	1475 (325)	1380 (320)
293806 (22.1)	1	1/2	21701	1348 (325)	1203 (306)
305115 (21.6)	1	1/2	18000	607 (246)	557 (238)
306601 (20.2)	2	3/2	14926	384 (234)	711 (234)
307234 (69.1)	2	3/2	148030	1398 (307)	2626 (307)
310385 (25.9)	1	1/2	29614	1761 (298)	1576 (281)
313133 (31.6)	1	3/2	37701	514 (54)	961 (121)
323566 (72)	1	3/2	138770	868 (164)	1635 (163)
325691 (37.2)	2	3/2	63714	1549 (185)	2866 (185)
327197 (17.9)	1	1/2	9192	1413 (331)	1161 (329)
334049 (26.9)	1	1/2	29100	777 (360)	718 (358)
336531 (1244.6)	0	1/2	3368100	739 (371)	700 (371)
338458 (31.7)	1	1/2	40001	1327 (238)	1218 (238)
344851 (16.2)	1	1/2	6213	420 (228)	373 (228)
346365 (55.9)	1	3/2	116820	1024 (146)	1924 (145)
357817 (80.8)	1	3/2	136300	234 (194)	444 (387)
358820 (24.6)	1	1/2	27302	5016 (707)	4017 (597)
362728 (39)	1	1/2	57306	2290 (330)	2088 (318)
364893 (161.3)	0	1/2	368340	901 (281)	852 (280)
368382 (28.1)	1	1/2	29102	142 (182)	134 (181)
370205 (112)	2	3/2	236900	1140 (447)	2151 (891)
370504 (68.7)	1	1/2	128410	2417 (897)	2249 (881)
372199 (61)	1	1/2	103200	1249 (369)	1170 (365)
373892 (960.8)	0	1/2	4295600	1857 (496)	1760 (496)
376873 (36.7)	1	1/2	45602	767 (324)	715 (319)
383246 (135)	2	3/2	243970	132 (157)	250 (314)
384853 (48)	1	1/2	78003	2007 (402)	1855 (392)
386503 (19.1)	2	3/2	10549	409 (159)	746 (305)
391761 (22.5)	2	3/2	17000	111 (147)	208 (293)
392906 (31.1)	2	3/2	37342	1204 (213)	2211 (412)
398803 (41.6)	1	3/2	53700	230 (275)	433 (548)
399989 (24.8)	2	3/2	22179	1155 (275)	2081 (523)
404791 (78.6)	2	3/2	176130	1746 (277)	3278 (548)
407201 (21.8)	1	3/2	15173	309 (185)	574 (362)
408711 (34.3)	1	1/2	42088	2410 (532)	2161 (504)

411101 (29.4)	2	3/2	30399	371 (234)	695 (463)
411623 (62.4)	0	1/2	101070	1158 (544)	1085 (538)
413926 (59.6)	1	3/2	96856	881 (286)	1655 (566)
414872 (22.1)	2	3/2	15663	449 (251)	827 (487)
416303 (50)	1	1/2	71677	718 (339)	674 (336)
418715 (122.9)	2	3/2	423710	1644 (267)	3105 (533)
427701 (31.3)	1	1/2	33444	195 (247)	184 (246)
427990 (38.1)	2	3/2	47083	163 (186)	308 (371)
430160 (25.1)	1	1/2	21204	1191 (423)	1069 (400)
431457 (1479.4)	0	1/2	3845100	1486 (545)	1408 (544)
434199 (93)	2	3/2	191810	1470 (257)	2766 (509)
442810 (86.1)	2	3/2	143550	290 (207)	548 (414)
443524 (96.2)	1	1/2	163310	284 (297)	269 (297)
446024 (149.7)	2	3/2	296680	1138 (394)	2149 (785)
446455 (57.1)	1	1/2	84640	423 (395)	399 (393)
446567 (44)	2	3/2	58431	330 (303)	623 (603)
446975 (46.6)	1	3/2	63871	428 (299)	805 (594)
448990 (23.8)	1	3/2	19999	1498 (297)	2643 (553)
455697 (215)	0	1/2	679450	2499 (390)	2360 (388)
459240 (22.1)	2	3/2	13944	128 (127)	241 (252)
471171 (42.1)	1	1/2	53828	589 (457)	552 (452)
471388 (76.3)	1	3/2	140490	1672 (334)	3133 (659)
471893 (5047.1)	0	1/2	22013000	730 (519)	692 (519)
473863 (318.1)	0	1/2	610130	28 (86)	54 (171)
478695 (55)	1	3/2	81114	363 (147)	684 (293)
482081 (21.7)	2	3/2	12439	438 (154)	801 (298)
485256 (95.3)	0	1/2	456250	389 (392)	368 (392)
485773 (43)	2	3/2	55177	278 (202)	524 (401)
490134 (224.5)	1	3/2	421220	103 (151)	195 (302)
490600 (20.6)	1	1/2	10080	165 (226)	154 (223)
493002 (87.6)	1	1/2	144240	273 (255)	258 (254)
498054 (104.3)	1	3/2	185420	592 (209)	1119 (416)
498813 (150)	1	1/2	271730	283 (275)	268 (274)

Table 4.6: *Value of the kernel obtained from n_ TOF data.*

In table 4.8 a comparison between n_TOF data end the previous works are reported.

E_0 (eV)	***n_ TOF (meV)***	***GELINA (meV)***	***ORNL (meV)***
3096	3.07 (0.34)	3 (0.3)	3 (0.15)
7756	1685 (12)	1740 (110)	1800 (400)
9486	554 (145)	550 (30)	550 (28)
11183	881 (37)	770 (40)	690 (34)
13582	33	35 (3)	34 (2)
14468	586 (18)	620 (20)	620 (31)
19280	47	50 (4)	47 (2)
23042	401 (21)	370 (20)	390 (20)
28229	159 (11)	160 (10)	170 (8)
30678	846 (25)	830 (30)	960 (48)
35273	274 (105)	230 (20)	260 (13)
38463	953 (41)	830 (30)	920 (46)
39162	842 (39)	770 (40)	820 (41)
50101	53 (47)	56 (70)	75 (4)
51633	313 (36)	360 (30)	360 (18)
52657	1779 (155)	1500 (300)	2400 (400)
53620	493 (44)	520 (40)	600 (30)
55125	595 (42)	620 (50)	680 (34)
55487	480 (34)	550 (50)	680 (34)
59260	416 (33)	370 (30)	0
68860	332 (39)	240 (30)	310 (16)
75922	706 (106)	650 (30)	760 (38)
77343	1509 (128)	1290 (60)	1620 (81)
81434	308 (43)	290 (30)	300 (30)
83328	1152 (92)	960 (70)	1270 (64)
83637	549 (98)	360 (50)	450 (30)
87505	315 (303)	390 (40)	500 (25)
97811	204 (134)	110 (20)	240 (30)
99064	1120 (156)	1200 (250)	1650 (250)
100040	680 (547)	730 (60)	790 (40)
101913	278 (253)	290 (30)	350 (20)
104401	501 (71)	600 (60)	790 (40)

112866	679 (630)	640 (70)	720 (36)
113205	580 (539)	420 (60)	560 (28)
116136	1184 (106)	1060 (70)	1210 (60)
120106	959 (141)	1010 (90)	1110 (56)
121080	583 (95)	720 (110)	890 (44)
126718	2477 (132)	2500 (400)	2590 (130)
129620	2482 (311)	2900 (900)	3220 (640)
136162	718 (79)	500 (50)	690 (34)
141403	694 (228)	590 (70)	480 (24)
143191	1458 (157)	1300 (120)	1720 (86)
150804	1778 (252)	2100 (170)	2880 (144)
153125	1678 (258)	1280 (150)	1780 (89)
153680	1062 (143)	920 (110)	1140 (57)
157611	1029 (208)	1060 (100)	1450 (72)
159481	1060 (205)	1390 (170)	1890 (94)
165100	3065 (255)	3560 (250)	4120 (206)
165721	942 (167)	870 (140)	810 (40)
173480	1493 (357)	580 (720)	3500 (1100)
174042	428 (302)	790 (160)	820 (41)
178403	1310 (168)	1700 (200)	1880 (94)
182867	911 (158)	1020 (160)	1200 (60)
189451	281 (118)	270 (90)	490 (30)
192548	1023 (179)	1070 (140)	1330 (66)
194302	448 (219)	1030 (200)	1140 (57)
195184	2515 (276)	1670 (210)	1690 (84)
198304	1027 (250)	850 (130)	1230 (62)

Table 4.7: *n_ TOF kernel compared with other works.*

Figure 4.7 and 4.8 shows the ratio between n_TOF and GELINA data, and between n_TOF and ORNL data respectively. Compared with the previous experiment at GELINA the n_TOF kernels are in average 0.7% higher in the energy range from 1 eV to 200 keV. In average, considering the average statistical uncertainty of about 20%, n_TOF kernels are in good agreement with Brusegan's data measured at GELINA. The average deviation (weighted by error bars) is of (0.76±1.6)% as shown in Fig. 4.7.

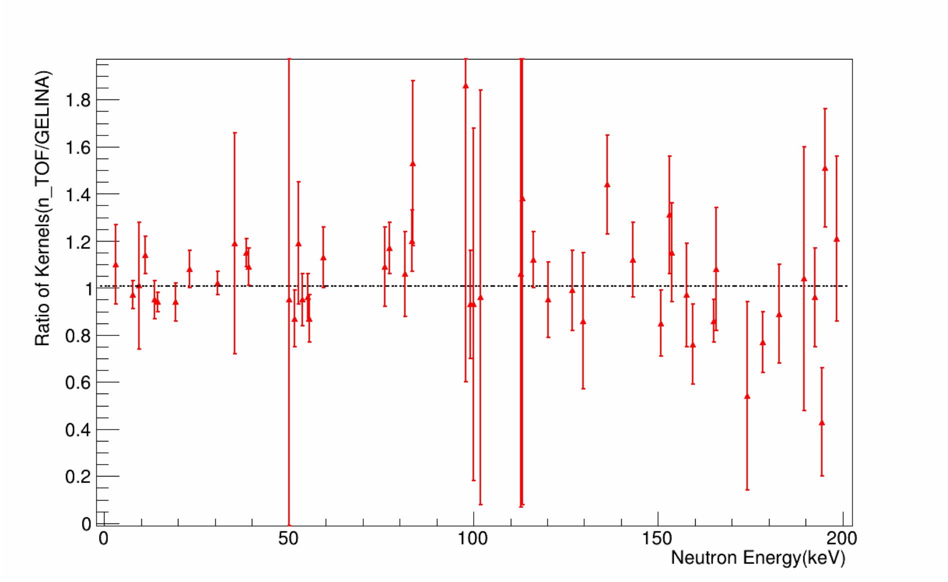

Figure 4.7: *Ratio of kernel between n_ TOF data and GELINA data.*

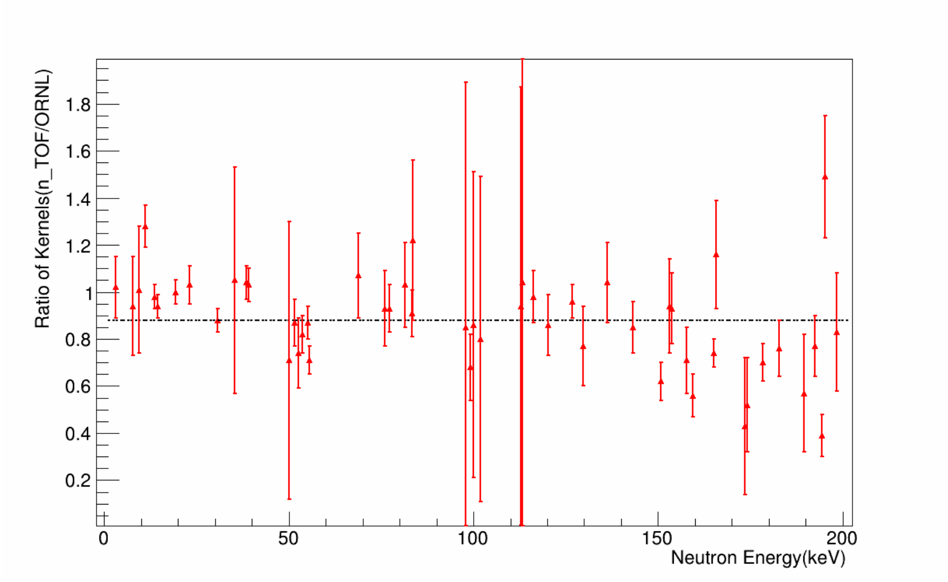

Figure 4.8: *Ratio of kernel between n_ TOF data and ORNL data.*

Compared with the ORNL experiment the RMS deviation the n_TOF data are in average 12.3% lower in the energy range up to

200 keV (Fig.4.8). A comparison up to 500 keV was not possible due to the high density of resonances.

- Range from 1 to 15 keV

In this range a set of 6 resonances were analyzed and are present in previous experiments, as well in the Sukhoruchkin compilation.

The s-wave resonance at 7.7 keV was analyzed using only the FZK data, in order to avoid possible neutron sensitivity contribution from the BICRON detector and because its statistics were large enough. For the resonance at 13.5 keV the Γ_n was taken from the Sukhoruchkin compilation. For the other resonances the Γ_n values were taken from GELINA report Ref. [52]. Only the fit of the 9.48 keV was clearly better when both Γ_n and Γ_γ were allowed to vary in R-Matrix analysis.

The 3 keV and 13.5 keV resonances are not present in the ENDF evaluation.

- Range from 19 to 30 keV

4 resonances are present in this energy range, both in the n_TOF data and in the two previous experiments. However, only the 30 keV resonance is tabulated. The SAMMY R-Matrix fit was made, in general, fixing the value of Γ_n for all of them. There is good agreement between n_TOF, GELINA and ORNL. Only the resonance at 30 keV shows a kernel 12% lower than in the ORNL data.

- Range from 35 to 45 keV

3 resonances are present in this energy range. Only the 39 keV resonance is present in the ENDF evaluation, reported as l=1, but the best fit for the n_TOF yield was obtained with l=2. A resonance at 41 keV is tabulated in the GELINA and ORNL capture data and not observed in the TOF data. The fit was made fixing Γ_n to the GELINA transmission data (Ref. [52]). The kernel obtained for the 35 keV resonance is 4.5% lower than the GELINA kernel and 15% lower than the ORNL kernel. The kernel at 38 keV is 15% higher than the GELINA kernel and 3.5% higher than the ORNL one. The kernel at 39 keV is 9% higher then the GELINA kernel and 2.7% higher than the ORNL one.

- Range from 50 to 60 keV

8 resonances are visibles and analyzed in this range. In the ENDF evaluation the resonances at 51.52 keV, 52.87 keV (s-wave), 53.54 keV and 55.35 keV are tabulated. In the GELINA and ORNL publication a total of 7 resonances are tabulated.

The best fit was obtained fixing Γ_n using the transmission parameters given by the Sukhoruchkin compilation [47]. A new resonance is clearly visible at 51.5 keV in the n_TOF data and the fit was obtained varying Γ_γ and Γ_n.

- 60-70 keV

In this range a doublet at 68.61 and 68.86 keV is visible, but only the second resonance is reported in previous experiments. Nothing appears in ENDFat this energy.

The n_TOF kernel is 38% higher than the GELINA kernel and 7% higher than the ORNL data.

- Range 70-80 keV

Two of the three resonances reported in previous experiments are visible in the n_TOF data. The two resonances present in the n_TOF data are also tabulated in ENDF. The s-wave at 77 keV is analyzed using only the FZK data for the same reason described before. The p-wave at 75 keV is 8.5% higher than the GELINA data and 9% lower than the ORNL data.

- Range 80-100 keV

7 resonances are present in this range. All of them are tabulated in the previous experiments, but the doublet at 87 keV is reported as a single resonance in the previous experiments.

- Range 100-200 keV

A set of 33 resonances were analyzed in this energy range. A new resonance was analyzed at 157.1 keV, and the doublet at 104.2 keV is reported as a single resonance in the previous experiments.

- 200-500 keV

In all this energy range 100 resonances were analyzed. Allen at al. report 95 resonances in the same energy range.

4.5 Neutron Sensitivity

Discrepancies with respect to previous experiments at GELINA and ORNL cannot be ascribed to effects related to the neutron sensitivity. Indeed, this is demostrated in Fig. 4.9 where the ratio of the kernels versus Γ_n/Γ_γ is displayed.

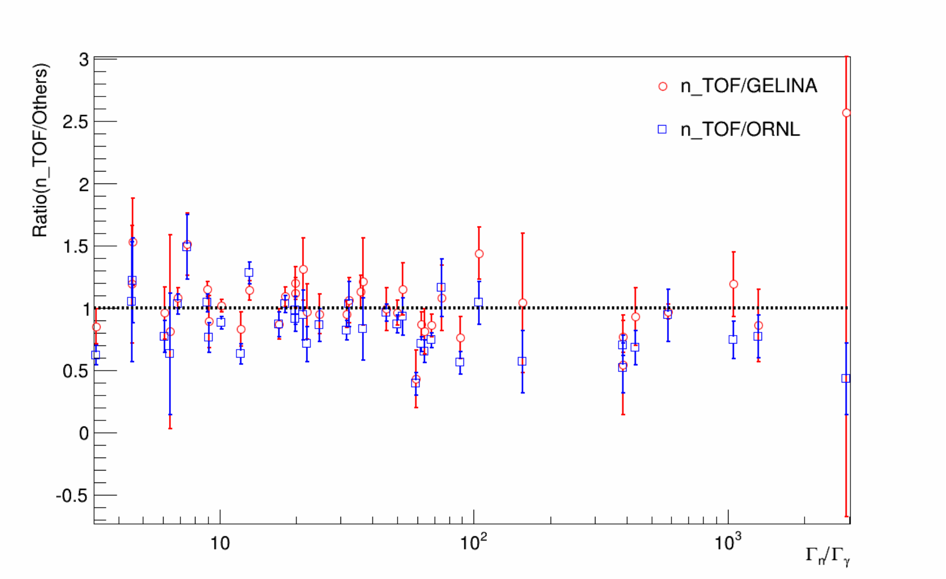

Figure 4.9: *Ratio of the kernels between n_TOF and the previous experiments versus* Γ_n/Γ_γ.

4.6 Thermal Cross Section

From the n_TOF parameters is possible to calculate the thermal neutron cross section which can be extrapolated as the sum of the contribution from the tails of all the individual Bret-Wigner resonances. Near $E_n = 0$ the radiative capture cross section is:

$$\sigma_\gamma = \sum_{i=1}^{N} g_n^i \frac{\pi}{k_n^2} \frac{\Gamma_n^i \Gamma_\gamma^i}{(E_n - E_0^i)^2 + (\Gamma/2)^2}, \tag{4.5}$$

where N is the total number of *s*- and *p*- resonances.

At thermal energy, assuming $E_0^i \gg E_n = 0.025$ eV and $E_0^i \gg \Gamma/2$, the previous equation can be written as:

$$\sigma_\gamma \approx 4.099 \times 10^6 \left(\frac{A+1}{A}\right) \sum_{i=1}^{N} g_n^i \frac{\Gamma_n^i \Gamma_\gamma^i}{(E_0^i)^2}. \tag{4.6}$$

If the cross section is dominated by the contribution due to s-wave resonances, the previous equation can be rewritten as

$$\sigma_\gamma \approx 4.099 \times 10^6 \left(\frac{A+1}{A}\right) \sum_{i=1}^{N_0} g_n^i \frac{\Gamma_n^i \Gamma_\gamma^i}{(E_0^i)^2}, \tag{4.7}$$

where N_0 is the amount of the s resonances. The results obtained for σ_γ for n_TOF, GELINA and ORNL are reported in table 4.8. The result obtained from the n_TOF resonance parameters is in reasonable agreement with the value derived from the parameters reported by Brusegan et al. from GELINA and Allen et al. from ORNL. All values lie around 37% lower than the thermal cross section for this isotope, which has been accurately measured [58] and its value is of 2252 mb. This difference can be ascribed to direct neutron capture.

Parameters	σ(mb)
n_TOF	1282 (8.9)
GELINA	1264
ORNL	1349
Mughabghab et al.	2252

Table 4.8: *Thermal neutron capture cross sections calculated using equation (4.7) for the resonance parameters of n_TOF, GELINA and ORNL. At the bottom the experimental value of the thermal CS is given.*

4.7 Maxwellian Averaged Cross Section (MACS)

Stellar reaction rates are a prerequisite for the study of nucleosynthesis at different stages of stellar evolution. The s-process nucleosynthesis takes place over a range of thermal energies from kT = 5 to 100 keV. The stellar neutron capture rate is given by,

$$\langle \sigma v \rangle = \int_{\infty}^{0} \sigma v \Phi(v) dv \tag{4.8}$$

where the velocity distribution $\Phi(v)$ corresponds to the Maxwell-Boltzman distribution.

Alternatively, the maxwellian-averaged stellar (n,γ) cross section, can be calculated using an approximation formula derived by Macklin & Gibbons [59] and is given by:

$$\langle \sigma v \rangle / v_T(kT) = \sigma_{th} \sqrt{\frac{(25.3 \times 10^6)}{kT}} + \frac{2}{\sqrt{\pi}} \times \frac{1}{(kT)^2} \sum_i A_{\gamma i} E_{0i} exp\left(-\frac{E_{0i}}{kT}\right), \tag{4.9}$$

where the term $A_{\gamma i}$ is the capture area, σ_{th} is the thermal cross section of ^{54}Fe, and kT is the stellar temperature.

At lower stellar temperatures kT the MACS is dominated by broad s-wave resonances. From the previous formula the MACS for the ^{54}Fe isotope has been calculated. Table 4.9 reports the total MACS at 30 keV obtained from the n_TOF data compared with the GELINA and ORNL data. Otherwise the n_TOF MACS are in agreement with the total MACS at 30 keV reported in KADONIS [60].

Parameters	MACS at 30 keV(mb)
n_TOF	30.8 ± 1.6
GELINA	27.6 ± 1.8
ORNL	33.6 ± 2.7
KADONIS	29.7 ± 1.3

Table 4.9: *MACS at 30 keV for the resonance parameters of n_TOF, GELINA and ORNL. At the bottom the value reported in KADONIS is given.*

4.8 Conclusion

For ^{54}Fe a total of 168 resonances were analyzed in the range from 1 eV up to 500 keV. Our data were compared versus two other experiments performed at ORNL by Allen et al. in 1976 and at GELINA by Brusegan et al. in 1982. At the same time the n_TOF data are compared versus the ENDF data library and the overall Sukhoruchkin compilation. Our data show an average deviation respect to the GELINA data of 0.76% and are 17% lower than the ORNL data. The thermal cross section obtained from our data is in reasonable agreement with the thermal cross section calculated for the previous experiments taking into account only the contribution of the first s-wave resonance. Otherwise the MACS calculated at 30 keV are in reasonable agreement with the value reported from KADONIS. It is important to remark that the analysis for the s-wave was performed using only the FZK data, in order to avoid possible neutron sensitivity effect from the BICRON detector.

Chapter 5

^{57}Fe neutron capture cross section

5.1 Experiment, data reduction, WF calculation and correction of systematics effects

The n_TOF setup used to measure the capture cross section of ^{57}Fe is the same as the one used for ^{54}Fe. The approach to sort the data, as well as to obtain the WF and to estimate the experimental errors was the same too. Some relevant information about this capture experiment and about the ^{57}Fe isotope is summarized in table 5.1.

A	57
Z	26
S_n	7.646 MeV
I^π (target)	$1/2^-$
J^π (GS compounds)	0^+
Natural Abundance	2.119 %
Sample mass	1.6235 g
Thickness	0.64 mm
Diameter	19.95 mm
Enrichment	99.06 %
Normalization sample	^{197}Au (0.1×19.94)mm
Number of protons	9.592581×10^{17}

Table 5.1: *Relevant quantities involved in the measurement and analysis of the ^{57}Fe(n,γ) cross section.*

The WF was obtained simulating monoenergetic gamma rays from 50 keV up to the neutron separation energy S_n, and the obtained WF parameters are summarized in tab. 5.2.

Detector	*Sample*	a_0	a_1 (MeV^{-1})	a_2 (MeV^{-2})	a_3 (MeV^{-3})	a_4 (MeV^{-4})
Bicron	^{57}Fe	1.036	65.061	23.303	-1.467	0.0635
FZK	^{57}Fe	0.687	39.358	14.120	-0.914	0.0355

Table 5.2: *Coefficients of the polynomial WF for ^{57}Fe.*

To obtain the total correction factor a detailed simulation was made using the cascade generator and the best agreement, as for ^{54}Fe, is obtained using the Constant Temperature level density parametrization by Von Egidy et al. [31], and the strength functions for E_1, M_1, and E_2 radiation are generated by a giant dipole resonance (GDR), and have the form of a standard Lorentzian. The electromagnetic parameters used in the calculation are reported in table 5.2.

	E_0(MeV)	Γ_0(MeV)	σ_0(mb)
E1	18.53	6.864	95.7
M1	10.59	4	2
E2	16.27	5.414	1.272

Table 5.3: *Electromagnetic strength parameters for* $^{57}Fe + n$.

An example for the parametrization used in the MC simulation is represented in Fig. 5.1, where a comparison with the experimental deposited energy (dashed line) is shown.

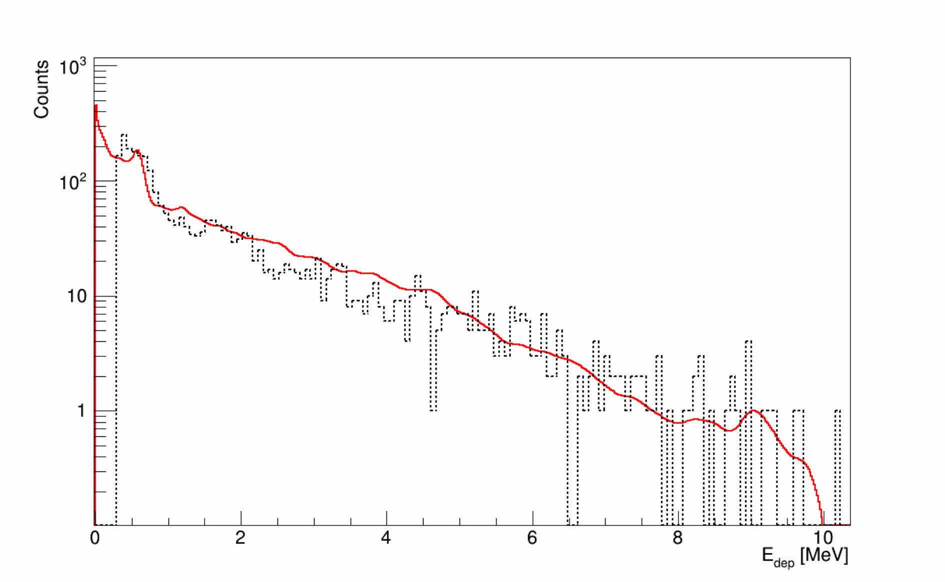

Figure 5.1: *Comparison between the deposited energy histogram obtained with the Constant Temperature level density parametrization of Von Egidy et al. versus the spectrum measured at n_ TOF for the 6.2 keV resonance.*

The threshold correction factor was calculated for an electronic threshold of 250 keV for the BICRON detector and 300 keV for the FZK detector and for all spin groups of ^{57}Fe. The final correction factor to apply to the experimental yield is given by:

$$Y^{corr} = \frac{f^{t,s,CE}_{^{57}Fe}}{f^{t,sCE}_{Gold}}, \tag{5.1}$$

The values obtained for the threshold correction factor and the final Yield correction factor are reported in table 5.4 and in table 5.5. The correction factor for the gold samples were reported in chapter 2 (see table 2.2).

Detector	J	l	$f^{s,t,CE}$
BICRON	0	0	1.01163
BICRON	1	0	1.01512
BICRON	2	1	1.02094
FZK	0	0	1.01104
FZK	1	0	1.01296
FZK	2	1	1.01834

Table 5.4: *Threshold correction factor for BICRON and FZK detector.*

Detector	J	l	Y^{corr}
BICRON	0	0	0.934
BICRON	1	0	0.937
BICRON	2	1	0.942
FZK	0	0	0.939
FZK	1	0	0.94
FZK	2	1	0.946

Table 5.5: *Yield correction factor for ^{57}Fe.*

The resulting deposited energy spectra for different spin and parity resonances are shown in Fig. 5.2, and the threshold correction factors listed above are computed from these spectra.

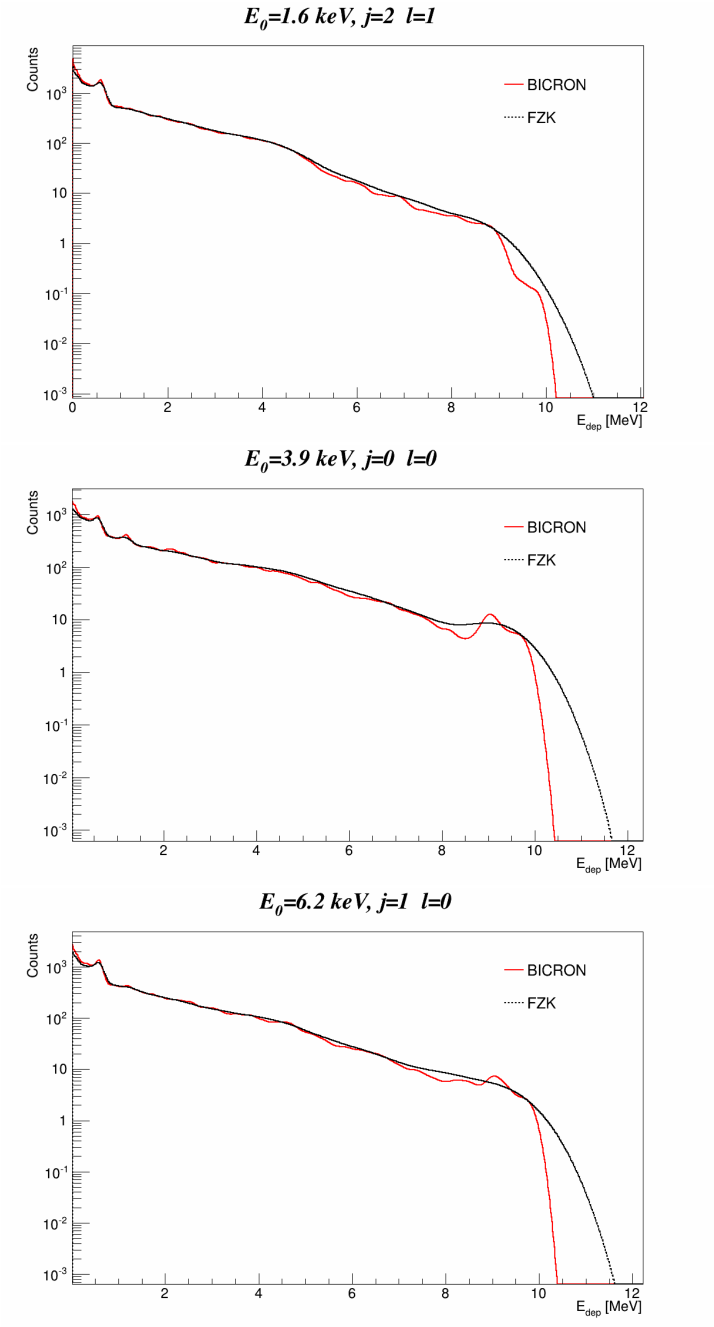

Figure 5.2: *Deposited energy histograms obtained for BICRON and FZK(dashed line) detector with the statistical model of the nucleus for several resonances of* ^{57}Fe*.*

5.2 Analysis

The procedure to obtain the experimental yield is the same as the one followed for the analysis of ^{54}Fe. The R-matrix analysis code SAMMY has been employed to fit individually the capture yield of each observed resonance in ^{57}Fe.

The experimental yield obtained for the ^{57}Fe capture measurement is represented and compared with the ENDF data library in Fig. 5.3.

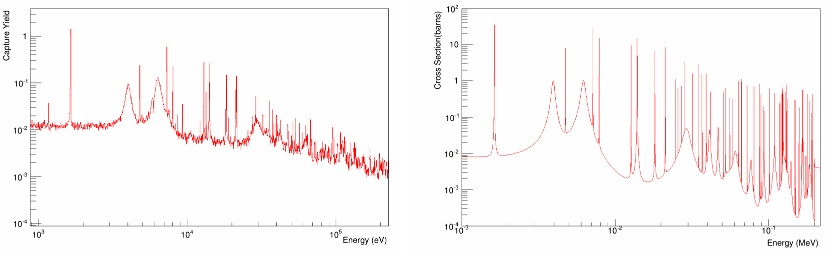

Figure 5.3: *Experimental yield obtained for ^{57}Fe isotope (left), and the ENDF capture cross section (right).*

The results of the analysis is compared with two previous experiments performed by Rohr et al.(GELINA 1983) [61] and Allen at al. (ORNL 1977) [62] (section 5.3). A total number of 116 resonances were identified in ^{57}Fe (n,γ) in the energy range from 1 eV to 200 keV, the region of the RRR. In this interval a set of 7 resonances not tabulated in the previous experiments could be analyzed in the n_TOF data and are well defined. Some examples of the fits obtained with SAMMY are displayed in Fig. 5.4

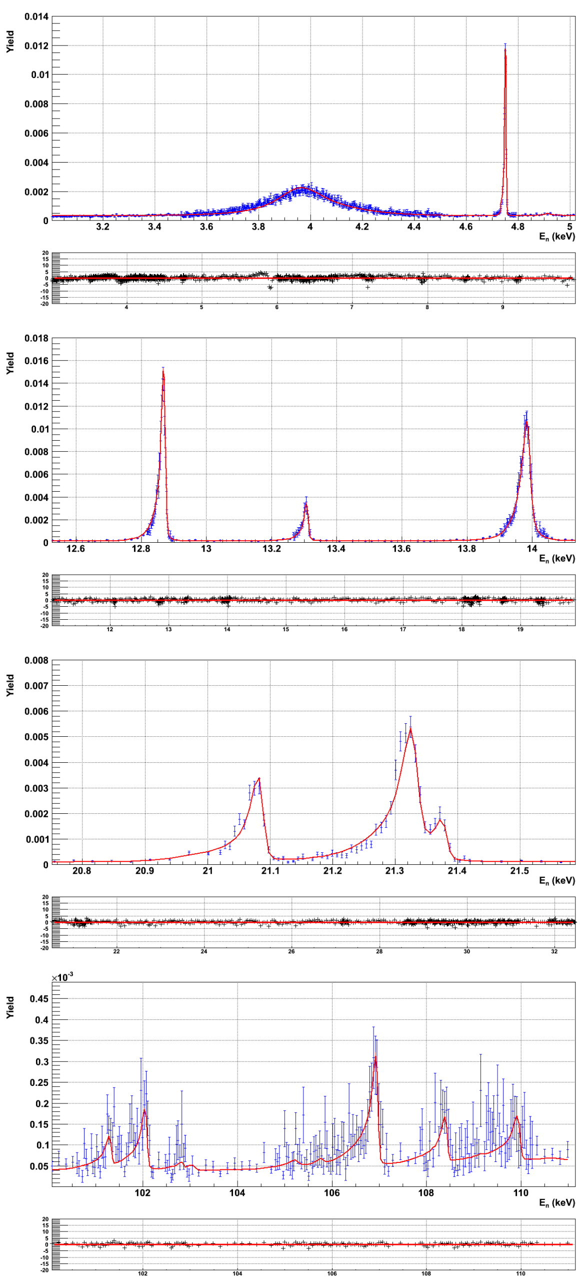

Figure 5.4: *First s-wave at 3.9 keV and some p-wave resonances. The solid curve corresponds to the yield, $Y^f + B$, fitted with SAMMY to the n_ TOF experimental yield data points, Y'.*

5.3 Results

The aim of this section is to report final analysis results and at the same time compare them with the other two main experiments, which were performed by Rohr et al. [61] and Allen et al. [62] in the past. In addition, our results will be compared also versus one calculated data library and one compilation of previous experimental data.

- Rohr et al.: This experiment was performed in 1983 at the 150 MeV LINAC of GELINA. The method employed to perform the experiment was a TOF with 60 m path length. The samples used for the capture cross section were two ^{57}Fe oxide samples of 80 mm diameter with enrichments of 93.4 and 94%. These samples were canned in 0.3 mm Al and placed back to back in the neutron beam. Two cylindrical liquid scintillator detectors containing benzene were used in conjunction with a 3 mm Boron-10 carbide slab used as a flux monitor. The data were analyzed using the capture area fitting code TACASI and the R-Matrix fitting program FANAC. The uncertainties include statistical and systematic errors due to the background, neutron sensitivity, relative flux and discrepancies due to the two analysis codes. The analysis was performed in the energy range from 1 keV up to 200 keV and a total of 117 resonances were analyzed [61].

- Allen et al.: This experiment was performed in 1977 at Oak Ridge National Laboratory. The method employed to perform the experiment was a TOF with 40 m path length. The sample used was a ^{57}Fe metallic sample with a purity of 93.6%. The detectors employed were two non hydrogenous liquid scintillators and a 0.5 mm thick Li-6 glass as neutron flux monitor. The data were analyzed using a modified version of the ORNL/RPI Monte Carlo code by J.G. Sullivan et al. The analysis was performed in the energy range from 1 keV up to 200 keV and a total of 106 resonances were analyzed [62].

- ENDF/B -VII.1: (American) Evaluated Nuclear Data Files [51].

- Sukhoruchkin: Compilation of the previous experimental data,which includes the two previous experiments and the ENDF data [48].

In order to have a clear overview about the obtained capture kernels, a plot with a comparison between the n_TOF data and the previous experiments is shown in Fig. 5.5.

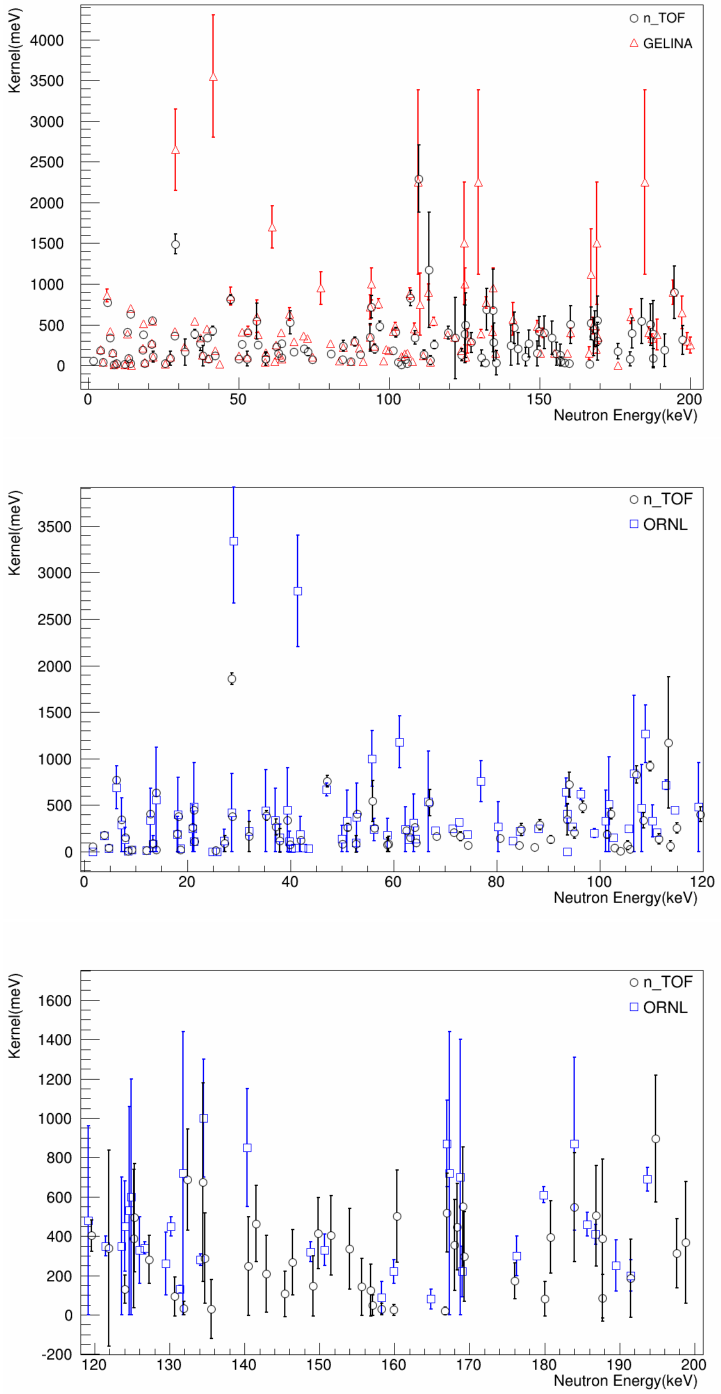

Figure 5.5: *Experimental kernels from n_ TOF, GELINA and ORNL.*

In table 5.6 the radiative Kernels obtained in this analysis are reported. In table 5.7 the table is implemented with the kernels of the previous experiments.

In the n_TOF data a total of 116 resonances are clearly visible in the energy range up to 200 keV. 62 of these resonances show a statistical deviation less than 50% with an average RMS of 20%. The statistics of the remaining 53 resonances are low thus yielding an average RMS of 92.3%. However, these resonances are clearly visible in the data.

E_0 *(eV)*	j	*l*	Γ_n*(meV)*	Γ_γ*(meV)*	***Kernel(meV)***
1630	2	1	50	470	53
3963 (1.2)	0	0	200090	763 (8)	179 (2)
4755 (0.1)	1	1	70	440 (76)	43 (8)
6248 (2.5)	1	0	501790 (5584)	1098 (13)	773 (13)
7231 (0.1)	2	1	926	422 (9)	343 (8)
7947 (0.2)	1	1	1781	247 (6)	154 (4)
8537 (0.5)	1	1	10	538 (359)	7 (5)
9217 (0.3)	1	1	40	298 (170)	25 (15)
12105 (0.2)	1	1	500	22 (27)	15 (19)
12878 (0.2)	1	1	1734	860 (27)	408 (14)
13316 (0.2)	1	1	1332	137 (12)	88 (8)
13978 (3.3)	2	1	1541	18 (14)	22 (18)
13995 (0.5)	1	0	13302	961 (30)	632 (21)
18091 (0.5)	1	1	2540	304 (13)	193 (9)
18263 (0.6)	1	1	3787	618 (22)	377 (14)
18742 (2)	1	1	3253	35 (4)	24 (3)
21097 (0.7)	2	1	3283	240 (10)	265 (12)
21342 (0.8)	2	1	10285	490 (20)	553 (23)
21390 (1.2)	2	1	98	1378 (793)	108 (66)
25487 (0.3)	1	1	190	49 (49)	28 (29)
27253 (0.2)	1	1	325	194 (180)	86 (85)
28940	1	0	3231500	2116 (166)	1490 (125)
28696 (1.2)	2	1	5466	324 (17)	361 (20)
32015 (0.4)	2	1	550	401 (375)	165 (163)
35282 (1.9)	2	1	950	505 (67)	390 (55)

37199 (2.9)	1	1	6004	403 (122)	268 (86)
37987 (0.4)	1	1	360	324 (324)	121 (128)
39487 (3.9)	1	1	21036	484 (40)	336 (29)
39892 (6.7)	1	1	11009	113 (21)	79 (16)
41276 (40.1)	1	0	999709	599 (74)	425 (55)
42076 (3.7)	0	1	7823	554 (80)	122 (19)
47168 (22.2)	1	0	450082	1155 (76)	812 (57)
50071 (5.3)	0	1	3484	391 (90)	83 (20)
51088 (2.7)	0	1	5602	1392 (208)	264 (42)
52702 (1)	1	1	160	435 (434)	83 (87)
53012 (5)	1	1	21018	588 (52)	406 (38)
56000	0	0	10000000	2324 (884)	546 (221)
56339 (5.8)	0	1	12009	1170 (143)	252 (33)
58858 (0.5)	1	1	130	635 (600)	77 (76)
59025 (0.1)	1	1	140	602 (585)	81 (83)
62515 (5)	1	1	7581	340 (50)	231 (36)
63219 (7)	1	1	7155	222 (39)	153 (28)
64154 (5.3)	1	1	7681	393 (57)	265 (41)
64333 (9.9)	1	1	12824	138 (42)	97 (31)
67010 (4.8)	1	1	4431	892 (226)	527 (141)
68300 (7.8)	1	1	13260	236 (37)	164 (28)
71678 (11.6)	1	1	31417	290 (44)	204 (33)
72984 (4.6)	1	1	930	318 (86)	168 (48)
74455 (8.5)	1	1	6001	98 (29)	68 (21)
80610 (6.7)	1	1	1433	234 (54)	142 (35)
84411 (7.3)	1	1	1667	103 (53)	69 (37)
84760 (7.1)	1	1	1862	416 (107)	241 (66)
87341 (7.5)	1	1	1700	72 (42)	49 (30)
88413 (12.9)	2	1	19801	247 (45)	288 (55)
90490 (14)	0	1	21997	576 (178)	133 (43)
93674 (81.7)	1	0	200190	491 (226)	346 (169)
94023 (17)	1	1	86109	1028 (184)	721 (136)
95011 (15.1)	1	1	17603	295 (79)	206 (58)
96728 (11.3)	1	1	16352	711 (85)	484 (61)
101392 (11.4)	2	1	10852	159 (35)	185 (43)
102153 (11.1)	2	1	15987	354 (48)	409 (59)

102922 (11.9)	2	1	9522	36 (29)	42 (36)
103971 (12.4)	2	1	10184	5 (13)	5 (17)
105343 (51.4)	2	1	106560	60 (37)	70 (46)
105869 (11.9)	2	1	9334	23 (28)	28 (34)
107045 (9.3)	2	1	15445	734 (78)	828 (94)
108507 (11.2)	2	1	9461	297 (69)	341 (84)
109864 (11.8)	1	0	4601349	3253 (553)	2292 (414)
111407 (12.6)	2	1	10645	117 (44)	137 (55)
113278 (5.6)	2	1	6430	1173 (666)	1173 (704)
113658 (11.4)	2	1	7896	55 (45)	65 (56)
114898 (13.4)	2	1	14812	220 (43)	257 (53)
119580 (18.5)	1	1	33380	577 (110)	403 (81)
121897 (0.9)	1	1	897 (883)	1016 (1006)	338 (499)
124001 (8.4)	1	1	897	232 (119)	131 (71)
125202 (473.4)	1	0	1501800	550 (469)	387 (351)
125322 (7.5)	2	1	736	967 (736)	494 (398)
127300 (8.5)	1	1	830	764 (313)	282 (122)
130698 (9.1)	1	1	1500	145 (145)	94 (99)
131900 (8.5)	0	1	800	172 (169)	34 (35)
132408 (8.3)	2	1	1360	1014 (358)	687 (257)
134403 (960.3)	0	0	3295100	2872 (2018)	674 (504)
134702 (8.5)	2	1	290	1517 (1142)	288 (229)
135531 (8.6)	2	1	290	28 (132)	30 (151)
140502 (3.1)	1	1	534	1014 (969)	248 (251)
141510 (444.3)	1	0	1501600	1975 (775)	464 (193)
142900 (8.7)	1	1	468	792 (699)	209 (195)
145401 (8.8)	1	1	181	909 (928)	107 (116)
146400 (9.2)	1	1	637	910 (538)	266 (166)
149102 (8.7)	1	1	278	809 (794)	147 (152)
149799 (8.7)	1	1	1050	1320 (543)	415 (180)
151502 (9.3)	1	1	1025	1283 (607)	404 (202)
153998 (8.9)	1	1	842	1090 (627)	337 (205)
155599 (8.6)	1	1	263	834 (801)	142 (144)
156802 (8.8)	1	1	223	854 (859)	125 (133)
157100 (9.2)	1	1	75	968 (983)	49 (53)
158300 (9.2)	1	1	150	792 (758)	30 (30)

159900 (9.3)	1	1	37	996 (998)	25 (27)
160314 (629.9)	1	1	2753100	707 (311)	502 (234)
166976 (547.1)	1	0	699370	737 (268)	519 (201)
166700 (9.4)	0	1	90	802 (806)	19 (20)
167999 (10)	2	1	1060	419 (259)	355 (232)
168351 (10.1)	2	1	1360	525 (243)	448 (220)
169143 (218.8)	1	0	700300	782 (403)	550 (302)
169253 (9.8)	2	1	1270	313 (228)	297 (229)
175985 (276.1)	0	0	699370	737 (368)	173 (92)
180000 (10.3)	2	1	950	73 (76)	80 (88)
180802 (10.4)	2	1	1270	454 (200)	395 (184)
183987 (1026.8)	1	0	3485700	770 (369)	546 (277)
186883 (10.3)	2	1	1270	641 (307)	504 (255)
187683 (1310.3)	0	0	3184600	367 (479)	86 (120)
187701 (2.8)	2	2	490	1000 (982)	389 (404)
191495 (0.6)	1	1	360	974 (985)	186 (199)
194803 (10.7)	2	2	1230	1974 (672)	896 (322)
197603 (10.5)	2	2	810	394 (208)	313 (175)
198805 (9.6)	2	2	1230	415 (331)	367 (309)

Table 5.6: *Value of the kernel obtained from n_ TOF data.*

E*$_0$ *(eV)	***n_ TOF (meV)***	***GELINA (meV)***	***ORNL (meV)***
3963	179(2)	195(20)	170(20)
4755	43(8)	43(2)	35(0)
6248	773(13)	860(80)	690(230)
7231	343(8)	420(40)	290(0)
7947	154(4)	160(10)	130(0)
8537	7(5)	8(2)	6(0)
9217	25(15)	28(2)	23(0)
12105	15(19)	13(1)	13(1)
12878	408(14)	390(20)	340(0)
13316	88(8)	83(10)	87(0)
13995	632(21)	700(40)	560(0)
18091	193(9)	210(15)	190(0)
18263	377(14)	510(30)	400(0)
18742	24(3)	37(4)	34(0)
21097	265(12)	280(20)	250(0)
21342	553(23)	540(40)	480(0)
21390	108(66)	100(15)	110(0)
25487	28(29)	14(3)	0(0)
27253	86(85)	100(10)	120(0)
28940	1490(125)	2650(500)	3340(670)
28696	361(20)	420(30)	420(0)
32015	165(163)	230(20)	220(0)
35282	390(55)	540(30)	440(0)
37199	268(86)	340(20)	340(0)
37987	121(128)	130(20)	150(0)
39487	336(29)	450(30)	450(0)
39892	79(16)	90(10)	110(0)
42076	122(19)	180(20)	190(0)
47168	812(57)	850(110)	670(70)
50071	83(20)	120(10)	140(0)
51088	264(42)	410(30)	330(0)
52702	83(87)	100(30)	97(15)
53012	406(38)	430(50)	370(0)
56000	546(221)	600(200)	1000(300)

56339	252(33)	380(40)	240(120)
58858	76(159)	160(30)	180(0)
62515	231(36)	250(30)	240(0)
63219	153(28)	130(20)	130(10)
64154	265(41)	400(30)	310(0)
64333	97(31)	80(20)	140(10)
67010	527(141)	630(80)	540(0)
68300	164(28)	290(30)	230(30)
71678	204(33)	360(30)	250(20)
72984	168(48)	330(30)	320(30)
74455	68(21)	100(30)	190(40)
80610	142(35)	270(40)	270(0)
84411	69(37)	60(30)	0(0)
84760	241(66)	220(40)	220(0)
87341	49(30)	50(20)	0(0)
88413	288(55)	300(20)	250(20)
90490	43(133)	210(30)	0(0)
94023	721(136)	720(150)	640(20)
95011	206(58)	240(20)	270(150)
96728	484(61)	760(60)	620(20)
101392	185(43)	200(0)	200(60)
102153	409(59)	420(30)	510(0)
107045	828(94)	880(70)	840(0)
108507	341(84)	0(0)	470(0)
109864	2292(414)	2250(1130)	1270(0)
111407	137(55)	120(40)	210(30)
113278	1173(704)	900(100)	720(30)
113658	65(56)	40(20)	0(0)
114898	257(53)	540(50)	450(50)
119580	403(81)	380(40)	480(40)
121897	338(499)	350(40)	350(0)
124001	131(71)	180(30)	350(50)
125202	387(351)	0(0)	530(0)
125322	494(398)	0(0)	600(0)
127300	282(122)	310(40)	340(30)
130698	94(99)	0(0)	260(30)

131900	34(35)	0(0)	450(160)
132408	687(257)	770(70)	720(0)
134403	674(504)	0(0)	1000(300)

Table 5.7: *n_ TOF kernels compared with previous works.*

A comparison between the n_TOF data and the previous experiments is illustrated in Fig. 5.6.

Compared versus the previous experiment at GELINA the n_TOF kernels are in average 17% lower in the energy range from 1 eV to 130 keV. The average deviation (weighted by error bars) is of (17±1.6)% as shown in Fig. 5.6.

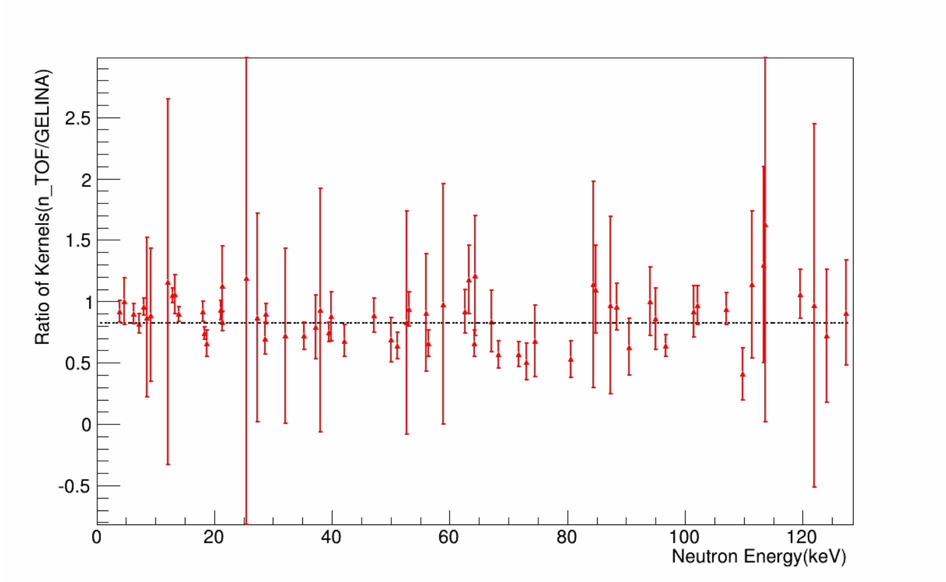

Figure 5.6: *Ratio of the kernels between n_ TOF data and GELINA data.*

To better evaluate this difference a caparison of the ratio, in the energy range between 1 keV and 60 keV and between 61 keV and 130 keV was made. In Fig. 5.7 the ratio in the energy range up to 60 keV is shown. The average deviation is of (15±1.8)%. In Fig. 5.8 the ratio in the energy range from 61 keV up to 130 keV is shown. In this last case the average deviation is (28±3.4)%.

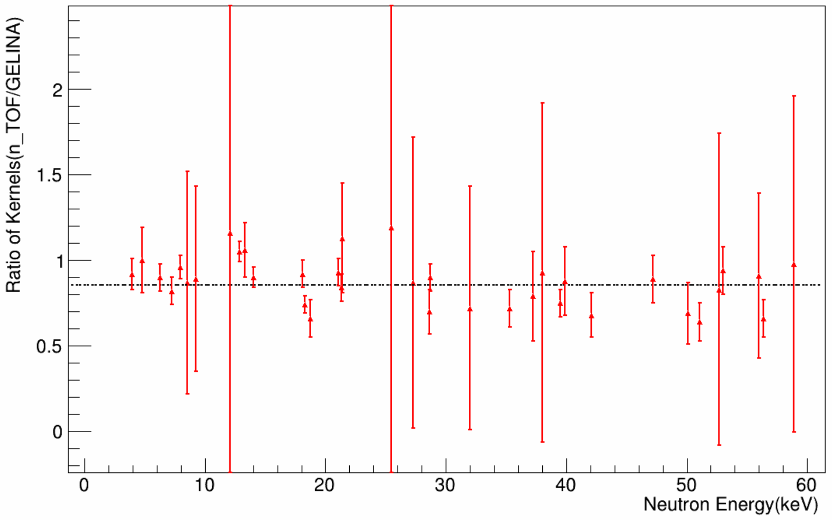

Figure 5.7: *Ratio of the kernels between n_ TOF data and GELINA data in the energy range from 0 up 60 keV.*

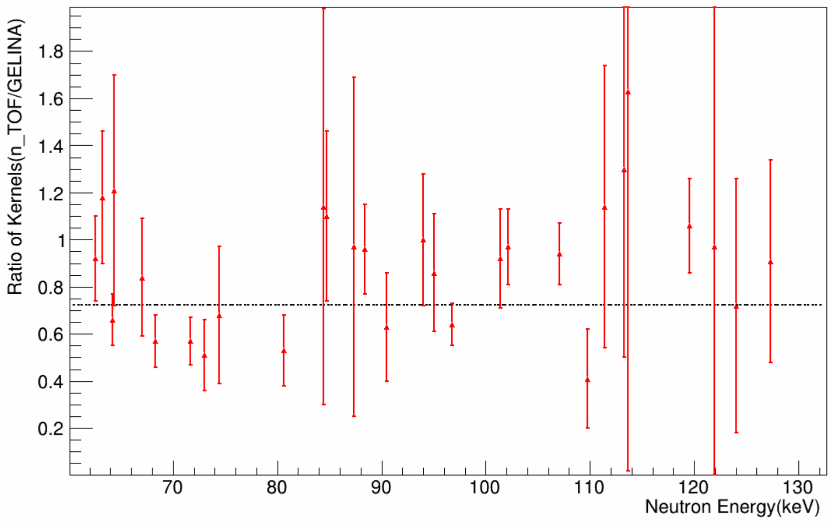

Figure 5.8: *Ratio of the kernels between n_ TOF data and GELINA data in the energy range from 60 up 120 keV.*

Compared versus the ORNL experiment the n_TOF data are in average 2.5% (RMS) lower in the energy range up to 130 keV (Fig. 5.9). The average deviation is of (2.5±1.5)%.

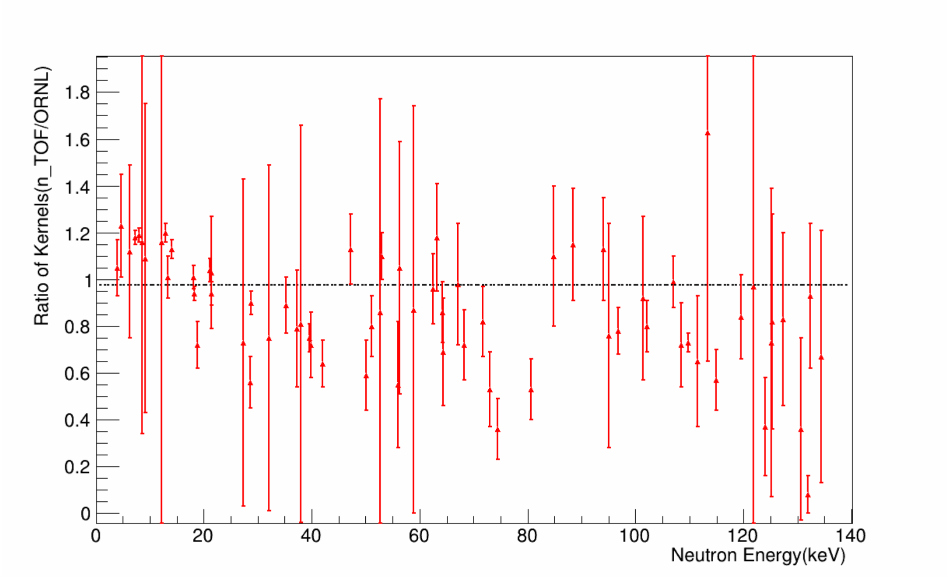

Figure 5.9: *Ratio of the kernels between n_ TOF data and ORNL data.*

As in the case of the comparison between the n_TOF and GELINA, the ratio was calculated in the same energy range as shown in Fig. 5.10 and Fig. 5.11.

In the range from 1.63 keV to 60 keV the RMS deviation between n_TOF and ORNL is of only (0.4±1.1)%. Surprisingly, in the range from 60 keV up to 130 keV is lower by (31±2.4)%

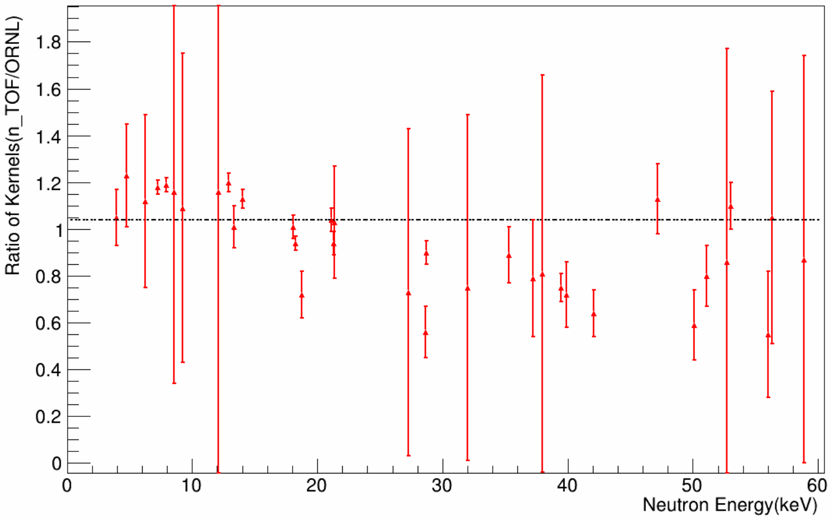

Figure 5.10: *Ratio of kernels between n_ TOF data and ORNL data in the energy range till 60 keV.*

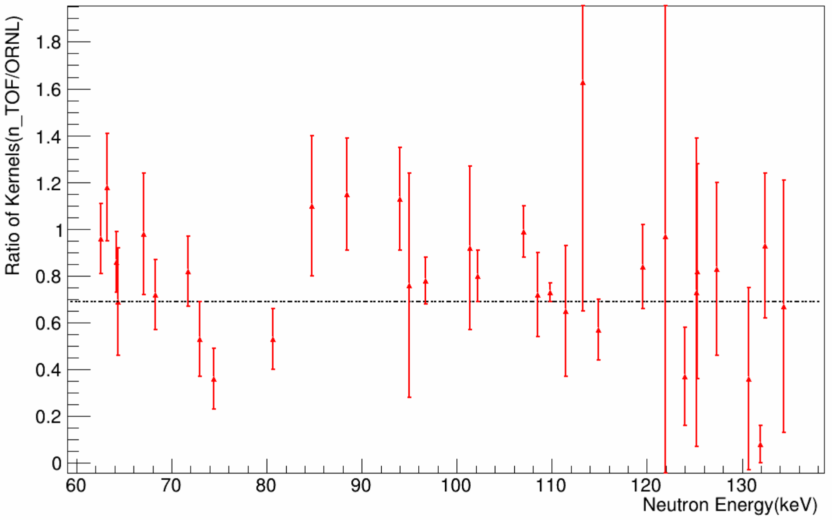

Figure 5.11: *Ratio of the kernels between n_ TOF data and ORNL data in the energy range between 60 keV up 130 keV.*

- Range from 1 to 10 keV

In this energy range a set of 8 resonances are visible. The first p-wave resonance at 1.63 keV is absent in the ORNL data. The n_TOF kernel is 4.7% higher than the GELINA kernel. The first s-wave is 8.5% lower that the GELINA one and 5% higher than the ORNL one.

A good agreement is present between n_TOF and GELINA kernel for the p-wave at 4.75 keV. Otherwise the ORNL results are 23% lower.

The other resonances in this range show a tendency to be lower than the GELINA data and higher than the ORNL data.

- Range from 12 to 20 keV

A set of 8 resonances is clearly visible. For our data the best fit at 13.98 keV was possible introducing an additional resonance at 13.97 keV. This resonance is not visible in the fit but is present in the Sukhoruschkin compilation. In the previous experiments this doublet at 13.99 keV is tabulated as a single resonance. In this energy range the same tendency noted in the previous point is present.

- Range from 21 to 30 keV

Seven resonances are present both in n_TOF and in GELINA. However, the 25 keV resonance is not present in the ORNL data.

A doublet is visible at 21.33 keV and their kernels are in better agreement with the ORNL data.

A big difference is remarkable for the s-wave at 28 keV, where our data are 30% and 45% lower than GELINA and ORNL data, respectively.

- Range from 30 to 60 keV

In this energy range 16 resonances are clearly visible. The previous experiments report 15 resonances because the doublet at 58.8 keV was interpreted as a single resonance. These resonances are lower than the GELINA and ORNL data. A difference is remarkable for the s-wave at 56 keV. n_TOF kernel is 9% lower than the GELINA kernel and 45% lower than ORNL data. This difference might be due to a neutron sensitivity effect in the ORNL data.

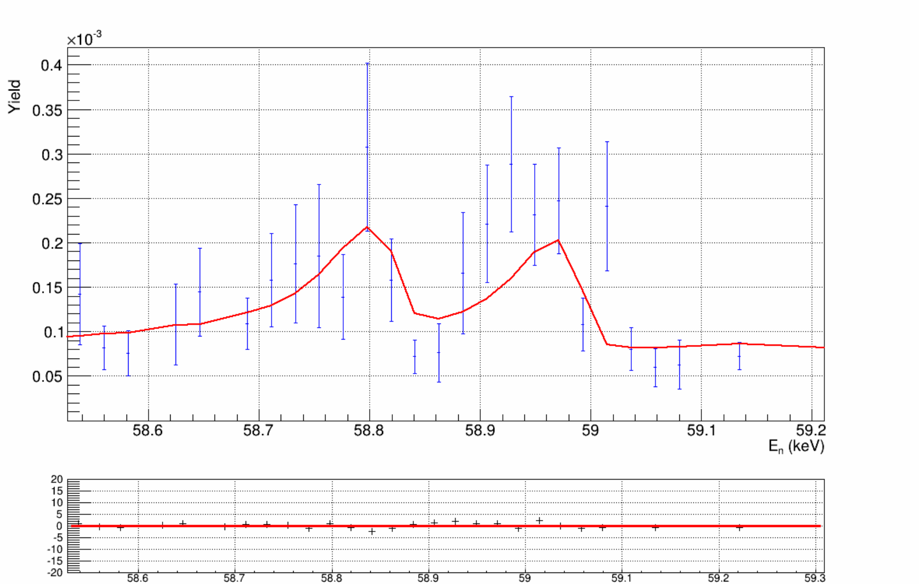

Figure 5.12: *Doublet at 58.8 keV.*

- Range from 60 to 130 keV

39 resonances were analyzed in the n_TOF data, where eight resonances more than in the GELINA and ORNL data are clearly visible. In this energy range the n_TOF kernels are 15% lower than the GELINA kernels and 31% lower than the ORNL kernels.

- Range from 130 to 200 keV

In this range 37 resonances could be analyzed. In the GELINA experiment 28 resonances are tabulated and in the ORNL data 23 resonances are present.

5.4 Neutron Sensitivity

Discrepancies with respect to previous experiments at GELINA and ORNL cannot be ascribed to an effect related to the neutron sensitivity. Fig. 5.13 shows the ratio of the kernels versus Γ_n/Γ_γ, where no systematic trend can be appreciated.

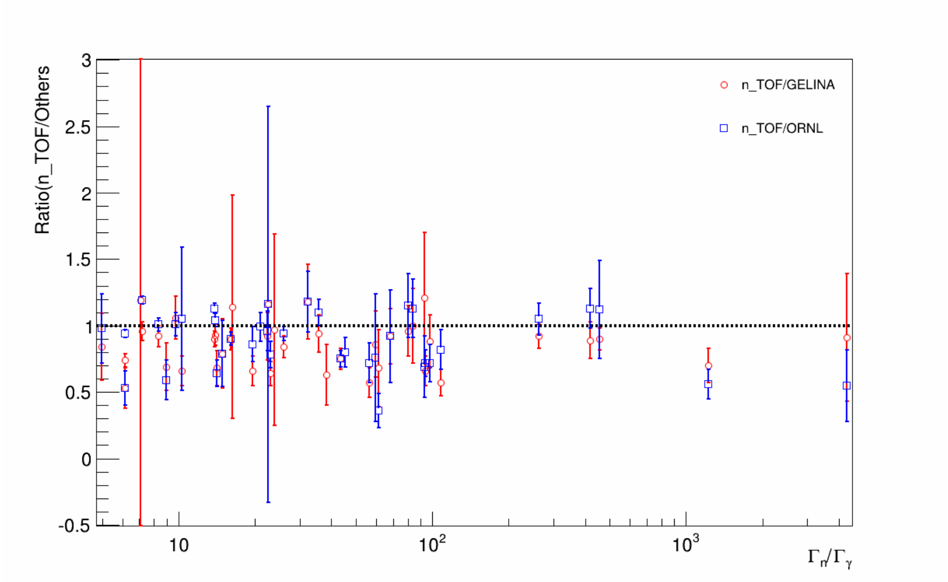

Figure 5.13: *Ratio of the kernels between n_ TOF and the previous experiments versus* Γ_n/Γ_γ.

5.5 Thermal Cross Section

The thermal cross section was calculated using equation 4.6. The result is 943 mb,(the contribution of the first three s-wave resonances). In table 5.8 the value for the thermal neutron capture cross section compared versus the experimental value is shown [58].

Parameters	$\sigma(mb)$
n_TOF	943 (1.03)
Mughabghab	2480

Table 5.8: *Thermal neutron capture cross sections calculated using equation (4.6) for the resonance parameters of n_ TOF. At the bottom the experimental value of the thermal CS is given [59].*

The difference between the thermal cross section obtained from the n_TOF data and the experimental value can be ascribed to direct capture.

5.6 Maxwellian Averaged Cross Section (MACS)

The MACS for ^{57}Fe have been calculated. The value obtained from n_TOF data compared with GELINA, ORNL and KADONIS [60] data are reported in table 5.9.

Parameters	MACS at 30 keV(mb)
n_TOF	26.8 ± 4.4
GELINA	39.9 ± 4.0
ORNL	36 ± 2.3
KADONIS	40 ± 4.0

Table 5.9: *MACS at 30 keV for the resonance parameters of n_ TOF, GELINA and ORNL. At the bottom the value reported in KADONIS is given.*

The lower value of the n_TOF MACS is to be ascribed to the systematically lower kernels.

5.7 Conclusion

For ^{57}Fe a total of 116 resonance were analyzed in the range from 1 eV up to 200 keV. Our data were compared versus two other experiments performed at ORNL by Allen et al. [62] in 1977 and at GELINA by Rohr et al. [61] in 1983. At the same time the n_TOF data are compared versus the ENDF data library and the overall Sukhoruchkin compilation. In general our data have a tendency to be lower than the GELINA data in the whole energy range, and a tendency to be higher than the ORNL data up to 20 keV. Our data are in average 2.5% lower than the ORNL data and 17% lower than the GELINA data. There is a difference between the MACS obtained from our data and the value reported in KADONIS. This discrepancy is due to the fact that n_TOF data are in general lower that the GELINA and ORNL data. It is important to remark that the analysis for the s-wave resonance was performed using only the FZK data, in order to avoid possible neutron sensitivity effects in the BICRON detector.

Chapter 6

Conclusion

The aim of the present work was to perform a measurement of the (n,γ) cross-section of ^{54}Fe and ^{57}Fe in the resolved resonance region (RRR). These measurements were carried out with high resolution using the time of flight technique at CERN n_TOF facility. In order to properly account for the γ-ray energy dependence of the detection efficiency, the Pulse Height Weighting Technique (PHWT) was used and applied. The technique is based on the use of low efficiency detectors, such that at most one gamma ray of the capture cascade can be detected in each capture event. Therefore one needs to introduce a weight in the response function, so that the efficiency is proportional to the registered gamma ray energy. In this way the cascade detection efficiency becomes proportional to the known cascade energy and independent of the cascade path. This Weighting Function (WF) is obtained from a set of detector response functions for different γ-ray energies. The PHWT requires the precise knowledge of the detector response as a function of energy and a detailed geometry and atomic composition of the experimental setup. To this aim, the experimental set-up was realistically modelled in a MC simulation using the code GEANT4. From these calculations, a weight as a function of deposited energy was calculated and applied to the measured count rate in order to obtain the capture yield. In the measurement of (n,γ) cross sections using the PHWT, there are some experimental effects which need to be taken into account. Indeed effects like gamma summing, electronic threshold in the detectors and internal conversion electrons are important to obtain the yield correction factor. The approach to determine the yield correction factor was based on the MC method to reproduce the shape of the prompt γ-ray spectrum for the measured capture resonances. Once the weighting was calculated and applied to the sorted data, the analysis of ^{54}Fe and ^{57}Fe was performed. An absolute normalization of the capture yield was obtained from the measurement of the 4.9 eV saturated resonance of a gold sample. Subsequently the resolved resonance region has been analyzed using the R-matrix code SAMMY.

In the case of the ^{54}Fe (n,γ) cross-section, a total of 168 resonances were analyzed in the range from 1 eV up to 500 keV. Our data were compared versus two other experiments performed in the past at ORNL by Allen et al. in 1976 and at GELINA by Brusegan et al. in 1982. The n_TOF data show an average deviation respect to the GELINA data of 0.76% and are 17% lower than the ORNL data. The thermal cross section obtained from our data is in reasonable agreement with the thermal cross section calculated for the previous experiments taking into account only the contribution of the first s-wave resonance. Otherwise the MACS calculated at 30 keV are in reasonable agreement with the value reported from KADONIS.

In the case of the ^{57}Fe (n,γ) cross-section, a total of 116 resonances were analyzed in the range from 1 eV up to 200 keV. Our data were compared versus two other experiments performed at ORNL by Allen et al. in 1977 and at GELINA by Rohr et al. in 1983. In general the n_TOF data have a tendency to be lower than the GELINA data in the whole energy range, and a tendency to be higher than the ORNL data up to 20 keV. Our data are in average 2.5% lower than the ORNL data and 17% lower than the GELINA data. As discussed below, this discrepancy cannot be attributed to the effect of the neutron sensitivity. On the other hand both ^{54}Fe + n and ^{57}Fe + n have a rather hard γ-ray spectrum which spans up to 9.3 MeV and 10 MeV respectively. The spectrum of ^{197}Au + n extends only up 6.512 MeV. This make the measurement of these cross-sections particularly sensitive to the weighting function.

In our case, as it was demonstrated in the chapter 2, we have calculated via Monte-Carlo simulations weighting functions for each particular sample measured. In all case, the proportionality condition has been achieved whit a high level of precision, thus allowing us to obtain a capture yield for both ^{54}Fe and ^{57}Fe, which is not affected by the hardness or the details of the prompt γ-ray cascade.

An advantage of the present experiment is that the capture measurement were carried out with two different type of C_6D_6 detectors, each one showing a very different intrinsic neutron sensitivity. This way, by comparing the capture yield measured with each detector, we had a direct estimate of the contribution of the neutron sensitivity which turned out to be negligible (see fig. 4.9 and 5.13). New resonances were analyzed in both experiments as reported in chapters 4 and 5. To conclude we can say that the analysis made for both isotopes is relevant for the design of the ADS. Neutron activation of ^{54}Fe leads to the production of ^{55}Fe, which has a half-life of 2.7 years and therefore contribute to the short-therm activation of the reactor.

Being ^{54}Fe and ^{57}Fe two *s*-process seed nuclei in massive star nucleosynthesis, it would be interesting to determine the cross-section at high energy (~ 100 keV) with improved statistic, in order to determine more accurately the value of the MACS at $KT = 91$ keV characteristic of the shell C-burning in massive stars, prior to their explosion as supernovae.

Resumen

La medida de secciones eficaces de captura neutronica (n,γ) para dos de los isotopos del hierro, ^{54}Fe y ^{57}Fe, ha sido realizada en la instalación n_TOF del CERN con el objetivo de una mejor comprensión del llamado proceso lento (del inglés s-process) de la nucleosíntesis estelar. Al mismo tiempo, el hierro es un constituyente fundamental para la realización y el diseño de sistemas de producción de energía asistidos por acelerador(ADS del inglés Accelerator Driven Systems). La medida de secciones eficaces (n,γ) para los isotopos ^{54}Fe y ^{57}Fe en el rango de las resonancias resueltas (RRR) ha sido llevada a cabo utilizando la técnica de tiempo de vuelo. Dichas medidas han sido realizadas utilizando una adecuada configuración experimental de manera tal que las secciones eficaces puedan ser determinadas con un error sistemático despreciable debido a la sensibilidad neutrónica. La primera parte de este trabajo ha consistido en desarrollar simulaciones Monte Carlo de la función de respuesta de los detectores para calcular la correspondiente función peso. Estas funciones peso han sido aplicadas a los datos medidos para poder obtener experimentalmente la tasa de captura neutrónica. El análisis final de la sección eficaz ha sido realizado utilizando el código SAMMY. Los datos obtenidos en nuestras medidas han sido contrastados frente a experimentos realizados anteriormente en otras instalaciones de medida similares.

Motivación

Principios de astrofisica nuclear

La nucleosíntesis describe los procesos nucleares involucrados en la combinación atómica de los núcleos con el fin de crear otros núcleos atómicos. Las estrellas son el escenario perfecto para las diversas reacciones necesarias para que se produzca la nucleosíntesis de los elementos pesados. En astrofísica los elementos de la tabla periódica se dividen generalmente en dos grupos en función del número atómico Z. Así tenemos los elementos ligeros con Z$\leq$ 30, y los elementos pesados con $30 \leq$ Z ≤ 83. El hierro representa un cambio de régimen en cuanto a cómo los elementos se pueden crear. Los neutrones son la clave para la formación de elementos pesados debido a que las temperaturas en el interior de las estrellas no son lo suficientemente altas para que los elementos más pesados que el hierro se puedan formar a través de reacciones de captura de protones. Esto es posible porque no hay repulsión de Coulomb para superar la interacción entre los neutrones y los elementos pesados. Si el flujo es bajo($\sim 10^8$/cm^3), se puede asumir que el proceso es lento ("s" del inglés slow). Esto quiere decir que el tiempo entre dos capturas neutrónicas sucesivas es típicamente superior al tiempo de decaimiento de elementos inestables [5, 6].

Bajo estas consideraciones, durante una irradiación neutrónica el cambio en abundancia N(A) de un particular isotopo A puede ser expresado como:

$$\frac{dN(A)}{d\tau} = \sigma(A-1)N(A-1) - \sigma(A)N(A), \tag{6.1}$$

donde el termino τ es la exposición neutronica.

Como alternativa al proceso lento s existe el proceso rápido (del inglés r -process) que ocurre en presencia de un elevado flujo de neutrones y se asocia con entornos estelares explosivos como pueden ser supernovas y sistemas binarios de estrellas de neutrones en colisión, aunque el entorno concreto de proceso r no se ha descubierto con certeza todavía. Muchos isotopos pueden surgir de la contribución de estos dos procesos, y por lo tanto la abundancia observada, debida al roceso r es igual a:

$$N_r = N_\odot - N_s. \tag{6.2}$$

donde $N_\odot$ es la abundancia solar observada, y N_s es la contribución del proceso s. Las abundancias isótopicas s pueden ser bien determinadas gracias a secciones eficaces (n,γ), las cuales pueden ser medidas experimentalmente. Por esas razones el objetivo principal de este trabajo ha sido la determinación experimental de las secciones eficaces de captura en los isótopos del hierro ^{54}Fe y ^{57}Fe, en función de los parámetros típicos E_0, Γ_γ and Γ_n calculando sucesivamente el kernel o area de captura, que se expresa como:

$$K_r = g\frac{\Gamma_n \Gamma_\gamma}{\Gamma}. \tag{6.3}$$

Diseño de reactores híbridos avanzados

El campo de la tecnología nuclear y principalmente la produccion de energía en plantas nucleares es otro ámbito donde las medidas de secciones eficaces juegan una función muy importante. Uno de los problemas principales en las centrales nucleares son los residuos radioactivos, por esa razón se está considerando la posibilidad de reducir estos residuos por medio de reacciones (transmutaciones) inducidas por neutrones. Mediante una reacción de captura (n,γ) o (n,f), a la vez que se produce energía se podrían convertir los residuos radioactivos en elementos estables o al menos reducir la cantidad de los isótopos de vidas medias más prolongadas. Esta es la base para la realización de los reactores híbridos avanzados (ADS) [13, 14, 15]. El hierro es omnipresente como constituyente de componentes estructurales de los sistemas ADS y todos los isotopos estables del hierro estan directamente involucrados en la construcción y diseño de un sistema ADS. Por esa razón la medida de la sección eficaz de captura neutrónica en los isotopos del hierro es de utilidad para el diseño de estos reactores nucleares subcríticos.

La instalación CERN n_TOF

La instalación CERN n_TOF [19, 20] es una instalación de tiempo de vuelo donde se producen neutrones mediante el mecanismo de espalación. Por ello, los protones proporcionados por el CERN PS con 20 GeV/c impactan en un blanco de plomo de 80 x 80 x 60 cm^3. Parte de los neutrones generados vienen canalizados por medio de un tubo de vacío por el que viajan hasta el área experimental que esta localizada a 185 m. El blanco de plomo está sumergido en agua borada que tiene la función de actuar como refrigerante y como moderator para los primeros neutrones rápidos que tienen una dependencia de 1/E con el flujo hasta una energía de aproximadamente 1 MeV. La única interfaz entre el moderador y el tubo de vacío es una ventana de aluminio de 16 mm de espesor. A 120 m está localizado un dipolo magnético de 2 m para limpiar totalmente los neutrones de las particulas secundarias cargadas. Finalmente dos colimadores posicionados a 135.5 m y 173.35 m respectivamente, permiten dar una forma gaussiana al haz de neutrones. La estación de medida empieza a 182.5 m de la ventana del blanco de espalación pero la muestra que se va a medir esta posicionada generalmente a 185 m de distancia.

Técnica de medida

En la medida de los isótopos de hierro hemos utilizado la técnica de los detectores de energía total. Para ello hemos empleado dos detectores C_6D_6 que tienen la ventaja de una despreciable sensitividad neutrónica [21]. La técnica de medida esta detalladamente descrita en el capítulo 2. La técnica de los detectores de energía total se basa en utilizar detectores de muy baja eficiencia, de manera que se pueda registrar como máximo un gamma por cada cascada nuclear. Por esa razón, ya que la cascada de los rayos gamma sigue caminos diferentes tras cada captura, la eficiencia de detección para cada evento depende de cada rayo gamma detectado. Para corregir este efecto se aplica un peso a la función de respuesta del detector de manera que la eficiencia de detección sea proporcional a la energía del rayo gamma detectado. Por lo tanto tenemos que determinar un peso W_i para cada amplitud de señal i. Finalmente aplicando este peso a la función de respuesta R_{ij} de nuestro sistema de detección para un rayo gamma de energía E_j, tiene que ser verificada la siguiente condición:

$$\sum_i W_i R_{ij} = kE_j. \tag{6.4}$$

Esta es la base de la técnica de pesado de pulsos PHWT [17, 18]. Las funciones de respuesta R_{ij} necesarias para obtener la función peso

W_i se han calculado mediante simulaciones Monte Carlo. El código utilizado para las simulaciones y el modelo geométrico del aparato experimental ha sido GEANT4 [27]. Un resultado relevante de esta parte del trabajo es que las funciones de respuesta dependen no solamente del proprio detector, sino de la muestra a medir, tanto de su composición como de su geometría. Para poder calcular la función peso necesitamos una serie de ecuaciones como la eq. (4) en un rango de energía que cubra hasta la energía del espectro de captura de los isótopos medidos. Para obtener esa función peso es necesario haber calibrado previamente los detectores para obtener y convolucionar las funciones de respuesta obtenidas, como se describe en la sección 2.3.

La función peso W_i ha sido obtenida utilizando un código en FORTRAN. Al mismo tiempo el perfil espacial del haz está incluido en el fichero de entrada para incluir su efecto en las funciones de respuesta. Para evaluar la incertidumbre (estadística y sistemática) de las funciones peso obtenidas, se ha desarrollado un método basado en la simulación Monte Carlo de los procesos de desexcitación nuclear que ocurren tras cada captura neutrónica. Como los estados excitados del núcleo compuesto son conocidos experimentalmente solo hasta un cierto valor de la energía, por encima del último nivel experimental conocido se ha hecho uso de un modelo estadístico del núcleo que permita completar la cascada nuclear hasta la energía de captura. La parte de la cascada nuclear correspondiente al modelo estadístico se puede calcular como se ha descrito en la sección 2.5.1. La intensidad de las transiciones desde estos niveles a los experimentales reales a baja energía se puede calcular utilizando el modelo de la resonancia dipolar gigante [28]. Para calcular transiciones entre los niveles de la región estadística se han utilizado varios modelos diferentes de densidad de niveles [30, 31] . Este cálculo ha sido programado e implementado como generador de eventos en el código GEANT4, en el cual hemos incluido también una representación detallada del dispositivo experimental de medida. De esta manera se puede reproducir de forma completa la función de respuesta de los detectores para una captura neutrónica en cada resonancia. Simulando un experimento ideal, despreciando los errores experimentales, y aplicando la función peso a cada respuesta ideal se puede calcular la incertidumbre debida a la función peso (sección 2.5.2). El método descrito anteriormente permite no solo estimar la incertidumbre debida a la función peso, sino también las incertidumbres debidas a los efectos experimentales como el umbral electrónico de los detectores, la conversión electrónica y la posible detección de dos o mas rayos gamma a la vez. Completada esta parte del trabajo, lo siguiente ha sido analizar los datos de nuestras medidas. Para ello se desarrolló un programa de análisis basado en el paquete ROOT del CERN [35, 36] descrito en la sección 3.4. Finalmente, utilizando el metódo Monte Carlo anteriormente descrito ha sido posible estimar las incertidumbres debidas a los efectos experimentales (umbral electrónico de los detectores, conversión electrónica...). Una vez obtenida la tasa de captura experimental en función de la energía del neutrón incidente, (sección 3.1), aplicando el método de la resonancia saturada (sección 3.7), este ha sido analizado con el código SAMMY [42]. Este código permite analizar reacciones con neutrones y utiliza el formalismo R-matrix con el método de Bayes. SAMMY nos permite tener en cuenta diferentes efectos experimentales, como por ejemplo incluir el tamaño y las características de la muestra, y los efectos descritos en las secciones 3.10 y 3.11.

Finalmente el factor de corrección a aplicar a la tasa de captura experimental ha sido calculado para diferentes valores de spin J y de momento angular orbital l. Los valores obtenidos están representados el las tablas 4.5 y 5.5 para cada isótopo.

Sección eficaz de captura en ^{54}Fe

La disposición experimental y las características de la muestra empleada en esta medida están descritas en detalle en el capítulo 4. El planteamiento para interpretar y reducir los datos es el descrito en el capítulo 3. Para calcular la función peso se han calculado la función de respueta de rayos gamma monoenergéticos desde una energía de 50 keV hasta 14 MeV. En este caso un total de 36 simulaciones han sido realizadas. Minimizando la ecuaccion 2.7 se han obtenido los parametros de la función peso mostrados en la tabla 4.2. Además para la corrección de los errores inducidos por los efectos experimentales detalladas simulaciones Monte Carlo han sido realizadas. El mejor acuerdo entre los espectros experimentales y la simulación se ha obtenido utilizando la aproximación de Von Egydy et al. [31]. Los parámetros utilizados se muestran en la tabla 4.3. Para obtener el factor de normalización la muestra de referencia ha sido una de ^{197}Au de 20 mm × 1 mm. El factor de corrección de umbral electrónico ha sido calculado para cada grupo de spin y paridad. La sensitividad neutrónica del dispositivo de medida ha sido evaluada como se describe en la sección 4.5 y resultó ser prácticamente despreciable. En esta medida se ha utilizado un umbral electrónico de 250 keV para ambos detectores. Utilizando el código SAMMY se han analizado un total de 168 resonancias en un rango de energía desde 1 eV hasta 1 MeV. Estas resonancias han sido comparadas con datos de experimentos anteriores, principalmente con el de Allen et al.[54, 55] realizado en ORNL y con el de Brusegan et al.[52, 53] realizado en GELINA. Nuestros datos muestran una relación promedio de desviación de los datos GELINA de 0.76% y son un 17% más bajos que los datos de ORNL.

En nuestro análisis siete nuevas resonancias han sido identificadas y analizadas. En la tabla 4.7 se muestran los valores obtenidos en términos de kernel y la tabla 4.8 corresponde a una comparación entre los datos de n_TOF y los de los experimentos anteriores. La contribución de las resonancias analizadas a la la sección eficaz térmica ha sido calculada y comparada con las anteriores. En este caso un buen acuerdo existe entre nuestros datos y los de los dos experimentos anteriores. Sin embargo estos datos están un 37% por debajo de la sección eficaz térmica medida con precisión [57], la cual se puede deber a captura directa y a la contribución de resonancias por debajo del umbral de captura. Las MACS (Maxwellian Averaged Cross Sections) calculadas a partir de las resonancias medidas y analizadas en este trabajo muestran buen acuerdo con la evaluación más reciente de KADONIS [60].

Sección eficaz de captura en ^{57}Fe

La configuración experimental, el método para interpretar los datos, calcular la función peso y estimar los efectos experimentales han sido equivalentes a los utilizados en la medida del ^{54}Fe. Una cosa que hay que remarcar en esta medida es que se ha utilizado un umbral electrónico de 250 keV para el detector Bicron y de 300 keV para el detector FZK. Todos los cálculos realizados se muestran en detalle en el capítulo 5. En este trabajo los datos de n_TOF han sido comparados con dos experimentos anteriores, con el de Allen et al.[62] realizado en ORNL y con el de Rohr et al. [61] realizado en GELINA. En esta medida un total de 116 resonancias han sido analizadas con el código SAMMY en un rango de energía desde 1 eV hasta 200 keV y un total de siete nuevas resonancias no presentes en las librerias han sido analizadas en detalle. En general, nuestros datos tienen una tendencia a ser más bajo que los datos de GELINA en todo el rango de energía, y una tendencia a ser mayores que los datos de ORNL hasta 20 keV. Nuestros datos estan en promedio un 2.5% por debajo de los datos de ORNL y un 17% más bajos que los datos de GELINA. En las tablas 5.6 y 5.7 se muestran los datos de n_TOF y se comparan con los anteriores en término de kernel. Como en el caso anterior, la seccíon eficaz térmica y la MACS han sido calculados. En este caso se pueden notar diferencias remarcables dentre los calculos obtenidos con los datos n_TOF y los presentes en las librerias. La sensitividad neutrónica también resultó ser mínima y sin implicaciones para el análisis de esta muestra.

Bibliography

[1] E.M. Burbidge, G.R. Burbidge, W. A. Fowler, & F. Hoyle, *Synthesis of the Elements in Stars*,1957, Rev. Mod. Phys., 29, 547.

[2] G. Wallerstein et al., *Synthesis of the elements in stars: forty years of progress*, Rev. Mod. Phys. 69, 995–1084 (1997).

[3] K. Krane, *Introductory Nuclear Physics*, John Wiley and Sons Inc.

[4] V. Castellani, *Fondamenti di Astrofisica Stellare*, Zanichelli 1985.

[5] C. Arlandini et al., *Neutron Capture in Low-mass Asymptotic Giant Branch Stars: Cross Sections and Abundance Signatures*, The Astrophysical Journal, 525:886-900, 1999 November 10.

[6] C. Travaglio et al., *Galactic Chemical Evolution of Heavy Elements: from Barium to Europium*, The Astrophysical Journal, 521:691-702, 1999 August 20.

[7] F. Kappeler et al., *s-process Nucleosynthesis-nuclear Physics and the Classical Model*, Rep. Prog. Phys. 52 945,1989.

[8] M. Pignatari,*The Weak s-process In Massive Stars and its Dependence on the Neutron Capture Cross Section*, The Astrophysical Journal, 710:1557–1577, 2010 February 20.

[9] R. Gallino et al., *Evolution and Nucleosynthesis in Low-Mass Asymptotic Giant Branch Stars. II. Neutron Capture and the s-Process*, The Astrophysical JournaL, 497:403, 1998 April 10.

[10] Z. Y. Bao et al., *Neutron Cross Sections for Nucleosynthesis Studies*, Atomic Data and Nuclear Data Tables 76, 70–154 (2000).

[11] B. J. Allen, I. Bergqvist, R. E. Chirien, D. Gardner, W. P. Poenitz, *Neutron Radiative Capture, Pergamon Press.*

[12] A. Foderaro, *The elements of Neutron Interaction Theory*, The MIT Press.

[13] Nuclear Energy Agency Organisation for Economic Cooperation and Development, *Accelerator-driven Systems (ADS) and Fast Reactors (FR) in Advanced Nuclear Fuel Cycles,* http://www.oecd-nea.org.

[14] Y. Kadi and J.P. Revol, *Design of an Accelerator-Driven System for the Destruction of Nuclear Waste*, Workshop on Hybrid Nuclear Systems for Energy Production, Utilisation of Actinides & Transmutation of Long-Lived Radioactive Waste, Trieste, 3 - 7 September 2001.

[15] C. Rubbia et al., *Conceptual Design of a Fast Neutron Operated High Power Energy Amplier*, CERN/AT/95-44 (EET), CERN, Geneva, 1995.

[16] Macklin and Gibbons, *Capture Cross-Section Studies for 30-220 keV Neutron Using a New Technique*, Phys. Rev. 159 (1967), pag. 1007.

[17] J. L. Tain et al., *Accuracy of the pulse height weighting technique for capture cross section measurements*, Journal of Nuclear Science and Technology, Supplement 2, (2002), 689.

[18] U. Abbondanno et al., *New experimental validation of the pulse height weighting technique for capture cross-section measurements*, Nucl. Instr. and Meth. Phys. Res. A (2004), pag. 454.

[19] CERN n_TOF Facility: *Performance Report, CERN/INTC-O-011 INTC-2002-037 CERN-SL-2002-053 ECT.*

[20] C. Guerrero et al., *Performance of the neutron time-of-flight facility n_ TOF at CERN*, Eur. Phys. J. A (2013) 49: 27

[21] R. Plag et al., *An optimized* C_6D_6 *detector for studies of resonance-dominated (n,γ) cross-sections*, Nucl. Instr. and Meth. in Phys. Res. A 496 (2003), pag. 425.

[22] S. Marrone, et al., *A low-mass neutron flux monitor for the n_ TOF facility at CERN*, Nuclear Instruments and Methods A (2003).

[23] D.B. Gayther, *International Intercomparison of Fast Neutron Flux-Rate Measurements Using Fission Chamber Transfer Instruments*, Metrologia 27, 221- 231, (1990).

[24] Y. Giomataris, et al., *Micromegas: a high granularity position sensitive gaseous detector for high particle-flux environments*, Nucl. Instr. and Methods A 376 (1996) 29-35.

[25] Glenn Knoll, *Radiation Detection and Measurement*, third edition (2000), pag. 115.

[26] C. Domingo Pardo, *New radiative neutron capture of* ^{207}Pb *and* ^{209}Bi*, PhD Thesis.*

[27] *GEANT4 User's Guide for Application Developers. Version: GEANT4 9.3*, December 2009.

[28] J. Kopecky, M. Uhl, *Test of gamma-ray strength in nuclear reaction model calculation*, Phys. Rev. C., 41(1990), pag.1941.

[29] J. Kopecky et al., *Observation of the M1 Giant Resonance by resonance averaging in* ^{106}Pd, Nucl. Phys. A 468 (1987), pag. 285.

[30] *Handbook for calculation of nuclear reaction data, RIPL-2, IAEA-TECDOC-1506*, August 2006.

[31] T. Von Egidy et al., *Nuclear Level Densities and Spacing Distribution: Part II*, Nucl. Phys. A 481(1988), pag. 189.

[32] F.H. Frohner, *Evaluation and Analysis of Nuclear Resonance Data*, JEFF Report 18, 2000.

[33] *Manuale Cremonese di ELETTRONICA, Parte specialistica*, Edizioni Cremonese, 1996.

[34] C. Guerrero et al., *Nuclear Instruments and Methods in Physics Research*, A 597 (2008) 212–218.

[35] *Castor Website: http://cern.ch/castor.*

[36] *LSF/LXBATCH Website: http://batch.web.cern.ch/ batch/.*

[37] Volker Blobel, *The BOS System: Bank Object System, Fifth and last printing*, June 19, 2003.

[38] G. Lorusso et al., *Time-energy relation of the n TOF neutron beam: energy standards revisited*, Nucl. Instr. and Meth. in Phys. Res. A 532 (2004), pag. 622.

[39] C. Guerrero, *Neutron Fluence of the n_TOF-ph2 Facility*, n_TOF internal note, August 2011.

[40] R.L. Macklin et al., *Absolute Neutron Capture Yield Calibration*, Nucl. Instr. and Meth. in Phys. Res. A 164 (1979), pag. 213.

[41] J. W. Boldeman, B. J. Allen, A. R. de L. Musgrove, R. L. Macklin, *The Neutron Capture Cross Section of Natural Silicon*, Nuclear Physics A252 (1975) 62–76.

[42] Nancy M. Larson, *Updated users' guide for Sammy: Multilevel r-matrix fits to neutron data using Bayes' equations*, ORNL/TM-9179/R8 ENDF-364/R2, October 2008.

[43] F. Belloni, *Study of Beam Profile with MGAS detector*, n_TOF internal note 2011.

[44] W.R. Leo, *Techniques for Nuclear and Particle Physics Experiments, Springer Verlag*, 1987.

[45] B. Povh, K. Rith, C. Scholz,*Particelle e Nuclei*, Bollati Boringhieri.

[46] D. Cano, E. Mendoza, *New Neutron Library for GEANT4 code*, private communication, 2010.

[47] Souchkouskin et al., *Neutron Resonance Parameters For 54-Fe (Iron)*, Springer 2009.

[48] Souchkouskin et al., *Neutron Resonance Parameters For 57-Fe (Iron)*, Springer 2009.

[49] J.A.Adams, G.White, Nucl. Instr. and Meth. A1 56 (1978) 459.

[50] C. Domingo, J.L. Tain, *Resolution Function and Flux from TOF02* C_6D_6 *measurements*, n_TOF Internal Note IFIC-2002-3, October 2002.

[51] ENDF/B-VII, Incident neutron data.

[52] C*omm. of the European Commun. report to I.N.D.C.*, No.15, p.13 (1982).

[53] *http://www-nds.iaea.org/exfor/exfor.htm*, EXFOR, request 21798.

[54] Nuclear Physics, Section A, Vol.269, p.408 (1976).

[55] *http://www-nds.iaea.org/exfor/exfor.htm*, EXFOR, request 30355.

[56] *TACASI; analysis of resonance measurements*, S. Friesenhahn, ANL/NESC-410 Technical Report;

[57] *FANAC: a shape analysis program for resonance parameter extraction from neutron capture data for light and medium-weight nuclei*, Kernforschungszentrum Karlsruhe ; KFK 2145 : Inst. fur Neutronenphysik u. Reaktortechnik ;

[58] S.F. Mughabghab, *Neutron Cross Sections from Neutron Resonance Parameters and Thermal Cross Sections*, Academic Press (1981).

[59] H. Beer et al., *On the calculation of Maxwellian-Averaged Capture Cross Section*, The astrophysical journal supplement series, 80:403-424, 1992 May.

[60] I. Dillmann, R. Plag, F. Kappeler, T. Rauscher, Karlsruhe *Astrophysical Database of Nucleosynthesis in Stars, KADONIS, http://www.kadonis.org.*

[61] *http://www-nds.iaea.org/exfor/exfor.htm*, EXFOR, request 31846.

[62] *http://www-nds.iaea.org/exfor/exfor.htm*, EXFOR, request 31847.

Acknowledgements

I am very grateful to José Luis Taín for giving me the opportunity to work in the group of gamma spectroscopy of IFIC. At the same time I am grateful to César Domingo Pardo for following me constantly in my thesis work. I am truly grateful to have been able to work with the group of gamma spectroscopy having expanded and improved my knowledge. Thanks to all members of the group starting with José Luis Taín and Berta Rubio. Thanks to Cesar, Alejandro, Jorge, Ebe, Loli, Sonia, Kike, Ana, Victor and Pancho. Another thanks goes to the n_TOF collaboration for giving me the opportunity to realize this thesis. Thanks to C. Guerrero, N. Colonna, D. Cano, P. Calviño and all people I met during my experience at CERN. I want to write just a few words to thank my family. Thank you for supporting me, giving me the strength and desire to continue making me feel your closeness, not making me weigh the various past problems. Another thanks goes to my second family, Judokan Valencia, who welcomed me since my first day here in Valencia.

Finally I want to thank Rebeca for giving me the strength and the desire to finish this work, a big kiss to you.